The Pennsylvania State University

The Graduate School

Department of Chemistry

# FUNCTIONAL MATERIALS FROM LAYERED OXIDES

A Dissertation in

Chemistry

by

Yoji Kobayashi



Submitted in Partial Fulfillment
of the Requirements
for the Degree of

Doctor of Philosophy

May 2008

The dissertation of Yoji Kobayashi was reviewed and approved* by the following:

Thomas E. Mallouk
DuPont Professor of Materials Chemistry and Physics
Thesis Advisor
Chair of Committee

Harry R. Allcock
Evan Pugh Professor of Chemistry

John V. Badding
Associate Professor of Chemistry

Digby D. Macdonald
Distinguished Professor of Materials Science and Engineering

Ayusman Sen
Professor of Chemistry
Head of the Department of Chemistry

*Signatures are on file in the Graduate School

## ABSTRACT

In Chapter 2, the layered Dion-Jacobson perovskites $HLaTa_2O_7$, $HLaNb_2O_7$, and structural variants of $HLaNb_2O_7$ were prepared and their AC and DC conductivities were measured under various temperatures and atmospheres. The layered structure in $HLaNb_2O_7$ was modified by pillaring, exfoliation-restacking, and further annealing. The modification in structure strongly affected the grain boundary conduction, rather than grain bulk conduction. Grain boundary conduction is thought to be strongly dependent on adsorbed water, whereas grain conduction would be more dependent on movement of interlayer protons. $HLaNb_2O_7$ was prone to reduction under hydrogen, yielding a mixed ionic-electronic conductor. In-plane conductivity measurements on an oriented film of $HLaNb_2O_7$ showed similar behavior. Part of this reduction was suppressed by addition of water vapor to the ambient atmosphere and by replacing the B-site niobium with tantalum.

In Chapter 3, the nanoscroll-to-nanotube thermal transformation was studied for $H_4Nb_6O_{17}{\cdot}4.4H_2O$ scrolls, prepared by exfoliation of $K_4Nb_6O_{17}$. Thermal dehydration of the scrolls produces $Nb_2O_5$ nanotubes at 400-450$^oC$. The non-topochemical transformation results in polycrystalline nanotubes; however, significant texturing with respect to the tube axis is observed. Substituting Ta for Nb in the precursor compound led to a lower yield of scrolls, most likely because there is less built-in lattice strain to drive scrolling of the unilamellar colloidal sheets.

Chapter 4 reports the synthesis of a wide range of single crystal spinel platelets with exposed (111) faces, lateral dimensions in the micron range, and thicknesses of 20-50nm, prepared by soft chemical dehydration of well crystallized layered precursors. This method enables the synthesis of the metastable composition $NiCoAlO_4$, which cannot be prepared by conventional solid state synthesis. Because of their nanoscale thickness, mosaic structure, shape anisotropy, and surface porosity, $NiCoAlO_4$ and $NiCo_2O_4$ platelets exhibit room temperature superparamagnetism ($T_B$ = 40K, 250K respectively) despite the fact that they have micron-size lateral dimensions. The accessibility of a wide

range of superparamagnetic spinel platelets (as opposed to cubes or spheres) should be useful for studies in ferrofluids and related composite magnetic materials.

The final chapter examines the fluorination of the layered perovskites $NaYTiO_4$, $RbLaNb_2O_7$, and $KCa_2Nb_3O_{10}$ to yield the fluorine-exchanged perovskite products $Na_yTiO_{4-x}F_x$, $RbLaNb_2O_{7-x}F_x$, and $KCa_2Nb_3O_{10}$. Such fluorination under an inert atmosphere preserves the layered perovskites structure but slightly modifies the unit cell. Fluorination reduces the B-site cation, inducing a mixed valency at the B-site. Electronic structure calculations on $RbLaNb_2O_6F$ show that in the absence of structural disorder, the resulting material is a 2-D metallic conductor. $RbLaNb_2O_6F$ is air stable, and is capable of ion-exchange with aqueous acid. By exfoliating these layered materials, it may be possible to obtain metallic conducting oxide nanosheets, which have not been extensively reported upon in the past.

# TABLE OF CONTENTS

## LIST OF FIGURES

# LIST OF TABLES

## ACKNOWLEDGEMENTS

Along my way I have been helped by many. I am grateful to my advisor Professor Mallouk for the freedom in research that he has let me pursue. Joining the group, I was aware that the group's research spans much in breadth, and that I would be required to be independent, but that I would also gain a degree of freedom in research. For this, combined with his support for my present and future career, I am truly grateful.

My research exposed me to diverse characterization techniques, and so I am indebted to the staff at the Materials Science and Engineering Department, Materials Research Institute, and Physics Department. Prof. Digby Macdonald and Hungoo Cho provided much assistance for the impedance experiments and analysis. The electron microscopy staff, namely Joseph Kulik, Trevor Clark, and Joshua Maier, helped me become fully trained on many aspects of the transmission electron microscope. Magda Salama and Raafat Malek have often done more than normally required to help me obtain data and interpretation regarding various powder characterization techniques. Prof. Peter Schiffer and Xianglin Ke explained to me what all the magnetic data meant. Finally, when I was in an XRD pinch Nichole Wonderling was always there to help.

It has been fun to be in the Mallouk Group. Joshua Schottenfeld helped me get started with crystallography, and it was fun building apparatus and debating the data in the midst of all the confusion surrounding us. Other members of the group have truly made the lab experience much better, and it was a pleasure and honor to be with them.

I must mention my parents for their wonderful environment they provided me in my childhood and freedom and support in later years. Finally, I also thank my wife Leiliang for her company these past few years—our journey together has just begun.

# Chapter 1

## Introduction—Functional Materials from Layered Oxides

The flexible modification of existing materials to add new functionality often requires reduced dimensionality. For example, the one dimensional nature of a polymer chain permits high control over what monomer units are to be arranged in what order, or, the layered two dimensional nature of the graphite[1, 2] and $LiCoO_2$ electrodes[3, 4] in lithium ion battery cells permits lithium ions to readily diffuse deep into solid particles, which might otherwise be impenetrable. It is also this layered nature of graphite which permits them to be modified into single graphene sheets,[5] rolled nanotubes,[6] and spherical fullerenes,[7] all of which have novel properties. The goal of this work is to explore the chemistry surrounding various layered inorganic oxide materials as relevant to the structural modification and properties enhanced as a result.

For all chapters except Chapter 4, the layered oxides involved possess exchangeable interlayer cations. The Dion-Jacobson layered perovskites, such as $RbLaNb_2O_7$, are one such type of material, and appear in Chapters 2 and 5. These layered perovskites are formed of slabs of $ABO_3$ (A = La, B = Nb, etc) perovskite, with an exchangeable alkali ion (Rb) between the layers, as shown in Figure 1.1. The slabs can vary in thickness by the number of $BO_6$ octahedra, and are indicated by the number *n*. Hence, the layered perovskite shown is an *n* = 2 Dion-Jacobson phase. The interlayer alkali metal can be exchanged for various other cations such as protons or other alkali metals. The protonated compound can further react with bases, such as in the intercalation of alkyl amines,[8, 9] or with the hydroxide salt of tetrabutylammonium.[10, 11] The latter results in intercalation of the tetrabutylammonium cation and exfoliation into a unilamellar suspension.

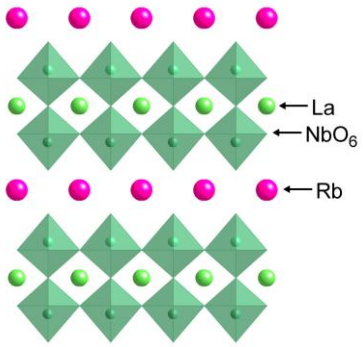


Figure 1.1: Structure of Dion-Jacobson layered perovskite, $RbLaNb_2O_7$

In the next chapter (Chapter 2), this layered perovskite is examined as a building block for a conducting oriented films. The protonated form of $RbLaNb_2O_7$ is known to be a solid acid even at temperatures above 100 °C.[12] This makes these films interesting candidates as proton conducting electrolyte membranes in fuel cells which could operate at temperatures of 200-300°C, which is an extremely attractive temperature range in terms of efficiency and robustness against fuel impurities such as CO. The protonic/electronic conductivities of various structural variants of $HLaNb_2O_7$ was examined. In general, the ionic conductivity was low at elevated temperatures and the material was dominated by electronic conductivity under reducing atmospheres; however, a large dependence of conductivity on the orientation of the layered structure was observed. Thus, further research in nanostructured oxide membranes with tailored conductivity paths is still warranted, and at present little studies of such exists despite much potential.[13]

The same type of intercalation chemistry observed in the Dion-Jacobson layered perovskites also applies for $K_4Nb_6O_{17}$, which is the starting material used in Chapter 3. It has been reported that many layered oxides, upon exfoliation, can be rolled into scrolls (albeit at low yields) using various wet chemistry techniques.[14] Of these layered compounds, some are known to topochemically dehydrate into crystalline products. Examples are $HTiNbO_5$ dehydrating to $Ti_2Nb_2O_9$,[15, 16] $H_2La_2Ti_3O_{10}$ dehydrating to $La_{2/3}TiO_3$,[17] or layered double hydroxides dehydrating to spinels.[18] If these materials can

be exfoliated and scrolled in the correct orientation, single crystalline oxide nanotubes would result. Attempts to exfoliate and scroll the compounds mentioned above were not successful; however, in this study we examined the crystallographic changes that occur when a layered material known to exfoliate and scroll ($K_4Nb_6O_{17}$)[19, 20] transforms non-topochemically to a tubular structure. Various results show that the resulting nanotubes are polycrystalline, but still textured with respect to the nanotube, which is an encouraging result as we pursue the synthesis of other single crystalline oxide nanotubes. $Nb_2O_5$ nanotubes have not been previously reported, and their high surface area may serve as useful materials as catalyst supports or electrodes in Li-ion batteries.

In Chapter 4, we take advantage of the platelet morphology inherent in layered materials to produce new morphologies of a cubic material, the spinel structure. When platelet single crystals of layered transition metal hydroxides are heated in an oxidative atmosphere, they transform to spinel platelets, with compositions such as $NiCo_2O_4$, $NiCoAlO_4$, or $CoFe_2O_4$. Similar to grinding table salt, most previous synthesis of these spinel materials result in roughly spherical or cubic nanoparticles. Here, we report the preparation of single crystalline, yet mosaic structured nanoplatelets which still possess room temperature superparamagnetism despite their size much larger than the cubic or spherical spinel nanoparticles.

Chapter 5 demonstrates a possibly general method to modify various insulating layered perovskites into conducting layered variants via reductive anion exchange. Most of the layered perovskites with interlayer cation chemistry are insulating $d^0$ compounds with the B-site cation at their highest oxidation state. Reductive fluorination replacing one of the oxygen sites induces a mixed valence in the B-site. The extra electron is injected into the conduction band, and these compounds are expected to be either metallic or, in the case of other effects such as disorder removing metallicity, semiconductors with good conductivity. While such compounds have been prepared by reductive cation exchange, anion exchange is advantageous since the interlayer chemistry is still preserved and the material may be able to still undergo ion exchange, exfoliation, etc. This will drastically increase the possibilities and raise new questions regarding layered perovskites in terms of electronic properties.

Throughout this thesis, it has been the author's goal to demonstrate the various new functions and properties introduced into layered materials which are unique. The structured conducting films, textured nanotubes, and large superparamagnetic platelets hopefully succeeded in doing so. Finally, the last chapter has attempted to expand the field into electronically interesting materials by exploring the preparation of ion-exchangeable perovskites with mixed valences.

## References


1. Shu, Z. X.; McMillan, R. S.; Murray, J. J. *J. Electrochem. Soc.* **1993,** *140*, 922-927.

2. Yazami, R.; Guerard, D. *J. Power Sources* **1993,** *43*, 39-46.

3. Auborn, J. J.; Barberio, Y. L. *J. Electrochem. Soc.* **1987,** *134*, 638-641.

4. Honders, A.; Der Kinderen, J. M.; Van Heeren, A. H.; De Wit, J. H. W.; Broers, G. *Solid State Ionics* **1984,** *14*, 205-216.

5. Novoselov, K. S.; Geim, A. K.; Morozov, S. V.; Jiang, D.; Zhang, Y.; Dubonos, S. V.; Grigorieva, I. V.; Firsov, A. A. *Science* **2004,** *306*, 666-669.

6. Iijima, S.; Toshinari, I. *Nature* **1993,** *363*, 603-605.

7. Kroto, H. W.; Heath, J. R.; O'Brien, S. C.; Curl, R. F.; Smalley, R. E. *Nature* **1985,** *318*, 162-163.

8. Guo, C.-x.; Hou, W.-h.; Guo, M.; Yan, Q.-j.; Chen, Y. *Chem. Commun.* **1997**, 801-802.

9. Gopalakrishnan, J.; Bhat, V. *Mater. Res. Bull.* **1987,** *22*, 413-417.

10. Schaak, R. E.; Mallouk, T. E. *Chem. Mater.* **2002,** *14*, 1455-1471.

11. Schaak, R. E.; Mallouk, T. E. *Chem. Mater.* **2000,** *12*, 2513-2516.

12. Matsuda, T.; Fujita, T.; Miyamae, N.; Takeuchi, M.; Kanda, K. *Bull. Chem. Soc. Jpn.* **1993,** *66*, 1548-1550.

13. Maier, J. *Nature Materials* **2005,** *4*, 805-815.

14. Ma, R.; Bando, Y.; Sasaki, T. *J. Phys. Chem. B* **2004,** *108*, 2115-2119.

15. Fang, M.; Kim, C. H.; Saupe, G. B.; Kim, H.-N.; Waraksa, C. C.; Miwa, T.; Fujishima, A.; Mallouk, T. E. *Chem. Mater.* **1999,** *11*, 1526-1532.

16. Fang, M.; Kim, C. H.; Mallouk, T. E. *Chem. Mater.* **1999,** *11*, 1519-1525.

17. Gopalakrishnan, J.; Bhat, V. *Inorg. Chem.* **1987,** *26*, 4299-4301.

18. Markov, L.; Petrov, K.; Lyubchova, A. *Solid State Ionics* **1990,** *39*, 187-193.

19. Saupe, G. B.; Waraksa, C. C.; Kim, H.-N.; Han, Y. J.; Kaschak, D. M.; Skinner, D. M.; Mallouk, T. E. *Chem. Mater.* **2000,** *12*, 1556-1562.

20. Du, G.; Chen, Q.; Yu, Y.; Zhang, S.; Zhou, W.; Peng, L.-M. *J. Mater. Chem.* **2004,** *14*, 1437-1442.

# Chapter 2

## Structural Effects in the Protonic/Electronic Conductivity of Dion-Jacobson Phase Niobate and Tantalate Layered Perovskites

## Introduction

Currently, much research on fuel cells focuses on low temperature polymer electrolyte fuel cells (PEMFC) and high temperature solid oxide fuel cells (SOFC). PEMFC and SOFC technologies are both promising because good proton and oxide ion conductor materials are available for the appropriate temperature ranges. In the intermediate temperature range (250 - 400 °C), however, there are few thermally stable materials that have the high ionic conductivity ($10^{-1}$ to $10^{-3}$ S/cm) needed for fuel cell membranes.[1] Compared to PEMFCs, fuel cells operating in the intermediate temperature regime are more resistant to catalyst poisoning by CO, and a wider range of less expensive catalysts can be used. Because of their lower operating temperature, intermediate temperature fuel cells are less affected by the materials engineering issues stemming from the high temperatures used in SOFCs.

The polymeric membranes used in PEMFCs lose conductivity above 100°C because of dehydration, and most ion conducting polymers are chemically unstable in the intermediate temperature regime. A number of polymer-inorganic composites and polymers combined with nonaqueous liquid proton conductors have been studied for use between 100 and 200°C,[2] Recently poly(benzoimidazole) derivatives, such as poly[2,5-benzimidazole] have been reported to be stable up to 200 ˚C.[3] However, even these suffer from loss of the dopant, phosphoric acid, at higher temperatures.

On the other hand, a number of inorganic solids such as $BaCeO_3$,[4] $Ba_3Ca_{1.18}Nb_{1.82}O_{9-\delta}$ (BCN18),[5, 6] and $CsH_2PO_4$[7] are known to have appreciable proton conductivity at temperatures between 250 and 600˚C.[4,6] Layered solid acids such as α-$Zr(HPO_4)_2 \cdot H_2O$[8], which retain intercalated water molecules, can have appreciable

protonic conductivity at even lower temperatures. In these materials the layers act as conduction channels for protons and water. The disadvantages of layered solid acids include irreversible dehydration at temperatures from 300-400 ˚C. These issues are sometimes a hindrance not only in operation, but also in processing or fabrication of membrane-electrode assemblies, since high temperature steps such as sintering cannot be performed.

Layered inorganic solids undergo exfoliation, restacking, and pillaring reactions that can in principle be useful in fabricating intermediate temperature membranes and membrane-electrode assemblies. The Dion-Jacobson phase layered perovskite $HLaNb_2O_7$ has already been modified by all of these processes.[9-12] Furthermore, this compound has been shown to be quite acidic and to retain mobile lattice protons up to 400 °C under dry atmospheres.[13] Although no general thermodynamic data exist, these types of acidic perovskites are thought to be metastable compounds, and the dehydration of $HLaNb_2O_7$ to $LaNb_2O_{6.5}$ is irreversible. Previous studies have shown that several layered perovskites, including $HLaNb_2O_7$, exhibit ionic conductivities of $10^{-5}$ - $10^{-3}$ S/cm at temperatures between 300 and 600˚C.[14-16] Sato *et al* reported that for $HLaNb_2O_7 \cdot 0.5H_2O$ the adsorbed water, rather than interlayer protons, were the dominant cause of proton conductivity at temperatures below 80$^{o}$C, but they did not investigate the conductivity of the compound in the intermediate temperature regime.[17] In this study, the structure of the layered perovskite $HLaNb_2O_7 \cdot 0.5H_2O$ was modified in various ways to increase the surface area for water adsorption and to optimize the conduction paths. The effect of reducing conditions, such as the presence of hydrogen at elevated temperatures, was investigated, and methods to suppress the electronic conductivity caused by reduction were also explored.

## Experimental Section

### Sample Synthesis

Starting materials $RbLaNb_2O_7$, and their tantalate analogues, were prepared by reaction of $Nb_2O_5$, $Ta_2O_5$, and $Rb_2CO_3$ (20% excess) at 1150 °C for 2 days. The phase purity of $RbLaNb_2O_7$ was confirmed by powder X-ray diffraction. The resulting alkali compounds (1g) were then acid exchanged by shaking in 100 mL 4M $HNO_3$ for at least three days with daily centrifugation and replacement of the acid solution. The product was isolated by centrifugation, washing, and finally drying at 60˚C. However, if the next intended step was exfoliation, then the sample was not dried and instead was kept as a slurry in water.

#### *Exfoliation/flocculated samples*

For exfoliation, a larger batch of the protonated compound (4 g, 9.1 mmol) was shaken at 200 rpm for at least 2 days with 8.5 equivalents (3.6 wt%, 550 mL) of aqueous tetra(n-butyl)ammonium hydroxide (TBAOH). The flocculated samples were prepared by taking 300 mL of the suspension, removing excess TBAOH by centrifugation, and then adding $HNO_3$ (1L, 0.05M) dropwise overnight.

#### *Silica-pillared sample*

A literature procedure based on Guo *et al* was adapted.[9] A hexylamine solution of ethanol (50% vol, 12 mL) was added to $HLaNb_2O_7$ (1g), and stirred at 60 °C for 4 days to obtain an intercalated product (d = 24.2 Å). The suspension was washed with ethanol, and a decylamine solution of ethanol (50% vol., 12 mL) was added and refluxed for two weeks. This decylamine intercalated material (d = 29.4 Å) was then washed with ethanol, and further refluxed with either an ethanol solution or a water sol of 3-

aminopropyltriethoxysilane (25% vol., 50 mL) for four days before washing with ethanol. The siloxane-oligomer intercalated material was then calcined at 500 °C overnight to obtain the final pillared product. TGA-MS verified the release of $CO_2$ and $NO_2$ slightly below this temperature.

***Thin-film preparation***

For thin film preparation, the colloidal suspensions of exfoliated materials (50 mL) were centrifuged, decanted, and then resuspended in ethanol (5mL) by agitation, and then cast onto glass slides patterned with Pt electrodes. Typically, 5-6 drops were applied to a glass square (2 cm x 2 cm) with intermittent drying. The Pt patterns consisted of a gap 800 μm wide and 1.5 cm long (conduction in the 800 μm direction) between Cr/Pt pads (150nm thick) prepared by lithography and sputtering techniques. Removal of organics from the thin films was accomplished by heat treatment at 350 °C or by exposure to UV-$O_3$ (either at room temperature or 80 °C) until X-ray diffraction showed a single and constant d-spacing 00l reflection.

**Impedance measurements**

Pellet samples were prepared by pressing 0.5 g of material at 220 MPa for 20 minutes. Unless otherwise noted, pellets (13 mm in diameter, and approximately 1 mm thick) were coated on both sides with 150 nm of Pt by sputtering to produce circular contacts 9 mm in diameter. Room temperature measurements were obtained by equilibrating the pellets under a stream of humidified air (100%RH, room temperature) overnight. Elevated temperature experiments were conducted using a home built flow-through system with a $H_2$ stream of 30 mL/min humidified at $P_{H20}$ = 0.3 atm. Two point impedance measurements were obtained using a Solartron 1255B Frequency Response Analyzer and Solartron 1287 Electrochemical Interface with no DC bias and an alternating voltage amplitude ranging between 50 mV to 500 mV. Frequencies ranged

from 1MHz to 0.01 Hz, depending on the sample. Fitting was conducted using ZView software from Scribner Associates. Using custom-written code, Kramers-Kronig transforms were conducted on select data to test the data for conformity to the stability, causality, and linearity constraints of Linear Systems Theory. Previous work on electrochemical systems has shown that Kramers-Kronig transforms are most sensitive to violation of the stability constraint[18] and thus provide a means to verify if the sample was stable and at equilibrium during measurement.

**DC Conductivity Measurements**

Pellets with Toray carbon paper backings on both sides were pressed at the same conditions as above. The porous carbon paper was used as an electrode instead of platinum films to ensure fast responses of the pelletized material to the hydration environment. Leads were then applied using silver paint, and the pellets were treated under various gases and humidities in an in-house constructed flow-through system.

**Other Characterization**

X-ray powder diffraction patterns were obtained on a Philips XPert system using Cu-K$\alpha$ radiation. Brunauer-Emmett-Teller (BET) surface areas and $N_2$ adsorption isotherms were acquired at 77 K using a Micromeritics 2010 ASAP system. A Nanoscope atomic force microscope (AFM) and NPX200 SII profilometer were used to observe exfoliated material and deposited films. Electron micrographs were obtained using a FEI Quanta 200 scanning electron microscope (SEM) equipped with energy dispersive X-ray spectroscopy (EDS). Thermal gravimetry-mass spectrometry (TGA-MS) was conducted on a TA instruments Q50 thermal gravimetric balance (1 °C/min) in tandem with a Pfeiffer quadrupole mass spectrometer.

## Results and Discussion

X-ray diffraction (XRD) patterns of the parent material $HLaNb_2O_7$ and its tantalum analogues were in good agreement with the literature.[19] Samples of $HLaNb_2O_7$ and $HLaTa_2O_7$ were equilibrated overnight at ambient temperature and at 100% relative humidity; water loss upon subsequent heating was then quantified by thermal gravimetry analysis (TGA). Figure 2.1 Sato *et al* have shown that when $HLaNb_2O_7$ is equilibrated under 100% relative humidity at ambient temperature, it hydrates to $HLaNb_2O_7 \cdot 0.5H_2O$ with a *c* lattice parameter of 11.404 Å, whereas the anhydrous material has a *c* lattice parameter of 10.548 Å.[17] Based on XRD and TGA, our own samples were anhydrous in ambient atmosphere and hydrated to a lower level of $HLaNb_2O_7 \cdot 0.25H_2O$ at 100% RH. However, Sato's formulation of $HLaNb_2O_7 \cdot 0.5H_2O$ will be used for naming the hydrated compound in this paper, since it is possible that water was lost during sample transfer. It is also possible that the dehydration behavior depends on other factors in sample preparation, since Sato *et al* note that water is gradually lost between 100 °C – 400 °C (no heating rate given)[17] whereas Matsuda *et al* see little loss between 100°C to 400 °C (10 °C/min).[13] Our own TGA results show that for the niobate and tantalate, water adsorbed at 100% RH at ambient temperature is lost upon exposure to dry air rather quickly below 100°C, and there is very little further weight loss over the range 100 °C to 400 °C. An abrupt weight loss at 400 °C for $HLaNb_2O_7$ corresponds to irreversible dehydration to $LaNb_2O_{6.5}$, releasing 0.5 mol $H_2O$ per mol of $HLaNb_2O_7$. This dehydration temperature is close to that reported previously.[13]

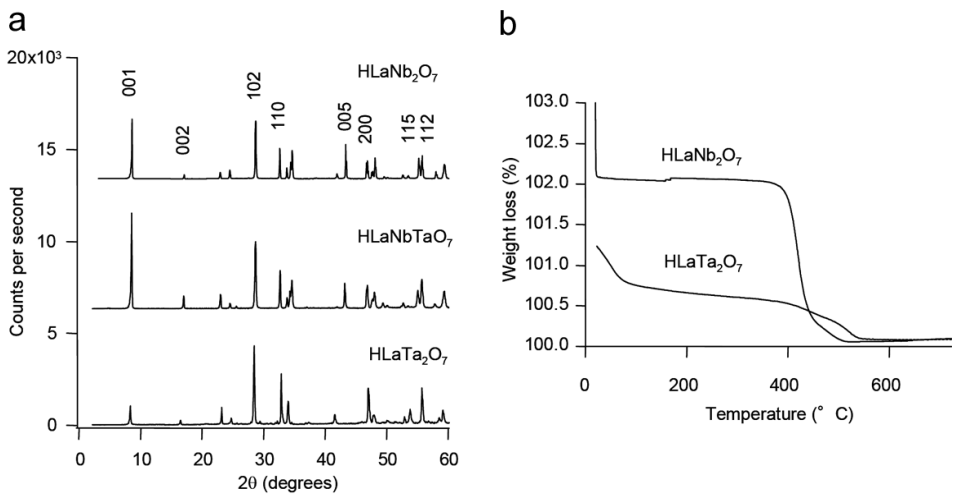


Figure 2.1: (a) XRD patterns of B-site $HLaNb_2O_7$ analogues, and (b) thermal gravimetry of $HLaNb_2O_7$ and $HLaTa_2O_7$ (1 °/min, equilibrated at 100% RH before analysis)

Impedance spectra of both materials are shown in Figure 2.2 and the intercept on the real axis (approx. 260 kΩ·cm here but ranging up to 600 kΩ·cm, depending on the sample) for $HLaNb_2O_7 \cdot 0.5H_2O$ corresponds reasonably well with that reported by Sato *et al* (approx. 400 kΩ·cm).[17] Sato *et al* conducted their lowest frequency measurements at 40 Hz, and since they observed only one semicircle they proposed that they could not resolve grain boundary and grain bulk components. When measurements are extended to 0.01 Hz as shown in Figure 2.2**,** the tail starts to curve into another semicircle, notably in the tantalum case. We postulate that the relaxation at high frequency is due to the grain surface conductivity while that at lower frequency is due to electrode polarization. Although higher temperature proton conductors, such as BCN18, have been reported to have quite low grain boundary conductivities,[20] our materials differ from these because in layered perovskites the conductivity does not originate from hydrated oxygen vacancies in the lattice; rather, conductivity originates from water adsorbed on surfaces. Grain bulk conductivity from interlayer hydrated protons in $HLaNb_2O_7$ is probably insignificant because the overall conductivity measured in air drastically decreased when the temperature was raised from ambient temperature to 110°C, despite the higher absolute humidity ($P_{H2O}$ = 0.3 atm as opposed to 0.03 atm). This agrees with results by Sato *et al,*

who found that the conductivity is related to water content and follows a Freundlich-type isotherm, $\sigma \alpha P_{H2O}^{1/n}$, where 1/n expresses the density of water adsorption on a rough surface.[17]

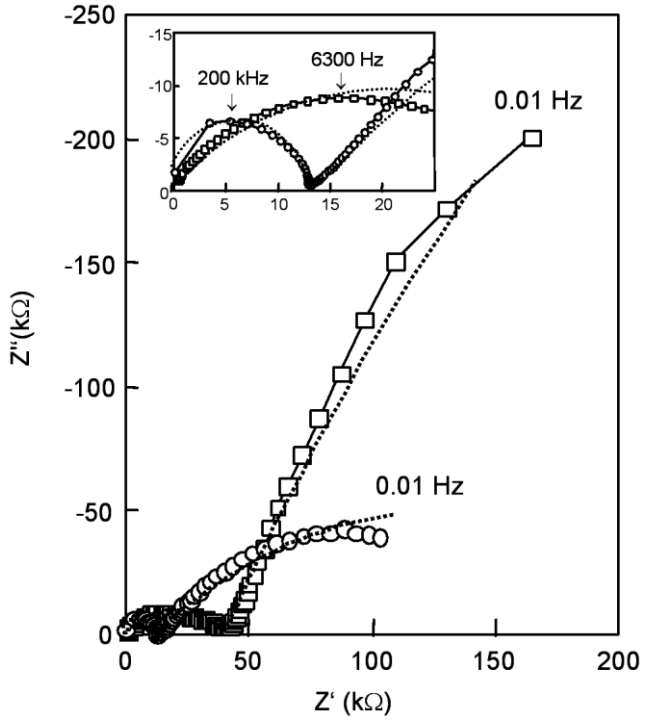


Figure 2.2: Impedance spectra (1 MHz - 0.01 MHz) at room temperature, under wet air ($P_{H2O}$ ) 0.03 atm). Dotted lines are fits to models shown in Figure 2.3. □: $HLaNb_2O_7 \cdot 0.5H_2O$, ○: $HLaTa_2O_7 \cdot 0.5H_2O$ (pellet with half the area).

An equivalent circuit shown in Figure 2.3 fits the spectra of the niobate and tantalate reasonably well, as shown by the dotted lines in Figure 2.2 (the actual model parameters are shown in Table 2.1). Since the semicircle features were depressed, constant phase elements (CPE) were used instead of capacitors in the actual modeling. The impedance of a CPE ($Z_{CPE}$) is described as following in Equation 2.1

$$Z_{CPE} = \frac{1}{C(j\omega)^P} \qquad 2.1$$

where $C$ is the capacitance of an element that would be found if $P = 1$, $j$ is the square root of -1, $\omega$ is the frequency and $P$ is a unitless coefficient loosely related to the distribution of the relaxation times, with $P = 1$ corresponding to a single relaxation time.

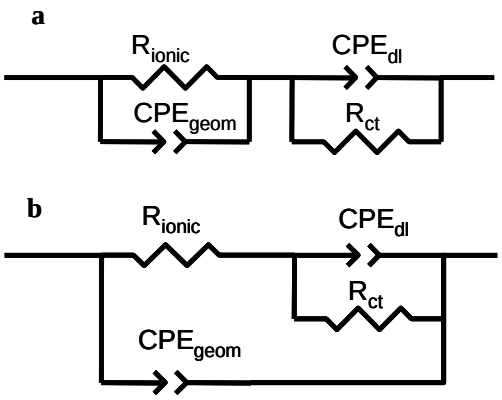


Figure 2.3: Equivalent circuit models

While an (RC)-(RC)-type arrangement shown in Figure 2.3a is perhaps more commonly encountered in the literature, we note that given the same R and CPE values, the circuit shown in Figure 2.3b gives exactly the same spectra as 2a does in both Nyquist and Bode plots. Other than the presence of $R_{ct}$, This second circuit is the same as the one used by Thangadurai *et al* to model electrolytes with blocking electrodes,[21] and provides a basis for the circuit shown in Figure 2.7b. For fitting, a least-squares optimization was initially conducted using the first model circuit, and it was confirmed that the second model circuit in Figure 2.3b gave the same impedance spectra. The results are summarized in Table 2.1.

Table 2.1: Fitted parameters on impedance spectra

| | $HLaNb_2O_7 \cdot 0.5H_2O$ | error (%) | $HLaTa_2O_7 \cdot xH_2O$ | error (%) |
|---|---|---|---|---|
| $R_{ionic}$ | 263 kΩ·cm | 1.4 | 41 kΩ·cm | 0.89 |
| $C_{geom}$ | 160 nF/cm$^2$ | 10 | 524 pF/cm$^2$ | 12 |
| $p_{geom}$ | 0.56 | 1.2 | 0.92 | 1.3 |
| $R_{ct}$ | 13 MΩ·cm | 93 | 630 kΩ·cm | 6.1 |
| $C_{dl}$ | 55 mF/cm$^2$ | 2.4 | 70 mF/cm$^2$ | 1.6 |
| $p_{dl}$ | 0.74 | 2.1 | 0.51 | 0.8 |

For these types of materials, $C_{geom}$ and $C_{dl}$ have been reported to be typically in the range of a few pF/cm$^2$ and μF/cm$^2$, respectively.[21] While the tantalate compound gives values of similar magnitude, it is not clear why $C_{geom}$ for the niobate is different. For other spectra reported here, it was difficult to fit $R_{ct}$ with high accuracy, often because the curvature of the semicircle was not very pronounced. The varying values of $R_{ct}$ are thought to be a reflection of the varying pseudo-blocking character of the Pt electrodes.

$HLaNb_2O_7$ is known to be reduced reversibly by $H_2$, even at ambient temperature.[22, 23] The equilibrium corresponding to a complete reduction can be expressed as follows:

$$H_2 + HLaNb_2O_7 \leftrightarrow HLaNb_2O_6 + H_2O$$

In terms of developing useful ionic conductors, this reaction is problematic, since the original compound is a Nb(V) compound and reduction gives a mixture of +V and +IV oxidation states, leading to electronic conduction. Focusing on the water by-product of the forward reaction, the redox equilibrium can be pushed backwards with the addition of water vapor to the hydrogen stream. An experiment (Figure 2.4) was run in which a small amount of $HLaNb_2O_7$ was heated in dry and wet hydrogen. In dry hydrogen, the material turned dark blue; this color change can be attributed to an intervalence charge transfer band centered at 1100 nm,[22] which indicates that the material has been reduced. However, the blue color does not appear when 0.3 atm of water vapor is added to the hydrogen stream, indicating that reduction has been suppressed substantially. Figure 2.5b shows electronic conductivity measurements of a $HLaNb_2O_7$ pellet, where the DC, or electronic conductivity has been lowered by an order of magnitude by the introduction of water. In Figure 2.5a, the sample was treated at the indicated temperature, and then, as the temperature was ramped down, the DC conductivity was measured. The figure shows that the activation energy for conduction remains fairly constant, regardless of the treatment, but it is the change in intercept, or density of charge carriers, that lowers the conductivity. This is consistent with the equilibrium shift mechanism mentioned earlier,

as the introduction of water vapor changes only the position of the equilibrium, and not the mechanism for electronic conduction. The sample treated under dry hydrogen at 450°C is an *n*-type semiconductor with an activation energy for conduction of 0.77 eV. As Palacin *et al* found,[23] plotting $-\ln(\sigma)$ vs. $1/(T^{1/4})$ failed to give any significantly better fits to the data, so it is not clear whether a variable range hopping mechanism is operative or not.[24]

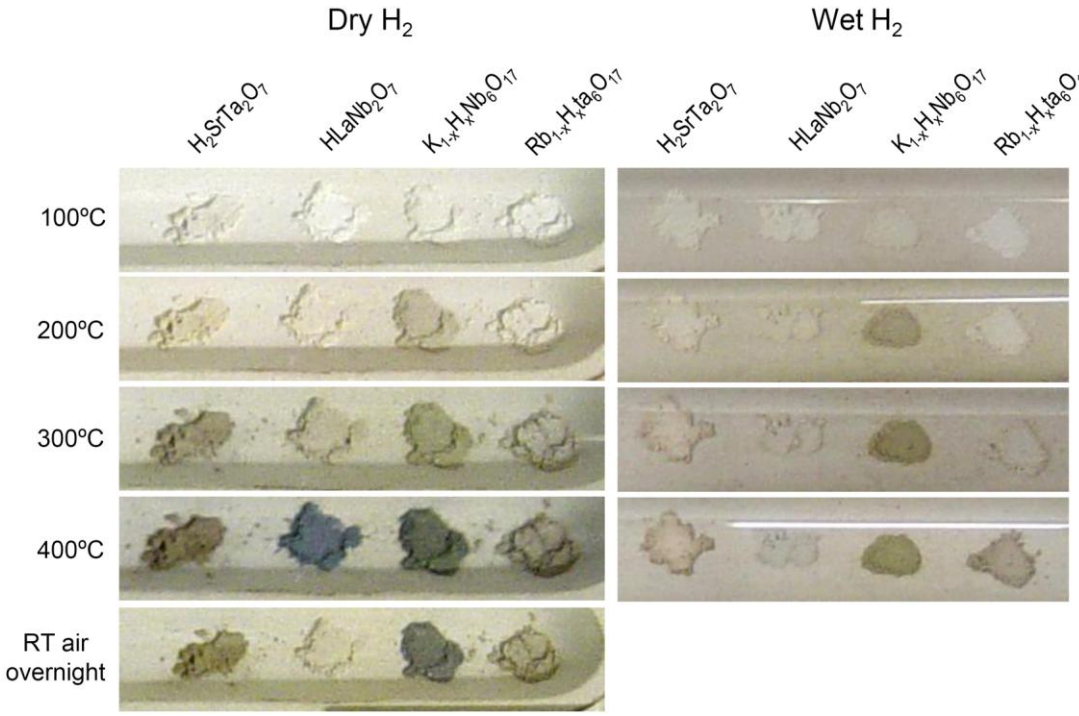


Figure 2.4: Reduction of $HLaNb_2O_7$ and other oxides under dry/wet hydrogen ($P_{H2O}$ = 0.3 atm). The temperature was ramped upwards after holding at each temperature for 30 min.

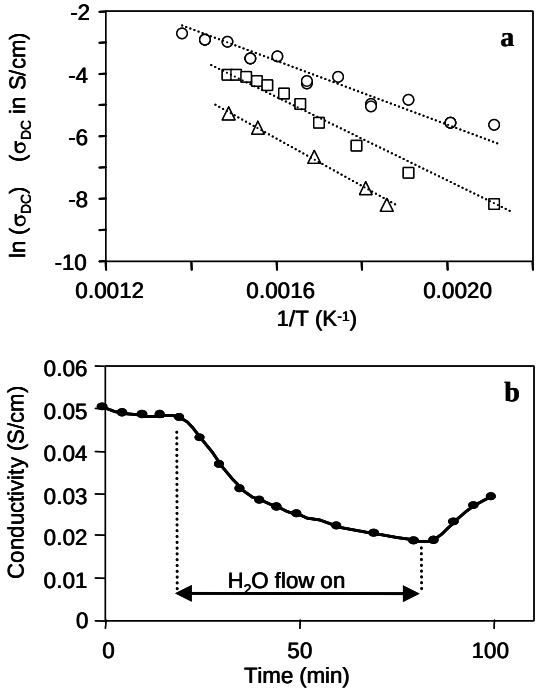


Figure 2.5: DC conductivity of $HLaNb_2O_7$ under various conditions

a) Effects of $H_2$ pre-treatment on $\sigma_{DC}$ of $HLaNb_2O_7 \cdot 0.5H_2O$ ($P_{H2O}$ = 0.3 atm); ○: 450 ºC dry $H_2$; □: 400 ºC dry $H_2$; △: 400 ºC wet $H_2$
b) Effect of water on DC conductivity under $H_2$ at 400 ºC, $P_{H2O}$ = 0.3 atm

Because the niobium cation is easier to reduce to lower, stable oxidation states (as in NbO, $NbO_2$, etc) than is the tantalum cation, the analogous Dion-Jacobson phase was synthesized with tantalum as the B-site cation, in order to suppress electronic conductivity. Figure 2.6 shows that the electronic conductivity is suppressed by several orders of magnitude, particularly at intermediate temperatures.

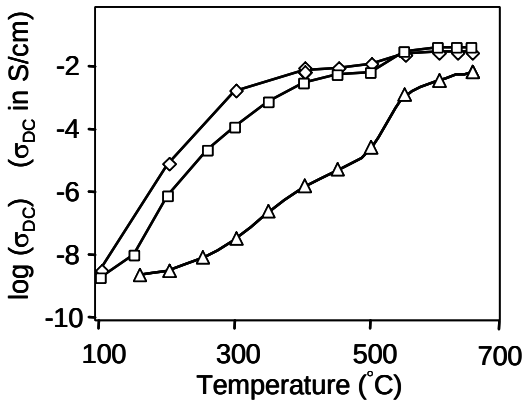


Figure 2.6: DC conductivity of $HLaABO_7$ (A, B = Nb, Ta) in dry $H_2$. ◇: $HLaNb_2O_7$; □: $HLaNbTaO_7$; △: $HLaTa_2O_7$.

**Effect of Hydrogen and Elevated Temperature on Impedance**

Since these materials were studied as potential candidates for intermediate temperature fuel cell membranes, it is important to know how stable they are at elevated temperatures and under reducing conditions. Figure 2.7a shows impedance spectra for $HLaNb_2O_7 \cdot 0.5H_2O$ and $HLaTa_2O_7 \cdot xH_2O$ in contact with humidified $H_2$ and air. Here, the niobate compound loses its low frequency tail when the atmosphere is switched to wet hydrogen, but the same effect is not seen for the tantalate. The model in Figure 2.7b explains the difference in the impedance behavior. Under wet air, there is very little electronic conductivity in either material, so the equivalent circuit previously shown in Figure 2.3 is adequate to model the spectra. Under wet hydrogen, however, the equivalent circuit is shorted by an electronically conducting pathway, shown by $R_{elec}$ in Figure 2.7b. This results in a lack of tail at low frequencies, which explains why the shape is changed when wet hydrogen is applied. Ideally, the circuit in Figure 2.7b should show two semicircles; a low frequency relaxation with its real intercept at $R_{elec}$ and another one at higher frequency with an intercept equal to $(R_{elec}^{-1} + R_{ionic}^{-1})^{-1}$. We do not see this probably because the RC components are not separated enough from each other and the

semicircles are depressed. While this makes it difficult to obtain an unambiguous fit, the solid lines shown in Figure 2.7b show that it is possible to model the spectra of the niobate in wet $H_2$ by simply adding an $R_{elec}$ component (108 kΩ·cm) while keeping $R_{ionic}$ the same as before reduction (140 kΩ·cm). The reasons for the conductivity in the tantalate *decreasing* slightly when exposed to wet hydrogen (Figure 2.7a) are not known. In general, the results from Figure 2.7 indicate that, even at room temperature under humidified conditions, $HLaNb_2O_7 \cdot 0.5H_2O$ is reduced to form a mixed ionic-electronic conductor.

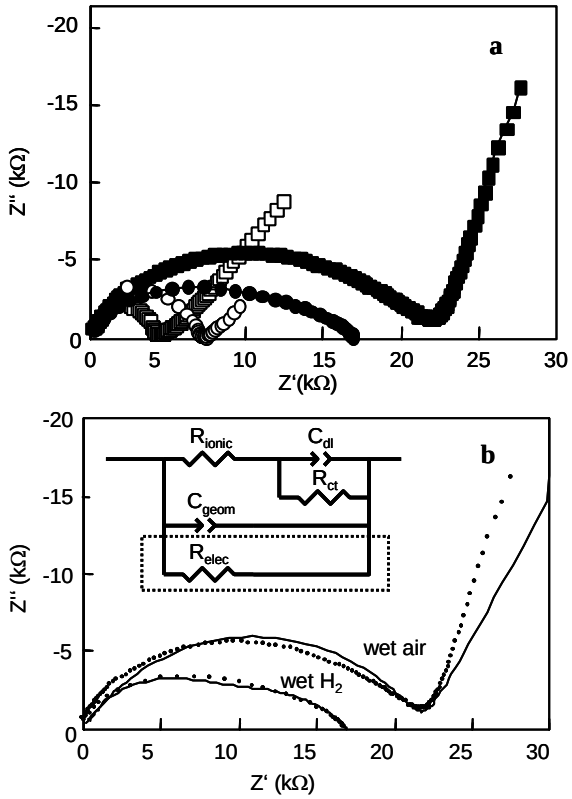


Figure 2.7: Impedance spectra of $HLaNb_2O_7 \cdot 0.5H_2O$ and $HLaTa_2O_7 \cdot xH_2O$ at room temperature under humidified air and $H_2$ ($P_{H2O}$ = 0.03 atm). Frequencies range 1MHz – 0.1 Hz.

a) □: $HLaTa_2O_7 \cdot xH_2O$, wet air, 5.5 hrs
   ■: $HLaNb_2O_7 \cdot 0.5H_2O$, wet air, 5.5 hrs
   ○: $HLaTa_2O_7 \cdot xH_2O$, wet $H_2$, 1 hr
   ●: $HLaNb_2O_7 \cdot 0.5H_2O$, wet $H_2$, 1 hr
b) Spectra for $HLaNb_2O_7 \cdot 0.5H_2O$ in different atmospheres, reproduced from a). Modelled results are shown by solid lines, and $R_{elec}$ was added for the wet $H_2$ sample.

Higher temperature measurements on $HLaNb_2O_7$ under humidified $H_2$ are shown in Figure 2.8. At 110°C, a flattened semicircle is observed, similar to that seen in Figure 2.7. This feature gradually changes into a single semicircle as the temperature is increased. As the temperature is increased, the niobate is progressively reduced, which, in terms of Figure 2.7b, implies a decreasing $R_{elec}$, resulting in the lower frequency semi-circle becoming smaller. The end result is a single semicircle obtained at 400 °C

(Figure 2.8). Here, the material is reduced to a predominantly electronic semiconductor, which is modeled by a parallel $R_{elec}C_{geom}$ circuit, showing a single semicircle with no tail**.** Upon cooling in the humidified $H_2$ stream, the material remains an electronic semiconductor, and thus the shape remains constant. The semicircle increases in size, however, since the material is a semiconductor and electronic conductivity decreases as the temperature decreases.

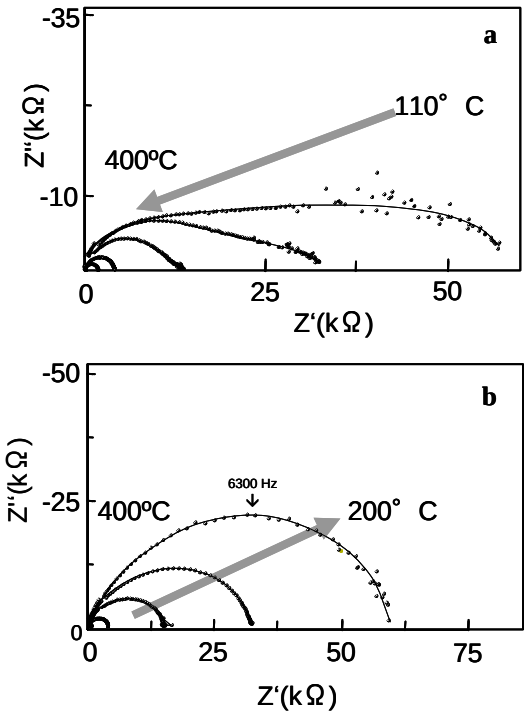


Figure 2.8: Impedance spectra of $HLaNb_2O_7$ at elevated temperatures in humidified hydrogen ($P_{H2O}$ = 0.3 atm) upon heating (a) and cooling (b).

**Characterization of Pillared Samples**

Trace (a) in Figure 2.9 is the X-ray diffraction pattern of the parent material $HLaNb_2O_7$. The reflection at 8.4° indicates an interlayer (00l) spacing of 10.4 Å. Stepwise intercalation of hexylamine, decylamine, and the organosiloxane modifies the layer to 24.2 Å, 29.4 Å, and approximately 23.4 Å, respectively. The organosiloxane

seems to intercalate better when dissolved in ethanol rather than when treated as a sol in water. However, calcining the former sample led to a smaller interlayer spacing and smaller surface area.

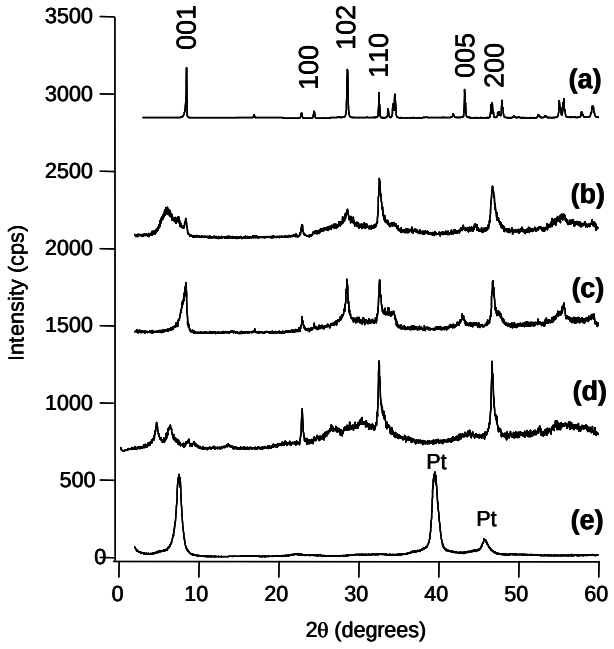


Figure 2.9: X-ray diffraction patterns of $HLaNb_2O_7$ with a modified layer structure. The individual traces are (a) parent $HLaNb_2O_7$, (b) restacked $HLaNb_2O_7$, (c) heat treated $HLaNb_2O_7$, (d) silica-pillared $HLaNb_2O_7$, and (e) cast $HLaNb_2O_7$ film on Pt/glass.

Thermal gravimetry coupled with mass spectrometry showed that both materials can be calcined at 450 °C to 500 °C to remove all organic traces. X-ray diffraction shows, however, that calcination at higher temperatures collapses the pillars. BET surface area measurements for both samples gave surface areas of 13.5 $m^2/g$ for the water sol sample and 9.1 $m^2/g$ for the ethanol solvent sample, while the original unpillared $HLaNb_2O_7$ has a surface area of less than 1 $m^2/g$. Scanning electron microscopy images of the pillared material are shown in Figure 2.10. EDS showed abundant silicon. The surfaces of the

particles appear to be relatively smooth, however, and this implies that the high surface area is due to silica pillaring rather than a porous layer of silica forming on the external surface of the lanthanum niobate particles.

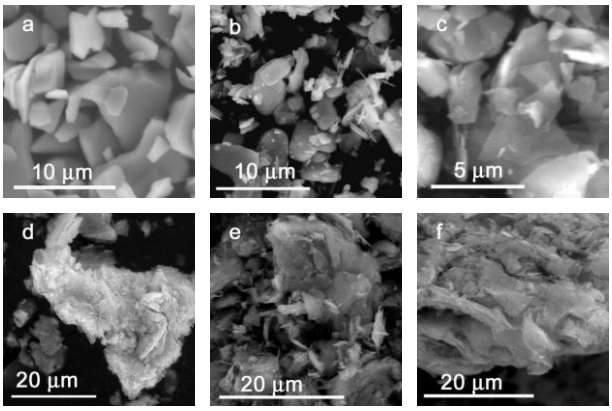


Figure 2.10: Scanning electron microscopy images of various modified $HLaNb_2O_7$ samples. (a) parent $HLaNb_2O_7$, (b) $HLaTa_2O_7$, (c) silica-pillared $HLaNb_2O_7$, (d) restacked/UV-$O_3$ treated $HLaNb_2O_7$, (e, f) further heat treated (d).

**Characterization of Flocculated Samples**

$HLaNb_2O_7$ was exfoliated into nanometer-thick and micron-wide sheets by stirring in excess aqueous TBAOH. When flocculated by addition of acid, the sheets re-assemble in a disordered manner, as can be seen in the X-ray diffraction comparison in Figure 2.9b. The broadened and shifted 00l line indicates that the layered structure has been severely altered, with most layers further apart from each other than in the parent compound. The loss of intensity in the three dimensional reflections, such as 102, in comparison with the 110 line, implies that the layers are disoriented with respect to each other, and the asymmetric profile of the 110 line also implies that the orientation between layers has been lost.[25] Nitrogen adsorption-desorption isotherms shown in Figure 2.11 exhibit large hysterisis for only the flocculated compound, implying the existence of mesopores. The BET surface area for this compound is 29 $m^2/g$, which is even larger than

that of the pillared samples. The material was treated with UV-$O_3$, but it is possible that some residual organics remain.

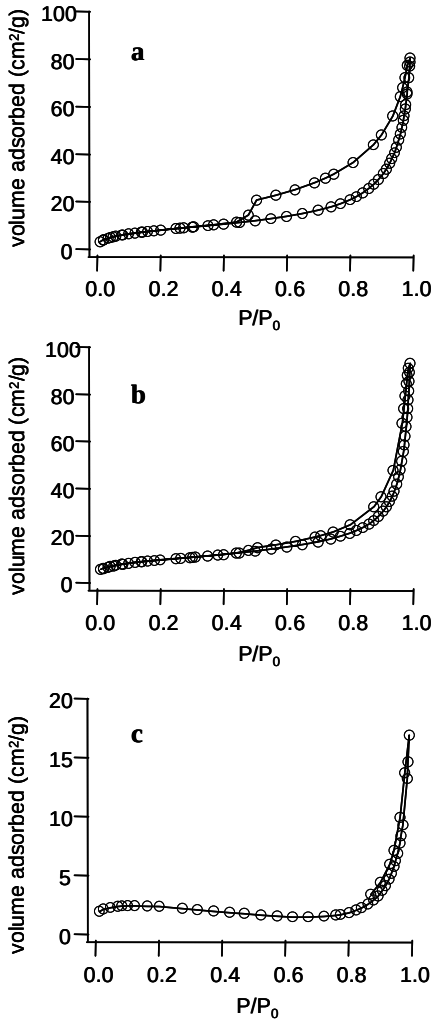


Figure 2.11: Nitrogen adsorption isotherms at 77K of (a) flocculated $HLaNb_2O_7$, (b) $HLaNb_2O_7$ flocculated and then annealed at 350 ºC, and (c) silica-pillared $HLaNb_2O_7$.

When the flocculated material was annealed in air at 350 °C overnight, the high surface area was retained (35 $m^2/g$). The mesopores have disappeared, however, as the isotherm in Figure 9b does not show adsorption-desorption hysterisis. The X-ray diffraction pattern shown in Figure 2.9c shows that much of the original layered structure was recovered, but with a noticeably smaller crystallite size. The slight increase in

surface area upon annealing may be due to residual organic material being removed during heating.

**Effect of Structure on Impedance Measurements**

In general, the room temperature impedance response for the parent material, the pillared, and annealed materials are largely similar (Figure 2.12a). At high frequencies, an experimental artifact where the impedance jumps into the second quadrant is seen; this is most likely due to phase shift in the operational amplifiers of the potentiostat. It is surprising that, although the pillared and annealed materials differ greatly in surface area and hence water adsorption capacity, the conductivity does not change significantly. The exception in Figure 2.12a is the response of the restacked but non-annealed $HLaNb_2O_7$ (inverted open triangles), which shows that the inside circle is much smaller than in the other samples. The moderately large surface area created by pillaring (9 $m^2/g$) does not have such a large effect on conductivity. Although the restacked material has an even larger surface area (29 $m^2/g$), the gain in conductivity obtained here is disproportionately large considering that increased surface area had no affect for the pillared sample.

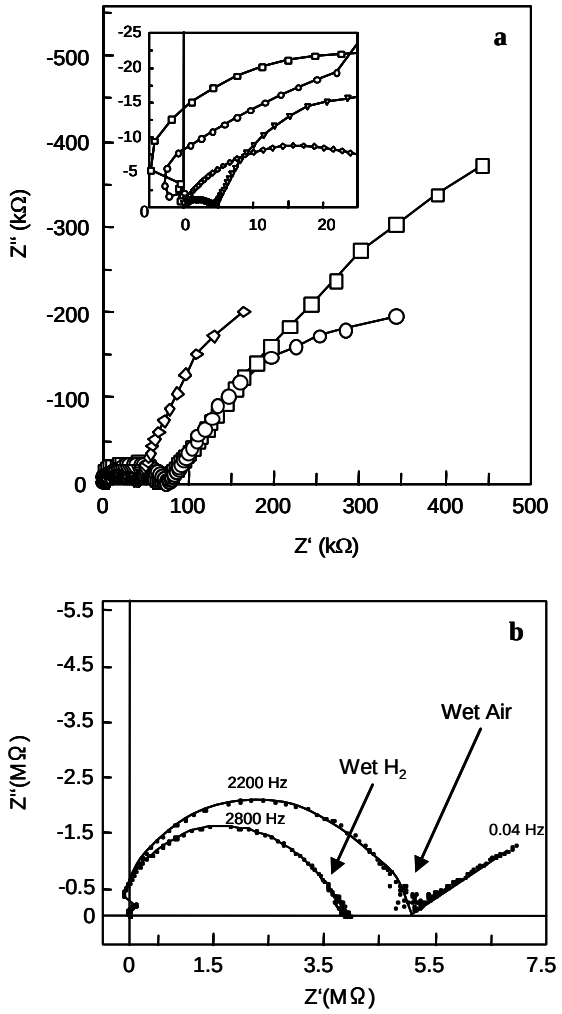


Figure 2.12: Impedance spectra for various modified $HLaNb_2O_7 \cdot 0.5H_2O$ samples at room temperature and 100% RH air equilibrated overnight. Lower limit of frequency is 0.01 Hz unless otherwise noted.

a) Various pelletized samples:
   ◇: original $HLaNb_2O_7 \cdot 0.5H_2O$
   □: $SiO_2$-pillared
   ▽: restacked
   ○: restacked, annealed
b) Comparison of oriented film under different atmospheres (equilibrated 1.5 hrs)

Furthermore, this enhanced conductivity of the restacked sample is lost when it is annealed to recover a regular layered structure. We assume that the annealed material has not been irreversibly dehydrated to $LaNb_2O_{6.5}$ during thermal annealing at 350˚C, since the position of the 001 line of the annealed material coincides with that of the parent $HLaNb_2O_7$. Instead, the difference in conductivity of the restacked material from others is perhaps due to structural differences illustrated schematically in Figure 2.13.

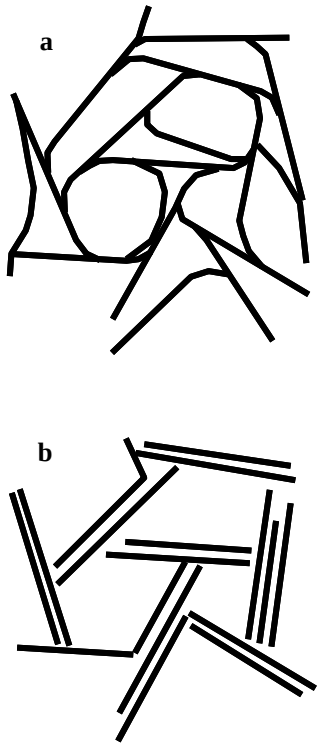


Figure 2.13: Schematics of structure in (a) restacked $HLaNb_2O_7 \cdot 0.5H_2O$ and (b) subsequent annealing at 350 ºC.

In all cases, we expect conduction to be due to grain surface conduction. We use the term grain *surface* as opposed to grain *boundary* because our sample pellets are not sintered and contain many voids. In the restacked material, the structure reflects the flexible nature of the exfoliated sheets—the individual sheets mesh well so that contact with each sheet occurs over a wide area, and there are many points of contact as sketched in Figure 2.13a. Therefore, the loss in conductivity due to sheet-to-sheet transfer is low. Once the material is annealed, however, X-ray diffraction shows the recovery of well

ordered layers. This is only possible if a granular structure with distinct grains and voids is recovered. Now, contact between each grain is more limited, and the overall conductivity is decreased. Because the grain-grain contact points are in series with the grain surface conduction pathways, however, we cannot distinguish them as independent relaxations in the impedance spectra.

An alternative explanation is that somehow the presence of mesopores as opposed to other pore diameters is crucial to the hydration of the surface and its effect on proton conductivity. The pillared sample, possessing very narrow pores, and the annealed sample whose surface area comes from inter-grain voids and simply thinner crystallites, did not show enhanced conductivity despite having a relatively high surface area.

**Effect of Orientation**

Ethanol suspensions of exfoliated $HLaNb_2O_7$ were deposited to form thin films on Pt contacts with a glass support. As the X-ray diffraction pattern in Figure 2.9 suggests, the layers are predominantly oriented parallel to the substrate plane. Immediately after deposition the interlayer distance has been expanded (d = 18.6 Å) due to intercalation of tetrabutylammonium hydroxide and perhaps residual solvent, but most of this can be removed by either UV-$O_3$ treatment or by thermal treatment at 350 °C.

In-plane measurements for the oriented film (70nm thick, 17mm wide, and across a gap 800 μm wide) yielded the impedance spectra shown in Figure 2.12b. As in the pellet case shown in Figure 2.6a, when treated with hydrogen the material becomes more conductive and shows no tail at low frequency, indicating that it is electronically conducting. For the film sample, the semicircle is less depressed since the grains are more aligned among themselves and with the Pt electrodes. This gives a well defined RC time constant, which results in a less depressed semicircle.

The resistance of the film at the intercept on the real axis of Figure 2.12b corresponds to a resistivity of 730 Ω·cm, whereas the pelletized samples typically are around 140-600 kΩ·cm. Thus, the oriented film is nearly three orders of magnitude more conductive than are the pellets with randomly oriented grains. This is expected given the

high aspect ratio of the sheets, and similar cases have been reported previously with oriented pellicular films of zirconium phosphate.[7, 26]

## Conclusions

Although $HLaNb_2O_7 \cdot 0.5H_2O$ readily reduces under hydrogen to give significant electronic conduction, its ionic conductivity can be increased significantly by exfoliation/flocculation to modify surface conduction pathways. This structure might be stabilized with inorganic pillars, so that it does not collapse at higher temperatures. Conduction pathways can also be optimized by preparing thin, oriented films. The electronic conductivity can be suppressed by the addition of water vapor and by substituting the B-site cation with a less reducible element, such as tantalum.

Continued efforts on this project should avoid the use of niobium compounds, if pure ionic conductivity is desired. The layered $Rb_4Ta_6O_{17}$ has been found to exfoliate into sheets (see next chapter), as does $RbTaO_3$ (Fukuda *et al*[27]). Both of these compounds do not have a perovskite structure; instead they are composed of a mixture of edge and corner-sharing $NbO_6$ octahedra. Perovskite monolayers tend to be quite dense and close-packed, as the voids between the corner-sharing octahedral are filled by the A-site cations. However, as Fukuda *et al* suggested for $RbTaO_3$, these non-perovskite layered tantalates may have channels just large enough for smaller ions such as protons to diffuse *through* rather than along the sheet surfaces. Such channel-type compounds could drastically enhance the ionic conductivity of these materials when prepared in membrane form.

Conduction *across* the membrane can also be achieved by changing the morphology of the particles. $H_2CaNaTa_3O_{10}$ is a Ruddlesden-Popper phase which when exfoliated and sonicated, produces extremely thin and long fibers. The fibers are similar to those $H_2SrTa_2O_7$,[28] but can be produced in almost quantitative yield. Preliminary experiments show that electrophoretic deposition of the fibers suspended in acetonitrile onto conducting substrates have readily yielded 1-3 micron thick matted films. In

summary, there are still many opportunities for further enhancing the ionic conductivity of these oxide films by simplying tuning the nanostructure.

## References


1. Norby, T. *Solid State Ionics* **1999,** *125*, 1-11.
2. Li, Q.; He, R.; Jensen, J. O.; Bjerrum, N. J. *Chem. Mater.* **2003,** *15*, 4896-4915.
3. J. A. Asensio, P. G. e.-R. *Fuel Cells* **2005,** *5*, 336-343.
4. Iwahara, H.; Uchida, H.; Ono, K.; Ogaki, K. *J. Electrochem. Soc.* **1988,** *135*, 529-533.
5. Du, Y.; Nowick, A. S. *Solid State Ionics* **1996,** *91*, 85-91.
6. Liang, K. C.; Du, Y.; Nowick, A. S. *Solid State Ionics* **1994,** *69*, 117-120.
7. Alberti, G.; Casciola, M.; Costantino, U.; Leonardi, M. *Solid State Ionics* **1984,** *14*, 289-295.
8. Boysen, D. A.; Uda, T.; Chisholm, C. R. I.; Haile, S. M. *Science* **2004,** *303*, 68-70.
9. Guo, C.-x.; Hou, W.-h.; Guo, M.; Yan, Q.-j.; Chen, Y. *Chem. Commun.* **1997**, 801-802.
10. Matsuda, T.; Udagawa, M.; Kunou, I. *Journal of Catalysis* **1997,** *168*, 26-34.
11. Schaak, R. E.; Mallouk, T. E. *Chem. Mater.* **2000,** *12*, 2513-2516.
12. Schaak, R. E.; Mallouk, T. E. *Chem. Mater.* **2002,** *14*, 1455-1471.
13. Matsuda, T.; Fujita, T.; Miyamae, N.; Takeuchi, M.; Kanda, K. *Bull. Chem. Soc. Jpn.* **1993,** *66*, 1548-1550.
14. Sato, M.; Abo, J.; Jin, T.; Ohta, M. *J. Alloys Compd.* **1993,** *192*, 81-83.
15. Thangadurai, V.; Shukla, A. K.; Gopalakrishnan, J. *Solid State Ionics* **1994,** *73*, 9-14.
16. Thangadurai, V.; Weppner, W. *Solid State Ionics* **2004,** *174*, 175-183.
17. Sato, M.; Jin, T.; Uematsu, K. *J. Solid State Chem.* **1993,** *102*, 557-561.
18. Macdonald, D. D.; Sikora, E.; Engelhardt, G. *Electrochim. Acta* **1998,** *43*, 87-107.

19. Gopalakrishnan, J.; Bhat, V. *Mater. Res. Bull.* **1987,** *22*, 413-417.

20. Norby, T.; Widerøe, M.; Glöckner, R.; Larring, Y. *Dalton Transactions* **2004**, 3012-3018.

21. Thangadurai, V.; Huggins, R. A.; Weppner, W. *Electrochemical Society Proceedings* **2001,** *2001-28*, 109-128.

22. Gomez-Romero, P.; Palacin, M. R.; Casan, N.; Fuertes, A. *Solid State Ionics* **1993,** *63-65*, 424-428.

23. Palacin, M. R.; Lira, M.; Garcia, J. L.; Caldes, M. T.; Casan-Pastor, N.; Fuertes, A.; Gomez-Romero, P. *Mater. Res. Bull.* **1996,** *31*, 217-225.

24. Mott, N., *Conduction in Non-Crystalline Materials*. Oxford University Press: Oxford, 1987.

25. Warren, B. E. *Physical Review* **1941,** *59*, 693-698.

26. Alberti, G.; Casciola, M.; Massinelli, L.; Palombari, R. *Ionics* **1996,** *2*, 179-183.

27. Fukuda, K.; Nakai, I.; Ebina, Y.; Ma, R.; Sasaki, T. *Inorg. Chem.* **2007,** *46*, 4787-4789.

28. Schottenfeld, J. A.; Kobayashi, Y.; Wang, J.; Macdonald, D. D.; Mallouk, T. E. *Chem. Mater.* **2008,** *20*, 213-219.

# Chapter 3

## A Scrolled Sheet Precursor Route to Niobium and Tantalum Oxide Nanotubes

## Introduction

Layered materials that can be exfoliated chemically to make unilamellar colloids possess the interesting possibility of re-stacking by scrolling into tubular morphologies. This has already been demonstrated in oxides such as $K_4Nb_6O_{17}$,[1, 2] and with non-oxide layered materials such as carbon[3] and the layered chalcogenides.[4] However, few studies exist on the transformation of these scroll structures, which are still layered in nature, to closed nanotubes. To date, most of the relevant studies concern titania nanotubes made from a scrolled layered alkali or protonated titanate.[5-11] However, this process remains limited in scope mainly to the formation of $TiO_2$ nanotubes and to single example with $MnO_2$ nanotubes.[12] Despite this, there exist many other layered oxides that readily exfoliate into unilamellar colloids. Among these, many are known to undergo topochemical reactions in the solid state.[13] Can these be scrolled and undergo further reaction to form nanotubes?

Several papers have been published on the spontaneous scrolling of $K_{1-x}H_xNb_6O_{17}$ upon exfoliation by aqueous tetra(*n*-butyl)ammonium hydroxide (TBAOH).[1] Because this is one of the few oxide materials that are known to scroll readily, we chose it to study the transformation into $Nb_2O_5$ nanotubes. Unfortunately, this transformation cannot happen topochemically, and the resulting nanotubes are therefore not single crystalline. However, we find that after thermal conversion, the nanotubular morphology is still preserved with some texturing despite the extensive rearrangement of atoms. This is an encouraging result as we attempt to identify other materials that can be scrolled (perhaps using methods recently developed by Ma, et al.[14]) and topochemically transformed into nanotubes.

## Experimental

$K_4Nb_6O_{17}$, $Rb_4Nb_3Ta_3O_{17}$, and $Rb_4Ta_6O_{17}$ were prepared by solid state reaction of $K_2CO_3$, $Nb_2O_5$, and $Ta_2O_5$. $Rb_2CO_3$ was added in 10% excess and $K_2CO_3$ was added in 20% excess to compensate for volatilization of alkali metal oxides. $K_4Nb_6O_{17}$ was prepared by firing at 1050-1100˚C for 10-24 hr, and $Rb_4Nb_3Ta_3O_{17}$ at 1100˚C for 40 hr. For $Rb_4Ta_6O_{17}$ the precursors were fired at 1100˚C for 40hr followed by grinding and additional heating at 1200˚C for 10hr. It should be noted that under most ambient conditions, $K_4Nb_6O_{17}$ partially hydrates making phase purity by XRD determination somewhat difficult. In these cases, it is sometimes advantageous to fully hydrate the sample by washing with water, and then fitting the pattern with an expanded basal lattice parameter to determine the phase purity.

The alkali compounds were exchanged to their protonated forms by shaking 0.2 g in 100 mL of 2 M nitric or hydrochloric acid for at least 5 days, during which the acid was exchanged three times. After 5 days, the acid was removed by centrifugation and the solid was washed three times with 50 mL portions of water. Exfoliation was carried out by adding the same batch of protonated material, isolated as a slurry, to aqueous 10 wt% tetra(n-butyl)ammonium hydroxide (TBAOH) solution (100 mL) and stirring for at least 4 days.

$TBA_xH_{1-x}Nb_6O_{17}$ was purified by washing away excess TBAOH by centrifugation, and the nanotubes were then precipitated by adding 0.5 M hydrochloric acid. The nanotubes were stirred in the acid solution overnight, and further washed the next day with water (three times) and ethanol (twice). The nanotube product was recovered in powder form by drying at 60 ˚C.

For attempts to prepare tubular $KNbO_3$ and $LiNbO_3$, 100 mg of $H_4Nb_6O_{17}$ scrolls or $Nb_2O_5$ nanotubes were reacted with 0.5 of $KNO_3$ or $LiNO_3$ salt in an alumina crucible for 24 hours at various temperatures ranging from 300 °C to 400°C for $LiNO_3$, and up to 450 °C for $KNO_3$.

Colloidal suspensions of the tantalum-substituted compounds in aqueous tetra(n-butyl)ammonium hydroxide were sonicated using a Branson 250 Sonifier for 15-45

minutes at an 80% output level and 70% duty cycle, before precipitation by slow addition of 100 mL 0.5 M HCl or 0.5 M $NH_4NO_3$ and isolation as a powder.

X-ray diffraction patterns were obtained on a Philips XPert or Scintag Pad diffractometer using Cu $K_\alpha$ radiation. Nitrogen adsorption isotherms were recorded on either a Micromeritics Accelerated Surface Area and Porosimetry System (ASAP) 2010 or 2020 unit. Pore size analyses was conducted according to either the Barrett, Joyner, and Halenda (BJH) theory, assuming both ends of the pores were open, or NLDFT theory. Before nitrogen adsorption isotherms were acquired, the samples were outgassed for at least 24 hours at 80 ˚C for $H_4Nb_6O_{17}\cdot nH_2O$ and 120 ˚C for $Nb_2O_5$ under dynamic vacuum. Transmission electron microscopy was conducted on either a Philips EM420 (operating at 120kV) or JEOL JEM-2010 microscope (operating at 200kV).

## Results and Discussion

The layered structure of $K_4Nb_6O_{17}$, is shown in Figure 3.1a. Each layer is composed of edge-sharing $NbO_6$ octahedra. Close examination reveals that for each layer, the top and bottom faces are different from each other, as exhibited by the different interlayer cation arrangements.[15] It is thought that this asymmetry in the faces of the sheets leads to spontaneous scrolling when the proton-exchanged compound $K_xH_{4-x}Nb_6O17$ is exposed to aqueous tetrabutylammonium hydroxide (TBAOH).[1] Figure 3.2a is an image of the $TBA_xH_{4-x}Nb_6O_{17}$ scrolls obtained after exfoliation and scrolling in aqueous TBAOH. As previous authors have noted, scrolling occurs in high yield, with diameters of about 30 nm and lengths of a few hundred nanometers. Based on statistical TEM measurements, Saupe et al and Du et al concluded that the scrolls are formed by exfoliated layers scrolling chiefly in the [100] direction, with the z axis of the original crystal structure as the tube axis.[1, 16] There was a small portion of unscrolled sheets also present in some batches. After scrolling and acid washing, the interlayers cations should be protons, as energy dispersive X-ray spectroscopy (EDS) showed no presence of

potassium and the IR spectrum shown in Figure 3.3 shows that there is probably only a trace amount of tetrabutylammonium.

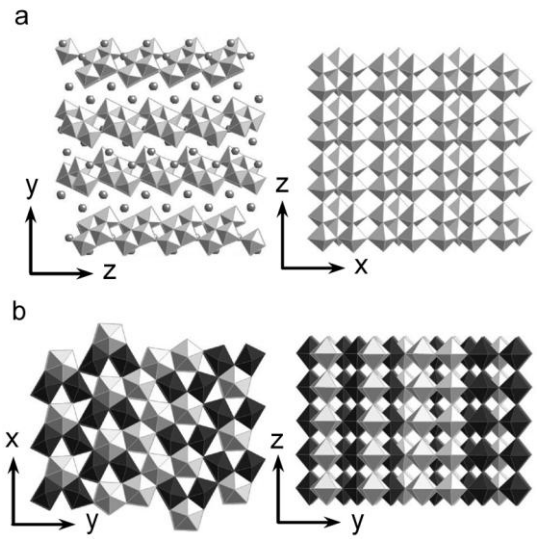


Figure 3.1: Crystal structure of (a) $K_4Nb_6O_{17}$ and (b) T-$Nb_2O_5$

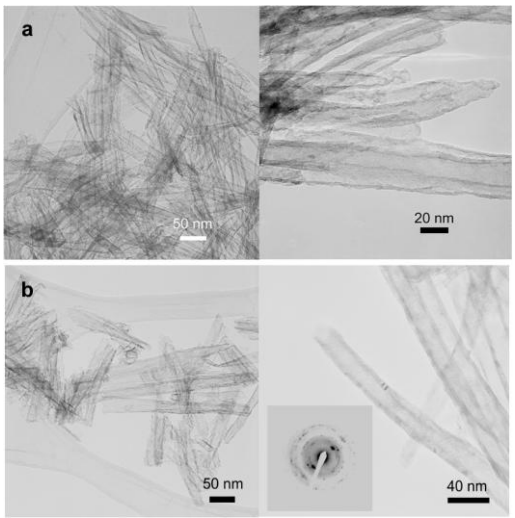


Figure 3.2: TEM images of (a) $H_4Nb_6O_{17}{\cdot}nH_2O$ scrolls, after isolation as a powder and of (b) $Nb_2O_5$ nanotubes obtained by treatment at 400˚C, 30 min (left) and 425˚C, 3 hr (right)

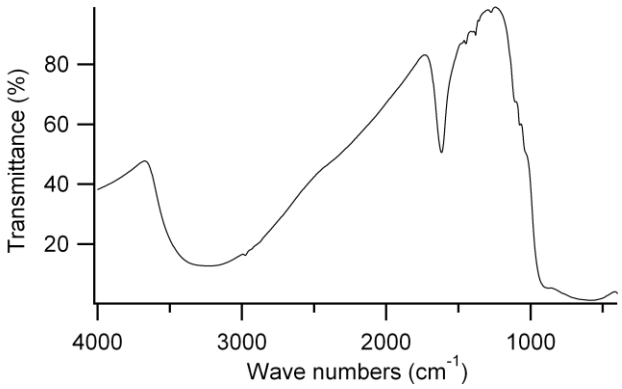


Figure 3.3: IR spectra of $H_4Nb_6O_{17}\cdot nH_2O$. The presence of only a very small peak at approximately 2950 $cm^{-1}$ (C-H stretching mode) indicates only trace amounts of tetrabutylammonium cations.

XRD patterns for the nanoscrolls isolated as powders are shown in the upper portion of Figure 3.4. The layered structure of $K_4Nb_6O_{17}$ is preserved within the scroll, as seen by the broad reflection at 5˚ and 040 reflection at about 11˚. The peak at 28˚ has become the strongest reflection, since it is the 002 reflection from lattice planes contained within one sheet; *hkl* reflections with two or more nonzero indices have been extinguished by the exfoliation and scrolling process. The XRD patterns in the lower panel of Figure 3.4 show the thermal conversion of the scrolls to $Nb_2O_5$. The structural details of this transformation are discussed in more detail below.

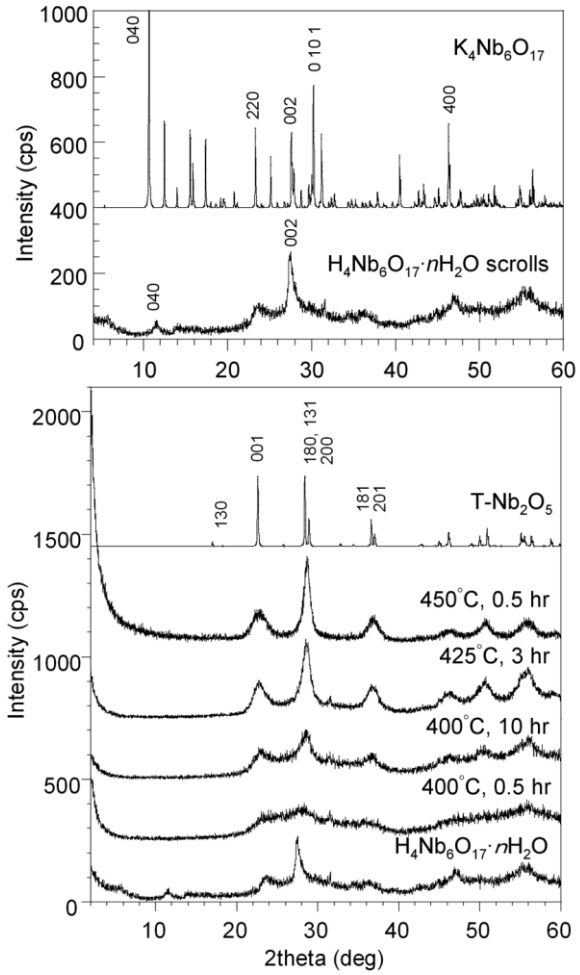


Figure 3.4: XRD patterns showing the transformation from $H_4Nb_6O_{17}\cdot nH_2O$ scrolls to $Nb_2O_5$.

Nitrogen adsorption isotherms of the scrolls and nanotubes were obtained to yield a Brunauer-Emmett-Teller (BET) surface area and pore size distribution according to BJH theory. The pore size distribution is shown in Figure 3.5 and a number of peaks are seen. Rather than indicating a pore, the sharp peak at 2nm is most likely due to a physical interaction between nitrogen and the sample, known as the tensile strength effect.[17] The peak is diminished when the adsorption data is modeled by an alternative theory such as density functional theory (DFT), as shown in Figure 3.6. The larger peak centered at 4 nm corresponds reasonably well with the inner radius measured from TEM images,

which for the $Nb_2O_5$ nanotubes was 5.4 ± 1.0 nm (S.D., $n$ = 41), hence we ascribe this feature to the pores from the individual nanotubes. Larger pores of approximately 20 nm radius are also observed, perhaps due to spaces between aggregates of tubes.

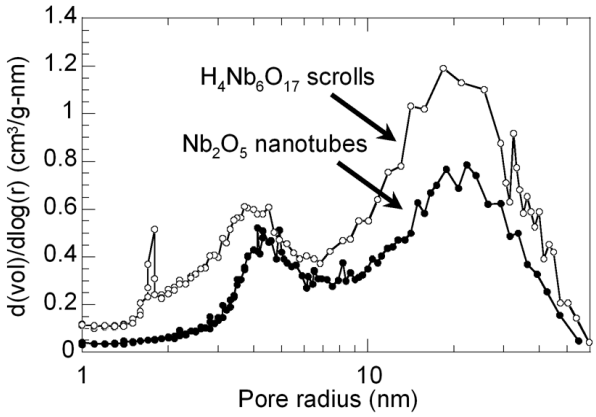


Figure 3.5: BJH pore size distribution of $H_4Nb_6O_{17}{\cdot}nH_2O$ scrolls and $Nb_2O_5$ nanotubes (nanotubes obtained after dehydration at 425 ºC for 3 hrs).

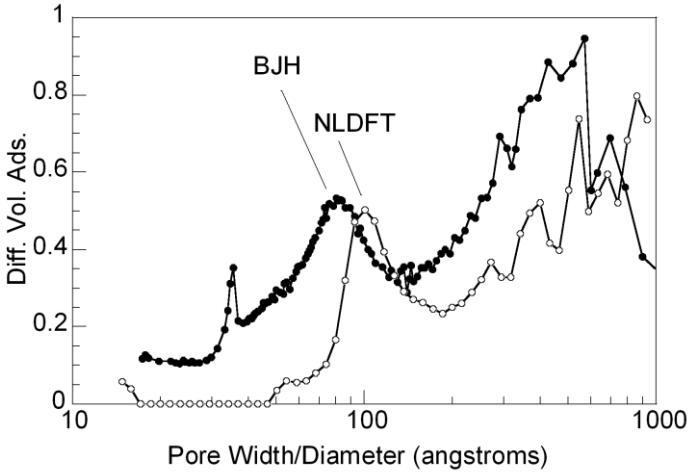


Figure 3.6: Comparison of pore size distribution of $H_4Nb_6O_{17}{\cdot}nH_2O$ scrolls according to BJH theory (cylindrical pores, measured by diameter) and NLDFT theory (slit pores, measured by pore width).

The BET surface area was approximately 250-300 $m^2/g$, with some variation from batch to batch. In general, the specific surface area (S) of a tube can be calculated geometrically from Equation 3.1 below:

$$S = \frac{(2\pi r_{OD} l) + (2\pi r_{ID} l)}{\left[(r_{OD}^2 - r_{ID}^2)\pi l\right] d} \qquad 3.1$$

where $r_{ID}$ and $r_{OD}$ are the inner and outer diameters of the tube, and $d$ is the density of the material. This equation can be simplified and rearranged to Equation 3.2, which yields the wall thickness (m), based on the surface area ($m^2/g$) and density ($cm^3/g$):

$$r_{OD} - r_{ID} = \frac{2 \times 10^{-6}}{Sd} \qquad 3.2$$

As mentioned above, depending on the batch, the surface area $S$ of the tubes ranged between 250 $m^2/g$ and 300 $m^2/g$. Based on lattice parameters from XRD experiments, the density of $H_4Nb_6O_{17} \cdot 4.4H_2O$ is 3.91 $g/cm^3$, and that of anhydrous $H_4Nb_6O_{17}$ is approximately 3.6 $g/cm^3$. If one chooses a value of 275 $m^2/g$ for the surface area, and sets the density to 3.75 $g/cm^3$, then the calculated wall thickness is 1.9 nm, corresponding to a scroll that is wrapped around 2-3 times. This is slightly smaller than most wall thicknesses (ranging from 2-5nm) observed in the TEM images.

**Characterization of $Nb_2O_5$ Nanotubes**

Because EDS spectra shows that the scrolls do not contain potassium, we may write the following Equation 3.3 for dehydrating the scrolls to convert them to $Nb_2O_5$ nanotubes:

$$H_4Nb_6O_{17} \cdot nH_2O \rightarrow 3\,Nb_2O_5 + 2+n\,H_2O \qquad 3.3$$

It is possible that some tetrabutylammonium cations remain in the scrolls. To ensure full exchange to the protonated form ($H_4Nb_6O_{17}$), after precipitation the exfoliated scrolls

were washed and stirred overnight in 0.5M nitric or hydrochloric acid. Thermal gravimetric analysis (see Figure 3.7) shows two weight losses between 230 ˚C and 450 ˚C, equivalent to a water loss of 1.9 mol, which is close to the 2 mol loss expected from Equation 3.3. We can therefore conclude that little tetrabutylammonium remains in the scrolls after acid washing, which agrees with the IR spectrum. We also see a significant weight loss centered at 100 ˚C, which sets $n$ in $H_4Nb_6O_{17}\cdot nH_2O$ at $n = 4.4$.

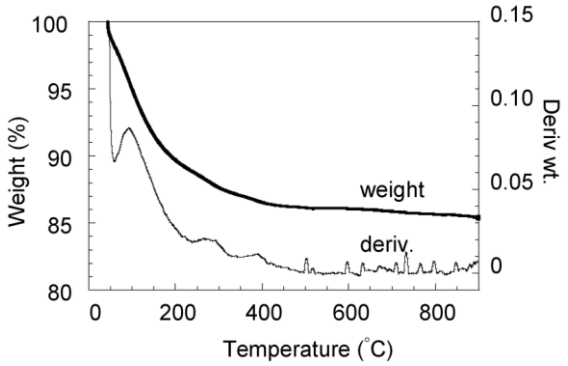


Figure 3.7: Thermal gravimetry of $H_4Nb_6O_{17}\cdot nH_2O$ scrolls. Data obtained under air, at a ramp rate of 15 ºC/min.

According to the thermal gravimetric results, dehydration is fairly complete at 425 ˚C. At this temperature, the tubes have not yet sintered, as can be seen in the TEM images of Figure 3.2b. The pore size distribution (Figure 3.5) is still centered on the same radius. The surface area of the tubes has decreased somewhat to 150-200 $m^2/g$. Most of this decrease is due to a change in the density of the material, rather than sintering. Upon formation of $Nb_2O_5$, the density of the material goes from approximately 3.75 $g/cm^3$ to 5.24 $g/cm^3$, resulting in a decrease in apparent surface area. Taking the surface area to be 175 $m^2/g$, the calculated tube wall thickness after dehydration is 2.2 nm, which again is slightly smaller than that observed by TEM; however, this is still consistent with the calculated wall thickness (1.9 nm) obtained before dehydration.

The series of XRD patterns in the lower panel of Figure 3.4 shows the scrolls as they are transformed into nanotubes at about 400 ˚C. Although many phases are known to exist for $Nb_2O_5$, a common progression found during the calcination of low-temperature precursors is (Equation 3.4):

$$TT \rightarrow T \rightarrow B/M \rightarrow H \qquad 3.4$$

where the actual transition temperature is dependent on precursors, impurities, etc.[18] In terms of X-ray diffraction the TT and T phases are difficult to distinguish, and in fact the T phase is thought to be simply a more ordered structure of the TT phase.[19-22] The structure of T-$Nb_2O_5$ is shown in Figure 3.1b. The *xy* plane is comprised of edge-shared $NbO_6$ and $NbO_7$ units. These are then linked by corner-sharing polyhedra along the *z*-axis to form the three dimensional structure. A small amount of additional Nb atoms (not shown) are scattered within the vacancies between the octahedral sites, in a loose six-fold coordination.[19, 20]

Looking back at the edge-sharing network of purely octahedral units in $K_4Nb_6O_{17}$, it is clear that conversion to TT,T-$Nb_2O_5$ requires long-range diffusion of Nb and O atoms; in other words the dehydration reaction cannot be topochemical. Hence, it would be difficult for a single crystal nanotube to result. The electron diffraction pattern of an individual nanotube is shown in Figure 3.2b, and shows evidence of multiple crystallites.

In order to determine crystallite sizes, the Scherrer equation was used to analyze the widths of the 28˚ (180, 131, 200) and 22˚ (001) diffraction peaks (Figure 3.4). For the sample heated to 400$^o$C, both peaks yielded crystallite sizes of approximately 4-5nm, although it was hard to make an accurate determination because of excessive broadening in the lower angle peak and the contribution of two overlapping reflections to the higher angle peak. At 450˚C, the crystallite size $L_{001}$ is approximately 4nm, whereas $L_{180,\ 131,\ 200}$ is approximately 10nm. This is noteworthy given that the tube wall thicknesses are on the order of 2-3 nm, smaller than the crystallite size determined from $L_{180,\ 131,\ 200}$. Although TEM images show that the tubes have started to sinter at 450˚C, there is a possibility that the anisotropy in crystallite size may be due to preferred orientation of the crystallites within the tube, with the 00l planes parallel to the tube walls.

The TEM image shown in Figure 3.8, combined with dark field imaging supports this proposed texture. Figure 3.8a shows a single tube and its corresponding selected area electron diffraction (SAED) in the inset. In the SAED pattern, points A correspond to 001 type planes (d = 3.93 Å), whereas points B correspond to 180 type

planes (d = 3.14 Å). Dark field imaging of the 001 spots (Figure 3.8b) illuminated the same areas as shown in the lattice fringe insets, where the fringes run parallel to the tube walls. This means that the lattice fringes are due to 001 reflections, and the planes run parallel to the tube walls. Another example is shown in the images Figure 3.8d-e. In Figure 3.8e, crystallites with their 001 planes parallel to the electron beam have been illuminated. All of the illuminated crystallites are positioned on the wall areas of the tube, whereas in Figure 3.8f the crystallites with the 180 planes parallel to the beam are less localized on the walls of the tube. In either 001-dark field image, the entire walls are not illuminated since the tube walls are not thick or crystalline enough in all regions to provide enough diffraction contrast; close examination shows that the illuminated areas tend to be the thicker, darker sections of the tube walls in the bright field images. Nevertheless, the important point is that when the 001 crystallites are illuminated, they tend to localize on the tube walls, while the 180 crystallites do not; furthermore, the lattice fringes are parallel to the tube walls, which implies that there is a substantial degree of texturing with the 001 planes parallel to the tube walls.

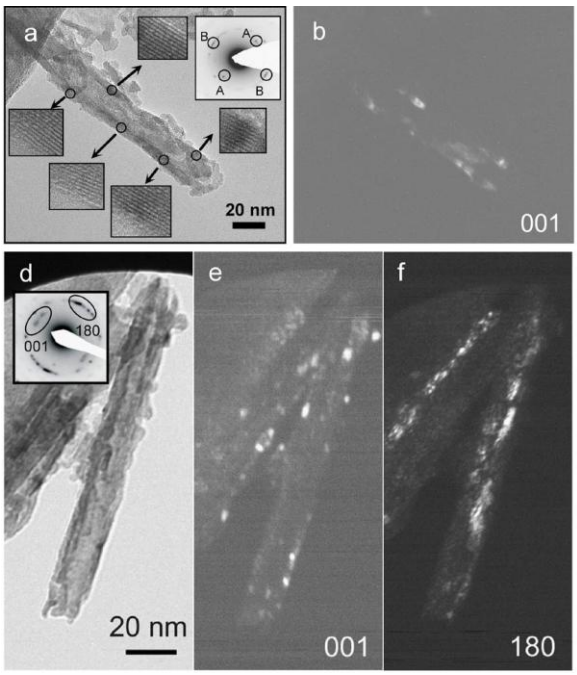


Figure 3.8: Bright field and dark field images of single $Nb_2O_5$ nanotubes

**Scrolling behavior of $TBA_xH_{4-x}Ta_6O_{17}$ and $TBA_xH_{4-x}Nb_3\ Ta_3O_{17}$**

Substituting tantalum for niobium had a somewhat surprising effect on the exfoliation behavior. Instead of forming scrolls, $TBA_xH_{4-x}Nb_3Ta_3O_{17}$ exfoliated to initially give predominantly large micron-sized sheets. Sonicating the suspensions with a probe consistently yielded a higher yield of $Nb_3Ta_3$ scrolls. Similar results were obtained with a $Ta_6$ sample, although in this case the scrolling yield depended on the batch. In general, complete conversion to scrolls was not observed in either case. Apparently, with Ta-substituted compounds, neither sonication nor sheet size affects the ability to scroll. Sheets caught in the act of scrolling can be seen in Figure 3.9. Unlike $K_4Nb_6O_{17}$, where a preferred scrolling direction has been reported, these semi-scrolled sheets seem to have no preferred scrolling direction. Some sheets were seen to be scrolling on all sides, and with the two scrolling edges are not at right angles to each other

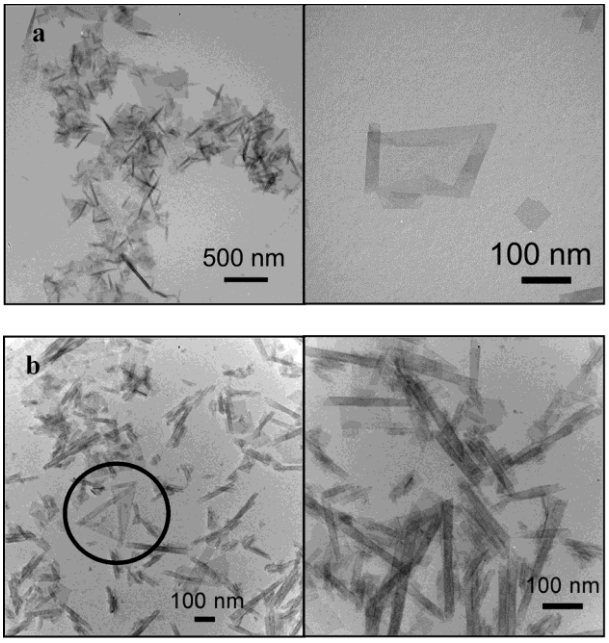


Figure 3.9: TEM images of (a) $TBA_xH_{1-x}Nb_3Ta_3O_{17}$ and (b) $TBA_xH_{1-x}Ta_6O_{17}$

Is it possible that substitution with tantalum, whether it be partial or full, decreases the ability to scroll by alleviating the stress in the layers? Comparison by Rietveld refinement of the tantalates was difficult since both tantalates partially hydrate

in atmosphere to a less crystalline material. It is possible that stress is relieved by Ta substitution, because of its slightly larger size and greater tendency, relative to Nb, to adopt a regular octahedral coordination geometry.

**Reactions with lithium and potassium salts**

If a non-topochemical reaction such as the conversion from $H_4Nb_6O_{17}$ to $Nb_2O_5$ can be can be carried out while preserving the tubular morphology, then it is possible that $H_4Nb_6O_{17}$ nanoscrolls or $Nb_2O_5$ nanotubes can be reacted with other materials to yield other nanotubes. Although the tubes sinter at temperatures above 450 ˚C, the diffusion length needed for the solid-state reaction may be short enough so that reactions occur below the sintering temperature. In order to test this hypothesis, both $H_4Nb_6O_{17}$ scrolls and $Nb_2O_5$ nanotubes were reacted with molten $LiNO_3$ or $KNO_3$ at various temperatures. As shown in Figure 3.10, $Nb_2O_5$ and $H_4Nb_6O_{17}$ nanotubes indeed formed $LiNbO_3$ when reacted at 350˚C – 400˚C. The formation of $KNbO_3$ from $H_4Nb_6O_{17}$, however, seems to demand higher temperatures. Sharp diffraction lines in the case of $LiNbO_3$, however, show that the phase has large crystallites, and indicates that the tubular nanostructure has most likely been lost. It appears that while the tubular structure can tolerate dehydration reactions, the tubes may dissolve to some extent in the flux, resulting in a dense product.

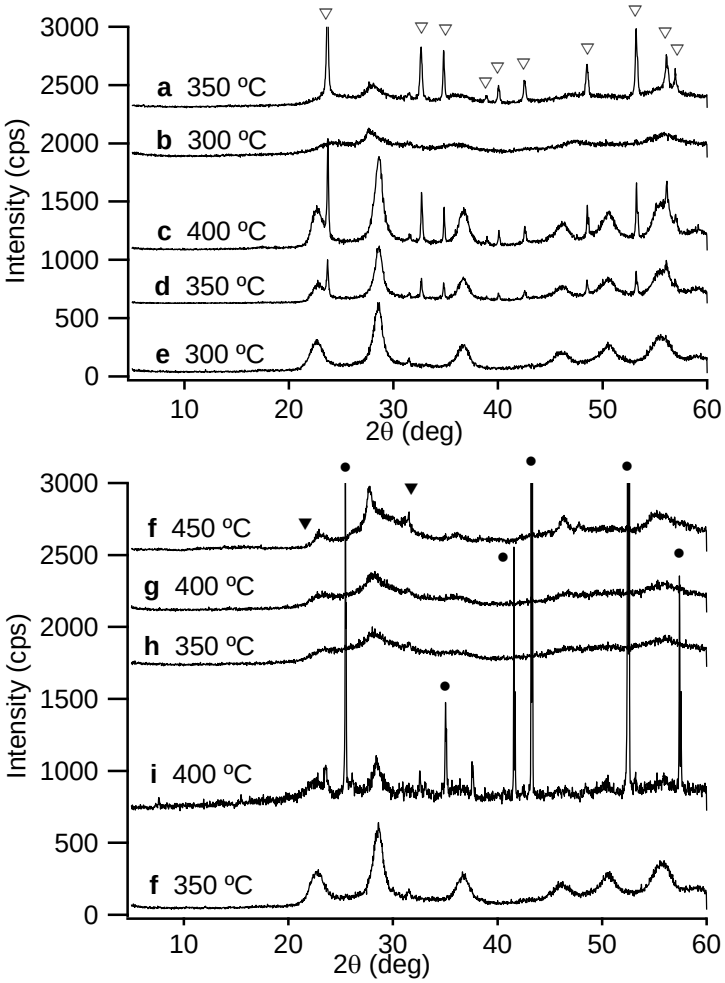


Figure 3.10: XRD patterns of products from reactions with $LiNO_3$ and $KNO_3$ with $Nb_2O_5$ nanotubes and $H_4Nb_6O_{17}$ scrolls.

a-b: reaction of $LiNO_3$ with $H_4Nb_6O_{17}$
c-e: reaction of $LiNO_3$ with $Nb_2O_5$
f-h: reaction of $KNO_3$ with $H_4Nb_6O_{17}$
i-f: reaction of $KNO_3$ with $Nb_2O_5$

## Conclusion

In conclusion, $H_4Nb_6O_{17}$ scrolls were successfully dehydrated to form high surface area T-$Nb_2O_5$ polycrystalline nanotubes. This successful example of a thermal scroll-to-tube conversion shows that in many systems it may be possible to conduct the conversion without sintering and destroying the desired morphology. The next step would be to scroll a layered precursor which may topochemically transform into a tube, potentially creating a single crystalline nanotube. An example of such materials would be the layered oxide $HTiNbO_5$, certain layered double hydroxides, or other Ruddlesden-Popper layered perovskites provided that they may be readily exfoliated.

## References


1. Saupe, G. B.; Waraksa, C. C.; Kim, H.-N.; Han, Y. J.; Kaschak, D. M.; Skinner, D. M.; Mallouk, T. E. *Chem. Mater.* **2000,** *12*, 1556-1562.

2. Du, G.; Chen, Q.; Yu, Y.; Zhang, S.; Zhou, W.; Peng, L.-M. *J. Mater. Chem.* **2004,** *14*, 1437-1442.

3. Viculis, L. M.; Mack, J. J.; Kaner, R. B. *Science* **2003,** *299*, 1361.

4. Li, Y. D.; Li, X. L.; He, R. R.; Zhu, J.; Deng, Z. X. *J. Am. Chem. Soc.* **2002,** *124*, 1411-1416.

5. Seo, D.-S.; Lee, J.-K.; Kim, H. *J. Cryst. Growth* **2001,** *229*, 428-432.

6. Wang, Y. Q.; Hu, G. Q.; Duan, X. F.; Sun, H. L.; Xue, Q. K. *Chem. Phys. Lett.* **2002,** *365*, 427-431.

7. Zhang, S.; Peng, L.-M.; Chen, Q.; Du, G. H.; Dawson, G.; Zhou, W. Z. *Phys. Rev. Lett.* **2003,** *91*, 256103.

8. Suzuki, Y.; Yoshikawa, S. *J. Mater. Res.* **2004,** *19*, 982-985.

9. Wei, M.; Konishi, Y.; Zhou, H.; Sugihara, H.; Arakawa, H. *Solid State Commun.* **2005,** *133*, 493-497.

10. Tsai, C. C.; Teng, H. *Chem. Mater.* **2006,** *18*, 367-373.

11. Wang, N.; Lin, H.; Li, J.; Zhang, L.; Lin, C.; Li, X. *J. Am. Ceram. Soc.* **2006,** *89*, 3564-3566.

12. Wang, X.; Li, Y. *Chem. Lett.* **2004,** *33*, 48-49.

13. Schaak, R. E.; Mallouk, T. E. *Chem. Mater.* **2002,** *14*, 1455-1471.

14. Ma, R.; Bando, Y.; Sasaki, T. *J. Phys. Chem. B* **2004,** *108*, 2115-2119.

15. Gasperin, M.; Le Bihan, M.-T. *J. Solid State Chem.* **1982,** *43*, 346-353.

16. Du, G. H.; Peng, L.-M.; Chen, Q.; Zhang, S.; Zhou, W. Z. *Appl. Phys. Lett.* **2003,** *83*, 1638-1640.

17. Groen, J. C.; Peffer, L. A. A.; Pérez-Ramírez, J. *Micropor. Mesopor. Mater.* **2003,** *60*, 1-17.

18. Schafer, H.; Gruehn, R.; Schulte, F. *Angew. Chem., Int. Ed.* **1966,** *5*, 40-52.

19. Kato, K.; Tamura, S. *Acta Crystallogr., Sect. B: Struct. Sci.* **1975,** *B31*, 673-677.

20. Tamura, S.; Kato, K.; Goto, M. *Zeitschrift fuer Anorganische und Allgemeine Chemie* **1974,** *410*, 313-315.

21. Weissman, J. G.; Ko, E. I.; Wynblatt, P.; Howe, J. M. *Chem. Mater.* **1989,** *1*, 187-193.

22. Gatehouse, B. M.; Wadsley, A. D. *Acta Cryst.* **1964,** *17*, 1545-1554.

# Chapter 4

## Soft Chemical Conversion of Layered Double Hydroxides to Superparamagnetic Spinel Platelets

## Introduction

The layered double hydroxides (LDHs) and brucite-type divalent metal hydroxide salts are a versatile class of lamellar compounds, which can be made to incorporate a broad range of trivalent and/or divalent metal cations. There are numerous reports of thermally decomposing these LDHs into porous mixtures of spinels and other metal oxide phases;[1-4] and a few reports of the phase pure preparation of spinels[5-9] via a topochemical reaction.[10] However, as a synthetic route to new spinels or to particles of known composition with nanoscale dimensions, this layered precursor method has not yet been exploited. An advantage of this solid state precursor method is the low temperature of the topochemical transformation, allowing metastable spinels to be prepared. While there is one report commenting that the layered precursor route seems to be useful for metastable compositions,[9] most of the previous literature describes the synthesis of spinels that are accessible by high-temperature methods. Furthermore, in earlier reports the layered precursors were poorly crystalline or had rather undefined particle shapes. Recent advances in the synthesis of highly crystalline LDH and brucite-type platelets of various transition metal compositions by Liu, Ma, and others[11-13] now make it possible to synthesize transition metal LDHs and brucite-type structures as extremely well-defined, single crystalline platelets. These are hexagonally shaped platelets that are typically about 20 nm thick and one micron wide, prepared by the homogeneous coprecipitation of metal salts.

Building on these new synthetic developments, we now report the transformation of single crystalline layered metal hydroxide precursors to spinel products, starting with simple cobalt hydroxide salts and proceeding to ternary LDH precursors. We find that the

layered precursor method uniquely permits the synthesis of metastable ternary spinels such as $NiCoAlO_4$ with well defined morphology and high crystallinity. Shape studies with anisotropic magnetic particles have been carried out, but they are usually limited to sphere or cube morphologies.[14] The formation of thin spinel platelets with a defined (111) face exposed makes them new targets for basic studies in magnetic anisotropy. The thin crystallite size (20nm), and perhaps in some cases the porosity of the newly prepared spinel platelets, gives them enhanced properties such as superparamagnetism, which are not typically observed in magnetic particles in the micron size range. Because of their superparamagnetism and shape anisotropy, these spinel platelets may exhibit interesting characteristics as ferrofluids, magnetic liquid crystalline colloids, or in magnetorheology. Thin films of spinel are also interesting for spintronics applications,[15] and these thin platelets may serve as building blocks for growing thin films under mild wet chemical conditions.

The LDH (hydrotalcite) structure consists of edge-sharing octahedral layers as shown in Figure 4.1a. This type of structure is rhombohedral ( $R\bar{3}m$ ) and consists of three layers within the unit cell along the c-axis, and so is sometimes referred to as the $3R_1$ polytype. Most LDHs crystallize in this structure, although some LDHs can crystallize as $3R_2$, $2H_1$ (as in the mineral manasseite), or 1H polytypes.[16] β-$Ni(OH)_2$ and $Fe(OH)_2$ are also known to crystallize in the same $3R_1$ type structure, and the structure of α-$Co(OH)_2$ is similar.[17] β-$Co(OH)_2$, however, crystallizes in a brucite structure ( $P\bar{3}m$ ), in which the layer stacking is different (1H) as shown in Figure 4.1b.

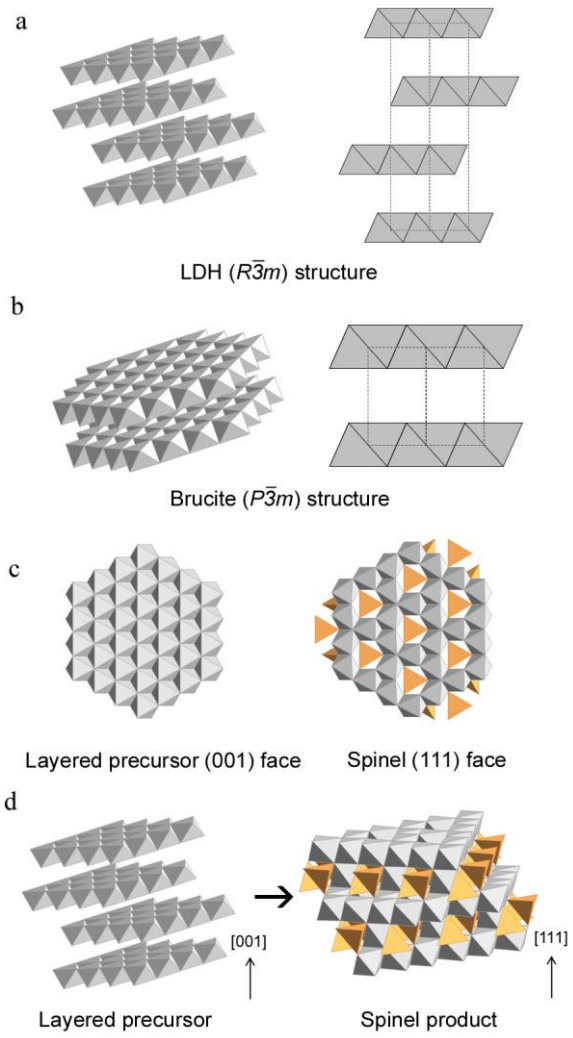


Figure 4.1: Diagrams of various crystal structures. (a) LDH structure, (b) brucite structure, (c) LDH (001) and spinel (111) faces, and (d) transformation from LDH platelet to spinel platelet with the (111) face exposed. Interlayer species have been omitted from the polyhedral representations of the structures.

The symmetry of the individual sheets closely resembles that of the (111) planes of the $Fd\bar{3}m$ spinel structure, shown in Figure 4.1c. We postulate that as the LDH is dehydrated and some of the metal ions are oxidized, ions within the octahedral layers leave to fill some of the interlayer sites and become the tetrahedrally coordinated cations of the spinel structure. The closely related symmetry of the LDH layers and spinel (111) planes permits the reaction to be fairly topotactic (within the precursor layer dimensions,

at least), and as Markov *et al.* observed, one expects the threefold axis of the LDH precursor to coincide with the [111] axis of the spinel product, as shown in Figure 4.1d.[10]

## Experimental Section

### Synthesis

#### *Heterometal LDHs $Co_2$Al-LDH, NiCoAl-LDH, $Ni_2$Al-LDH, ZnCoAl-LDH, FeCoAl-LDH*

The precursor LDHs were prepared following the method of Liu.[13] For heterometal LDH synthesis, nitrate salts of nickel, cobalt, and aluminum were used as precursors. The starting salts were in a $M^{+2}$:$M^{+2}$:$Al^{+3}$ = 1:1:1 ratio (2.5mmol each), and were dissolved in 500 mL of deoxygenated water. To this, 17.5 mmol of urea was added, and the solution was refluxed for 48 hours under nitrogen. $Ni_2$Al-LDH and NiCoAl-LDH was prepared on a smaller scale by dissolving the same ratio of precursors in 100 mL of water, and then heating for 2 days at 190˚C (150˚C for NiCoAl-LDH) in a 120 mL Teflon-lined Parr bomb purged with nitrogen before sealing. In preparing NiCoAl-LDH, it was necessary to extensively deoxygenate the nitrate salt solution prior to the reaction, otherwise a gray powder with spinel contamination would result instead of the off-pink pure compound. After reaction, the LDH samples were washed at least twice with deionized water, at least twice with ethanol, and then dried at 60˚C in air. Conversion to spinel was conducted by heating the various LDHs at 10˚C/min to a set temperature for 12 hours, and then cooling at a rate of 10˚C/min. Heat treatments at 500˚C or below were conducted under pure flowing $O_2$ instead of air. IR analysis on LDH precursors showed peaks at 1600 $cm^{-1}$ and 1490 $cm^{-1}$, indicating the presence of carbonate and nitrate anions as interlayer species. Elemental analysis from ICP-AES on $Co_2$Al-LDH and NiCoAl-LDH yielded metal ratios of Co:Al = 1.85:1.14 and Ni:Co:Al = 1.04:1.04:1, respectively.

EDS of numerous NiCoAl-LDH platelets showed a consistent elemental composition close to that obtained by ICP-AES.

***Preparation of amorphous NiCoAl-LDH***

The same molar amounts of nitrate salts were dissolved in 500 mL of deoxygenated water; to this, 2.36 mL of concentrated ammonium hydroxide (14.8M, 3.5 mmol) was quickly added under a nitrogen blanket. A purple-pink suspension quickly formed, which was aged for two hours. Another 2.36 mL of ammonium hydroxide was added again, resulting in no visible change. The suspension was stirred for a final 2 hours before being washed with deionized water and ethanol, during which the gel material increasingly turned darker in color to violet. Drying at 60˚C in air overnight yielded dark violet pellets, which produced a lavender powder upon grinding.

***Attempted preparation of $NiCoAlO_4$ from nitrate salts***

The same amount (2.5mmol each) of $Ni(NO_3)\cdot 6H_2O$, $Co(NO_3)\cdot 6H_2O$, and $Al(NO_3)\cdot 9H_2O$ was dissolved in 10 mL of ethanol, then concentrated using a rotavap. The resulting gel was heated to 120˚C for 10 minutes to yield a dry magenta foam, which was calcined at 350˚C in air for 1 hour, then under flowing oxygen for 12 hours at 500˚C.

***Attempted preparation of $NiCoAlO_4$ by the citrate gel method***

1.4540 g of $Ni(NO_3)_2\cdot 6H_2O$ (5 mmol), 1.4558 g of $Co(NO_3)_2\cdot 6H_2O$ (5 mmol), 1.8757 g of $Al(NO_3)_3\cdot 9H_2O$ (5 mmol), 5.774 g of citric acid (6 mmol), and 2.06 mL of ethylene glycol (6 mmol) was dissolved in 10 mL of water, and was boiled on hot plate. The mixture was stirred with a glass rod as a thick gel was obtained which finally became a thick paste; this was then cooled to room temperature, and ground to form a dry

powder. The powder was heated in air to 450˚C at 20˚C/min and kept at this temperature for 6 hours during which the furnace was briefly opened once for air exchange.

### *α-$Co(OH)_2$, β-$Co(OH)_2$, $Ni_{1/3}Co_{2/3}(OH)_2$*

The procedure of Liu *et al.* was followed,[11] where 2.974 g of $CoCl_2 \cdot 6H_2O$ (12.25 mmol) and 4.206 g of hexamethylenetetramine (30 mmol) were dissolved in 500 mL of a water-ethanol mixture (450 mL, 50 mL). The solution was refluxed for 1 hour under nitrogen, after which the green precipitate was collected and washed with deionized water and ethanol. The product was dried at 60˚C overnight in air.

For β-$Co(OH)_2$, 0.8919 g of $CoCl_2 \cdot 6H_2O$ (3.75 mmol) and 0.6130 g (4.38 mmol) of hexamethylenetetraamine was dissolved in 500 mL of water, and then refluxed for 4 hours to produce the pink product.

The IR spectrum of the α-$Co(OH)_2$ sample showed a peak at approximately 1600 $cm^{-1}$ ($CO_3^{2-}$) and a broad peak centered at 3500 $cm^{-1}$ (hydrogen-bonded OH groups). TGA analysis also showed an extra weight loss of 10 wt%, which would be attributed to the loss of water and other interlayer species. The β form gives only a sharp peak at 3650 $cm^{-1}$, resulting from isolated OH groups of the $Co(OH)_2$ framework.

$Ni_{1/3}Co_{2/3}(OH)_2$ was prepared in a similar way, by dissolving 0.5948 g of $CoCl_2 \cdot 6H_2O$ (2.5 mmol) and 0.2971 g of $NiCl_2 \cdot 6H_2O$ (1.25 mmol), 0.6133 g of hexamethylenetetramine (4.38 mmol) in 500 mL of deoxygenated water and refluxing for 4.5 hours under nitrogen. After the product had settled, it was washed with water and ethanol, and dried at 60˚C. Elemental analysis by ICP-AES determined the Ni:Co ratio to be 1.1:1.9.

### *Preparation of isotropic $NiCo_2O_4$ powder*

The metal ratio was adjusted to $Ni_{1.1}Co_{1.9}O_4$ in order to match the stoichiometry to the $NiCo_2O_4$ platelet sample. 0.6398 g of $Ni(NO_3)_2 \cdot 6H_2O$ (2.2 mmol) and 1.1059 g of

$Co(NO_3)_2 \cdot 6H_2O$ (3.8 mmol) was dissolved in approximately 10 mL of ethanol, which was then concentrated on a rotary evaporator until a thick syrup resulted. This was dried at 120˚C, and then heated in air at 350˚C for 2 hours. Despite the short calcination, XRD showed the synthesis of a crystalline phase-pure spinel product, with TEM analysis showing a particle diameter of approximately 1-2 μm. A portion of this was further heated at 500˚C for 12 hr under flowing oxygen

***Preparation of thin layered precursors for $NiCo_2O_4$ and $CoFe_2O_4$ platelets***

A 100 mL solution containing 0.1190 g of $CoCl_2 \cdot 6H_2O$, 0.0594 g of $NiCl_2 \cdot 6H_2O$, 0.1227 g of hexamethylenetetramine, and 0.1 g of polyvinylpyrrolidone were fully deoxygenated and then quickly sealed in a 120-mL Parr bomb. The solution was heated at 5 °C/min to 150°C, where it was held for 24 hours. The product was washed with water and ethanol, and dried at 60°C. EDS confirmed a Ni-Co ratio of approximately 1:2.

For preparing layered precursors with Co-Fe composition, 0.2974 g of $CoCl_2 \cdot 6H_2O$, 0.3169 g of anhydrous $FeCl_2$, and 0.1 g of polyvinylpyrrolidone (MW = 40,000) were added to 500 mL of fully deoxygenated water. The solution was heated to reflux, during which it remained clear with only a slight brown tinge. To this, 1.0514 g of hexamethylenetetraamine dissolved in a minimal amount of water was added via syringe. A white to grey turbidity is observed, and the reaction was cooled after 4 hours since further heating produced a coarse brown powder suspension. The suspension was collected by centrifugation and washed with water and ethanol, during which the powder oxidized to a brown opalescent suspension. EDS shows an approximate Co:Fe ratio of 1:2.

**Characterization**

X-ray diffraction patterns were recorded using Cu-$K_\alpha$ radiation on a Philips X'pert MPD diffractometer. TEM images were obtained on a JEOL JEM-2010 $LaB_6$

microscope operating at 200kV. Thermal gravimetry and differential scanning calorimetry were conducted on a TA SDT 2960, using approximately 100 ml/min of $O_2$. Nitrogen adsorption measurements were obtained on a Micromeritics ASAP 2010. DC magnetization measurements were performed using a Superconducting Quantum Interference Device (SQUID) magnetometer with temperature range from 1.8K to 370K and with a magnetic field up to 6T. We also performed AC susceptibility measurements with the ACMS option of the Quantum Design PPMS cryostat, at temperatures down to 2K and with a frequency range from 10 Hz to 10K Hz. Specific heat measurements were carried out in a PPMS cryostat with He3 option with temperature down to 0.4K using a standard semiadiabatic heat pulse technique.

## Results and Discussion

### Conversion to metastable $NiCoAlO_4$

Our initial hypothesis was that the layered metal hydroxide method might yield spinels with both metastable cation distributions and compositions. In order to test this idea, a range of the binary and ternary LDHs $Co_2Al$-LDH, FeCoAl-LDH, ZnCoAl-LDH, NiCoAl-LDH, $Ni_2Al$-LDH and structurally similar $Ni_{1/3}Co_{2/3}(OH)_2$, $\alpha$-$Co(OH)_2$, and $\beta$-$Co(OH)_2$ were synthesized as highly crystalline platelets. In general, IR analysis indicated that both nitrate and carbonate anions together with water were intercalated, although no attempts were made to quantify the relative amounts. Elemental analyses were also conducted on select samples to determine relative metal cation ratios, with ratios reasonably close to the nominal amount for NiCoAl-LDH and $Ni_{1/3}Co_{2/3}(OH)_2$. Dehydrating these LDHs in an oxidizing environment (i.e., in oxygen) led to spinels for all cases except $Ni_2Al$-LDH. However, we did not find any unusual cation distributions for cases such as $Co_2AlO_4$ and $ZnCoAlO_4$. Determining cation distributions in other spinel products such containing Ni, Co, and Fe were difficult due to similar atomic scattering factors. As for the LDH precursors, there is some evidence based on EXAFS,

IR, and UV-vis supporting long-range ordering in certain compositions (Cr-containing LDHs,[18-20] aged Mg-Al LDHs[21] and other systems[16]), which may have an interesting effect on the cation distribution of the spinel product. However, XRD typically encounters difficulty in determining this since the superstructure lines can be very weak (for example, the superstructure line for the $Zn_2Cr$-Cl LDH is calculated to be only 0.1% of the maximum reflection), and we could not observe any superstructure reflections in our own XRD patterns.

We did find that the ternary LDH $Ni_{1/3}Co_{1/3}Al_{1/3}(OH)_2 \cdot (CO_3^{2-})_x \cdot (NO_3^-)_y \cdot nH_2O$ decomposes to a metastable spinel ($NiCoAlO_4$) that decomposes above 600˚C. Furthermore, we find that this spinel cannot be prepared by alternate methods of coprecipitation or solid state reaction; it is only accessible from a well crystallized LDH precursor.

Figure 4.2 below shows thermal gravimetric (TGA) and differential scanning calorimetry data (DSC) during the dehydration/oxidation of select layered precursors. Weight loss occurs in two distinct steps, at 200°C and then at 250-300°C; the relative weight loss for $Ni_{1/3}Co_{2/3}(OH)_2$ is less since it does not contain any interlayer water or anionic species. The first step seems to be generally endothermic (as in the case of the Al-containing layered double hydroxides), so may be due to loss of interlayer nitrate, carbonate, and interlayer or lattice water (the apparent endotherm observed close to room temperature is an artifact due to inadequate thermal balancing between the reference and sample thermocouples/sample holders). The higher temperature peak (300 °C) is more ambiguous as to its origins. In general, the brucite-type $Ni_{1/3}Co_{2/3}(OH)_2$ and hydrotalcite-type $Co_{2/3}Al_{1/3}(OH)_2$, $Ni_{1/3}Co_{1/3}Al_{1/3}(OH)_2$ all show slightly different behavior on the DSC plot. Many processes occur during the transformation to a spinel product, such as dehydration/volatilization of nitrate/carbonate (endothermic), oxidation of cobalt (exothermic), crystallization (exothermic), and this renders the DSC plots difficult to interpret. In any event, though, there appear to be two steps, and in terms of mass transfer the transformation is complete by about 400 °C.

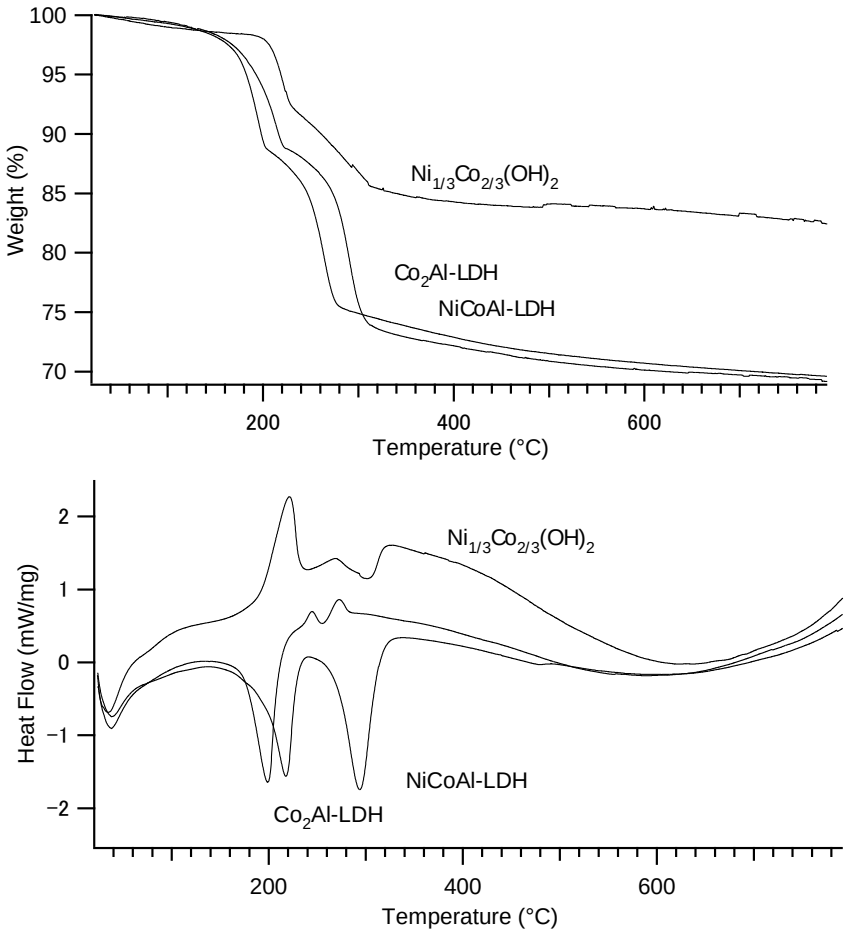


Figure 4.2: Thermal gravimetry (top) and differential scanning calorimetry (bottom; positive flow indicates exotherm) of layered precursors as they transform to spinel products. Heated at 10°C/min, $O_2$.

Figure 4.3 shows the TEM images of the LDH platelets and their SAED patterns, showing the transition from the rhombohedral/hexagonal LDH to a face-centered cubic spinel platelet. Although there appear to be two overlapping LDH platelets in Figure 4.3a, the corresponding SAED pattern shows that they are probably two fused crystallites oriented epitaxially. The pattern shown is characteristic of the [001] zone axis in hexagonal coordinates, and $d_{110}$ obtained from the pattern is approximately 1.50Å. Heating the platelets to 250˚C under flowing oxygen atmosphere leads to no apparent change (Figure 2b), although maintaining this temperature for 12 hours gave a mixture of spinel ([111] zone axis) and LDH [001] spots (not shown). Further heating to 500˚C gave

only spinel spots, where $d_{440}$ = 1.45Å, corresponding to a cubic lattice parameter of $a$ = 8.20Å. In general, TEM images of platelets viewed along their edges show that they are approximately 20 nm thick.

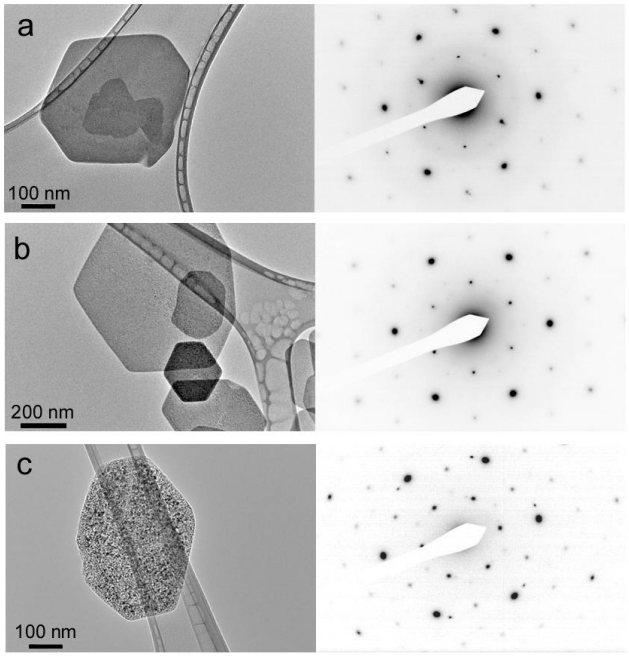


Figure 4.3: TEM images and diffraction patterns of (a) NiCoAl-LDH, (b) product after treatment at 250˚C, 15min., (c) at 500˚C, 12 hr.

The series of X-ray diffraction patterns in Figure 4.4 show the same transition. The top pattern of the LDH precursor shows that the platelets are highly crystalline. The strong intensities of the 012, 015, 018, and 1 0 10 reflections imply that the individual layers are well ordered to form the $3R_1$ polytype.[22] Using hexagonal indices, the lattice parameters for this LDH are $a$ = 3.045Å, $c$ = 22.6 Å, and the (rhombohedral) space group is $R\bar{3}m$. The hexagonal $a$ parameter implies a $d_{110}$ of 1.52 Å, which is reasonably close to that observed by TEM (1.50 Å). When this compound is heated to 250˚C, the XRD pattern (Figure 4.4b) shows that the LDH structure is already lost and the spinel structure has started to form; this is slightly different from the description given by the electron diffraction, which indicates that the structure at this stage is still that of the LDH precursor. Further heating to 400˚C or 500˚C shows spinel formation according to XRD,

as the electron diffraction patterns also show. However, heating the sample to 800˚C shows a clear decomposition to produce a new phase with Ni-O type structure and a similar cubic lattice parameter coexisting with a spinel phase. Given the thermodynamic stability of NiO in the rocksalt structure and the tendency of $NiCo_2O_4$ to decompose at high temperatures, it is not surprising that NiO or $(Ni_xCo_{1-x})O$ might segregate. If this is the case, the remaining spinel phase should be close to a $Co_2AlO_4$ or $CoAl_2O_4$ type spinel. TEM images of $NiCoAlO_4$ after decomposition at 800˚C (see Figure 4.5) show a heterogeneous mixture of numerous platelets, cubes and spherical particles a few hundred nanometers in width. SAED patterns show that the cubes/spheres have a cubic structure, and EDS shows them to contain chiefly Ni and Co. Electron diffraction of particles indexes well to a cubic structure ([112] zone axis). The lattice parameter of this particle was approximately 8.3 Å, indicative of a spinel—unfortunately, in the TEM we could not find the NiO-type phase suggested by XRD. Larger, fairly amorphous aggregations of plates were also observed, and EDS indicated that they contained primarily Al. While the decomposition products suggested by TEM and XRD are different, this type of difference was seen earlier in the structure at 250 ˚C; in both cases we see decomposition to a multiphase mixture.

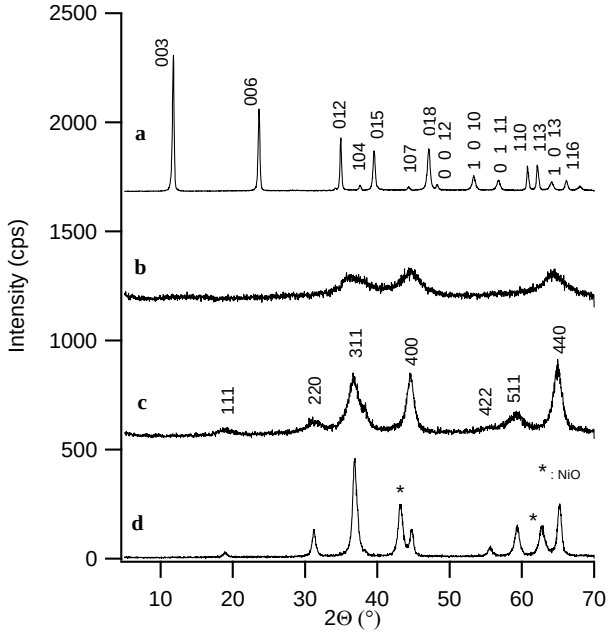


Figure 4.4: XRD patterns of (a) NiCoAl-LDH, (b) product after treatment at 250˚C, 15min., (c) at 500˚C, 12 hr., and (d) at 800˚C, 12hr.

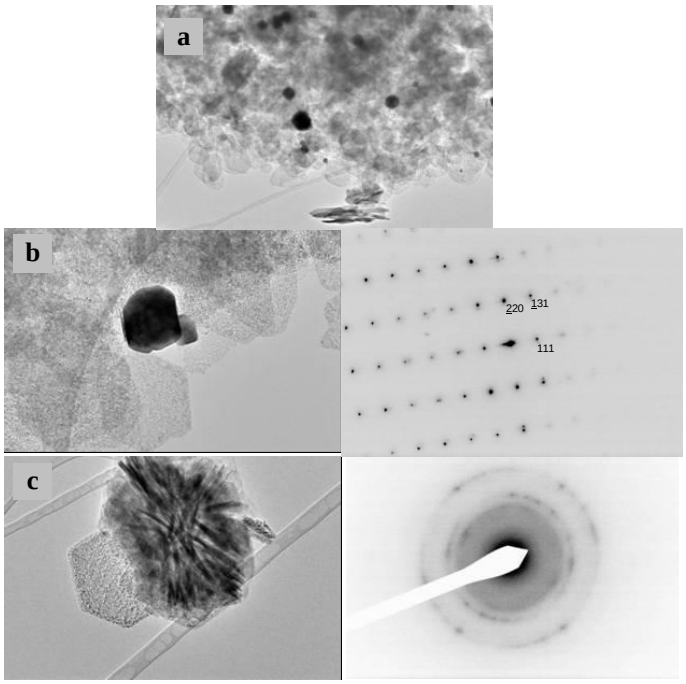


Figure 4.5: Decomposition products of NiCoAlO4 at 800˚C.

**Roughness and mosaic structure of $NiCoAlO_4$ platelets**

High resolution imaging of the spinel platelets shows lattice fringes running over tens to hundreds of nanometers, as seen in Figure 4.6 . The top picture in Figure 4.6 is a view looking at the edge of a $NiCoAlO_4$ platelet, whereas the bottom picture is a view of the face of the platelet. Lattice fringes can be seen running long distances (beyond the field of view in the shown image), despite the porous, rough surface induced during transformation to the spinel. The rough surface induces a high surface area--conversion from the LDH precursor to the spinel product increased the BET surface area from 20 $m^2/g$ to 120 $m^2/g$. Assuming a density of 5.2 $g/cm^3$, a solid spinel platelet 20 nm thick and 1 $\mu m^2$ in area would be expected to have a surface of only 20 $m^2/g$, close to that of the precursor.

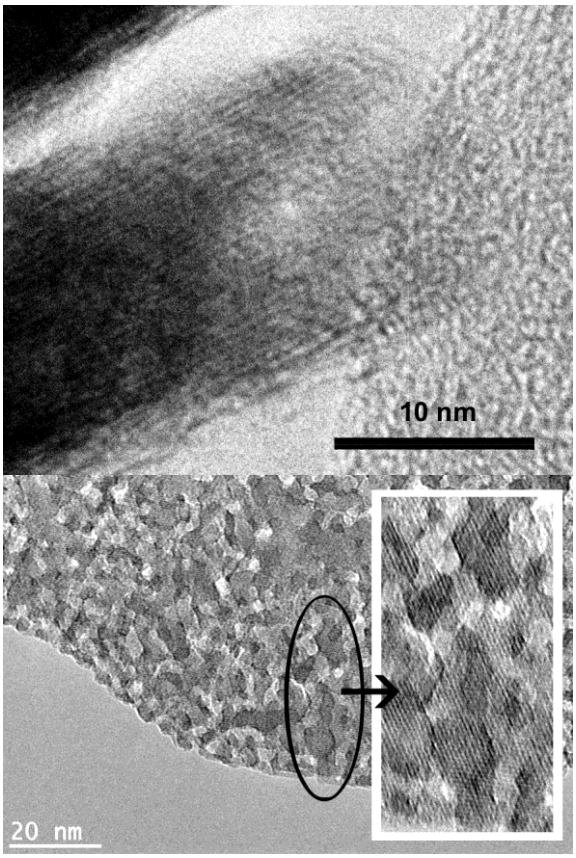


Figure 4.6: High resolution TEM images of a $NiCoAlO_4$ platelet formed at 500˚C

Each spinel product exhibits a single set of electron diffraction spots and long lattice fringes, consistent with a single crystal platelet. However, close examination of the diffraction spots implies that the platelets possess a mosaic structure, with small crystallites slightly misaligned with respect to each other. Figure 4.7 shows magnified view of diffraction spots from the (a) LDH and (b) spinel product, respectively. While the diffraction spot for the LDH precursor is circular, the spots from the spinel product are elongated along a constant d-spacing (i.e., along concentric arcs). Profiling the spots as shown in the lower portion of Figure 4.7 show the different peak widths, and this difference was observed for numerous spots in multiple spinel platelets. It is highly possible that the apparent mosaic structure is related to the porous, rough surface of the platelet.

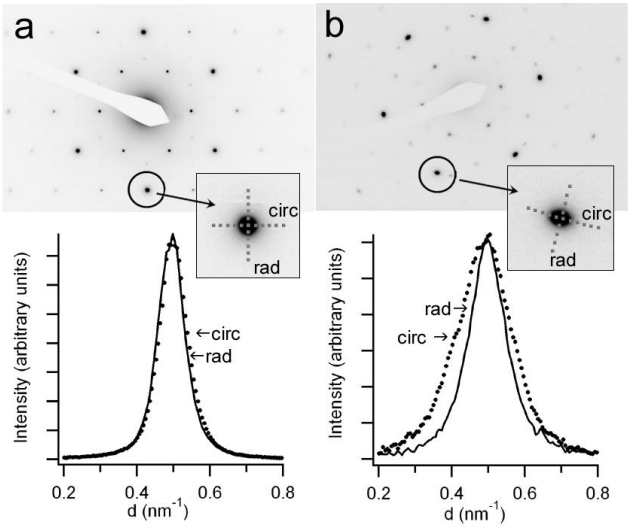


Figure 4.7: Profiles of diffraction spots from a NiCoAl-LDH platelet (a) and $NiCoAlO_4$ spinel platelet (b).

The acute observer will also find that the electron diffraction patterns of the (111) zone of $NiCoAlO_4$ prepared at 500˚C show sharp spots, whereas all the peaks in the corresponding X-ray diffraction pattern are quite broad. For example, the platelets are about 500 nm - 1 μm wide and the SAED pattern (always recorded with the selective area

aperture covering at least 50% of a platelet) shows only a single set of sharp spots, as in the {440} spots (the six darkest spots in Figure 4.3b). However, in the X-ray pattern (as in Figure 4.4c) the 440 reflection at 65˚ implies a crystallite size of only 9nm. The mosaic structure suggested by the elongated diffraction spots is one factor that contributes to peak broadening in the X-ray diffraction pattern. However, the primary reason for the broad X-ray peaks is that XRD and SAED are probing crystallinity in different directions; that is, SAED probes in-plane crystallinity only, whereas X-ray peak widths include symmetry-equivalent cross-plane reflections. Because of the high symmetry of the cubic spinel system, there are many planes of the {440} family; some of these are perpendicular to the platelet face and therefore reflect the long-range in-plane crystallinity. Many others lie at oblique angles with respect to the platelet face. Only the {440} planes perpendicular to the platelet contribute to electron diffraction, where as all {440} planes contribute to the X-ray diffraction pattern. In the X-ray pattern the broad peaks from oblique {440} planes are superimposed on a smaller component of sharp {440} peaks, resulting in an overall broad peak shape.

Although the XRD in Figure 4.4c shows that for the $NiCoAlO_4$ platelets there is no NiO impurity in comparable amount or crystallinity, in general we do recognize that the elemental homogeneity of the platelets is still somewhat open to question. An attempt was made to acquire element-specific high resolution TEM images using an energy filter. However, interpretation proved to be difficult given the weak signal and the heterogeneous contrast caused by surface roughness.

**Attempted alternate routes to $NiCoAlO_4$**

$NiCo_2O_4$ is a spinel related to $NiCoAlO_4$ which is also known to decompose to NiO and a Ni-deficient spinel above usually 400-500˚.[23, 24] However, $NiCo_2O_4$ is quite accessible by conventional methods such as heating nitrate salts to 350˚C or coprecipitating amorphous metal hydroxides and then calcining them at similar temperatures. To test if the ternary $NiCoAlO_4$ spinel could be made by other methods, we tried three different procedures: 1) direct solid state synthesis from nitrate salts, 2) the

citrate gel method, and 3) from an amorphous hydroxide precipitate of the metal salts. The first two methods produced a mixture of a NiO and spinel type phase, as shown in the XRD patterns in Figure 4.8ab. The hydroxide precipitate did form a spinel phase without any noticeable NiO-type phases (Figure 4.8c), but the TEM image Figure 4.8e shows that the crystallites are extremely small and aggregate to form larger particles. These control experiments show that the layered precursor method is the only way thus far to prepare highly crystalline samples of $NiCoAlO_4$; it may be the ternary nature of this system that makes it more difficult to prepare phase-pure than $NiCo_2O_4$.

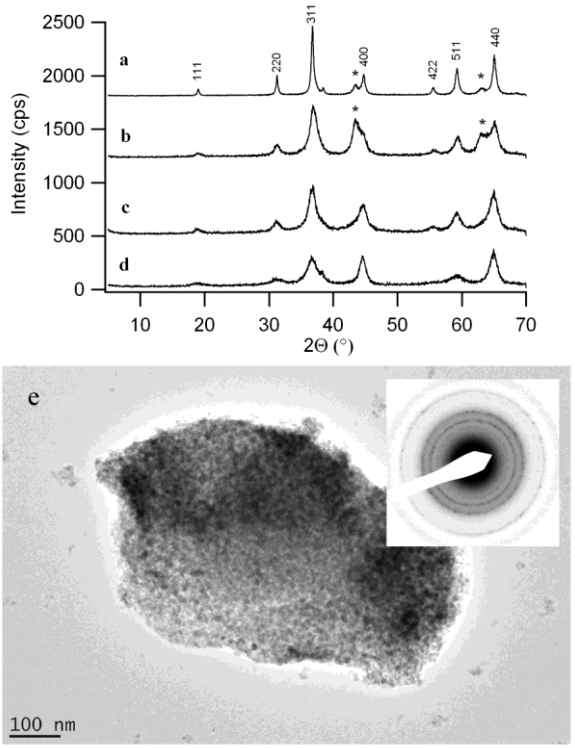


Figure 4.8: XRD patterns and TEM images of attempted $NiCoAlO_4$ synthesis from various methods. (a) solid state reaction of nitrate salts, (b) citrate gel method, (c) amorphous metal hydroxides, (d) crystalline LDH precursor, and (e) TEM image of product from (c).

When examining different spinel products, we found that the $\alpha$-$Co(OH)_2$ precursor gave lacey spinel platelets that were still reminiscent of the original hexagonal plate morphology (Figure 4.9). What is surprising is that despite the excessive

deformation, each platelet still remains a single crystal. The $Co_3O_4$ spinel platelets formed from the β precursor are also single crystalline, but have some cracks, as opposed to the lacey structure. Dehydrating both precursors at a slower rate of 1 C˚/min (compared to the 10C˚/min used in other experiments) did not result in any changes in the final morphology.

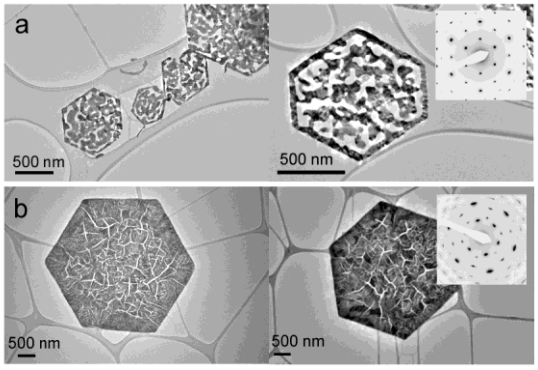


Figure 4.9: TEM images and diffraction patterns of $Co_3O_4$ platelets formed from (a) α-$Co(OH)_2$ and (b) β-$Co(OH)_2$.

It is likely that this lacey platelet is an extreme case of the surface roughness induced in the $NiCoAlO_4$ case. Despite the transformation to spinel being nominally topochemical, a slight decrease in the in-plane lattice parameter is necessary during transformation to spinel, and this is probably the cause of roughness or, in the case of $Co_3O_4$, extreme porosity. When one compares the LDH and spinel (111) layers closely; the spinel (111) layers have a higher metal cation density per unit area. Figure 4.1cd illustrate that the spinel (111) layers are composed of two alternating sublayers; one is the purely octahedral (gray) layer and the other is the layer composed of both grey octahedra and peach-colored tetrahedra. As mentioned earlier and shown in Figure 4.1c, one can imagine how metal ions in select octahedra in the precursor move to form the octahedral/tetrahedral sublayer. However, when one counts the cation holes in the octahedral layer and compares it to the cations per area of the octahedral/tetrahedral layer, there are two extra cations per unit area in the latter. To form a large crystallite of the ideal spinel structure would require long range diffusion of metal atoms to provide these extra cations, accompanied by shrinkage of the crystallite in the in-plane direction.

An alternate view of the transformation is that two neighboring LDH sheets (as opposed to a single sheet) form a pair of the octahedral and octahedral/tetrahedral layers; however, the total number of cations per unit area during the transformation is again not conserved.

**Magnetic properties of platelets of $NiCoAlO_4$ and $NiCo_2O_4$**

Since small particles of ferrimagnetic materials can exhibit superparamagnetism, an interesting question is whether these thin platelets are superparamagnetic or ferrimagnetic. While their thickness is within range of room temperature superparamagnetism, their lateral dimensions are very large. To date there have been some studies of shape control of superparamagnetic particles, but most of these focus on cubes or spheres.[14] To examine the effect of the platelet morphology on magnetism, a comparison was made between $NiCo_2O_4$ in platelet form and bulk powder form. $NiCo_2O_4$ is a known ferrimagnet ($T_c$ ranging 350K-670K[23, 25-28]) with an extrapolated 0K saturation magnetization of 1.25-1.5 $\mu_B$ per formula unit, depending on the synthetic route.[23, 24, 27, 29] Previously, Markov *et al* and Klissurski *et al* have prepared $NiCo_2O_4$ from layered precursors, but they did not examine the morphology or magnetic properties of their spinel products.[6, 30]

To serve as a control for the platelet morphology, isotropic (1-2 μm diameter) particles of $NiCo_2O_4$ were prepared at 350˚C and 500˚C. In preparation, the stoichiometry of these samples was adjusted so that the Ni:Co ratio matches the true ratio of the platelet sample, which was 1.1:1.9 rather than 1:2. Although these bulk $NiCo_2O_4$ samples partially decompose at 500˚C to produce a small amount of NiO impurity, magnetic measurements were conducted on samples prepared at both temperatures since the platelets could be made at 500˚C without any NiO impurity (see XRD in Figure 4.10). the magnetic measurements, in Figure 4.11, shows that both bulk $NiCo_2O_4$ samples have similar magnetic behavior, consistent with ferrimagnetism below its Curie temperature and a saturation magnetic moment of 1.5 $\mu_B$ (2 K)

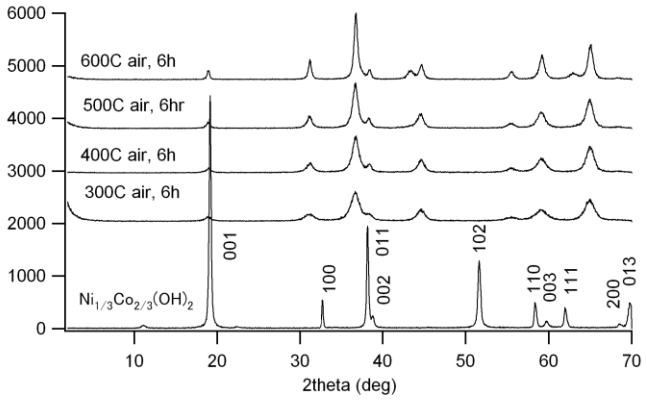


Figure 4.10: XRD patterns showing the formation of $NiCo_2O_4$ platelets.

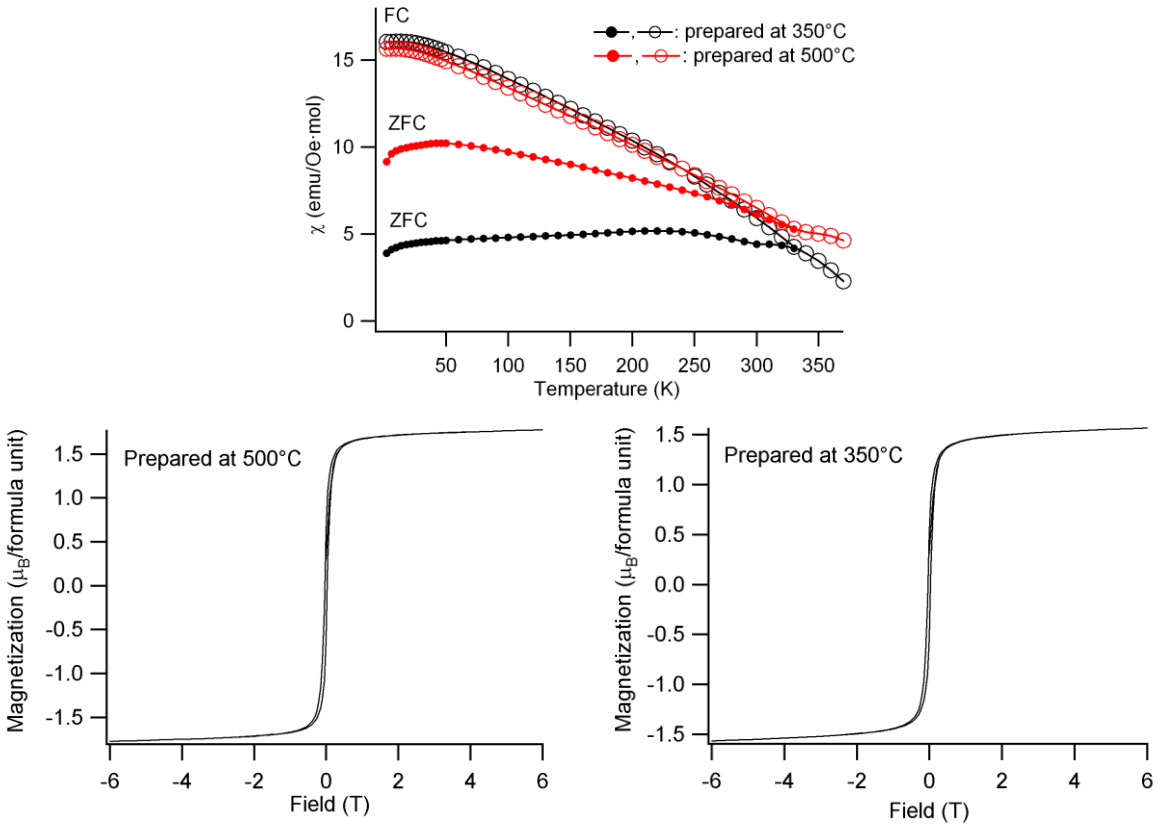


Figure 4.11: Magnetization curves of $NiCo_2O_4$ powder prepared at 350˚C and 500˚C (saturation curves obtained at 2K).

In contrast, $NiCo_2O_4$ in platelet form (approximately 1 μm lateral dimensions and 50 nm thick) showed superparamagnetism with a blocking temperature $T_B$ of approximately 250 K, as shown in Figure 4.12a —the zero field-cooled lines and field cooled lines match well above $T_B$. Hysteresis curves above and below $T_B$ show the absence and presence of hysteresis, respectively. The saturation magnetization at 2 K is approximately 1.3 $\mu_B$, close to that of isotropic powdered $NiCo_2O_4$. AC susceptibility measurements in Figure 4.12 show the increase of $T_B$ as the frequency of the applied field increases, which is another indication of superparamagnetism.

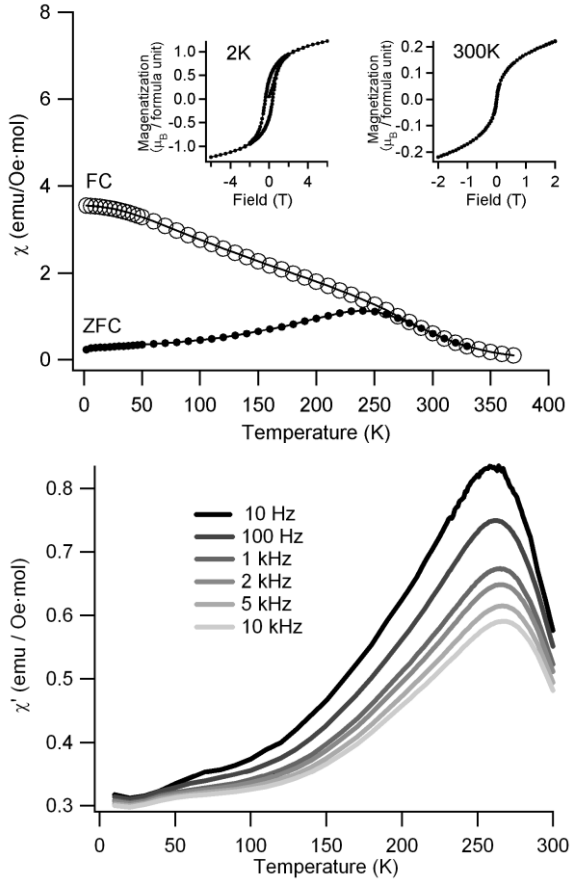


Figure 4.12: (a) DC magnetization data on $NiCo_2O_4$ platelets and (b) AC magnetic susceptibility data on the same sample

Similar measurements were also done on the metastable $NiCoAlO_4$ platelets (Figure 4.13). They showed similar superparamagnetic behavior, with a lower blocking

temperature (30~40 K) probably because the platelets were thinner (20 nm). In the field cooled curve for Figure 4.12 the increase in susceptibility at low temperatures is somewhat suppressed, and a similar trend can be seen in Figure 4.13 also. This may be attributed to domain-domain interactions within the platelet, and to a lesser extent between separate platelets; however, we believe that in our case this interaction does not lead to spin glass formation as other authors have found.[31, 32] The temperature dependence of the heat capacity of the $NiCoAlO_4$ platelets was measured (Figure 4.14) and no change in sign of the slope was observed near 40K. The fact that no change was observed excludes the possibility of the 40K event being a spin glass or ferrimagnetic transition. This result, combined with the AC susceptibility data, supports our conclusion that the peak in the zero field cooled peak at 40K is indeed at blocking temperature.

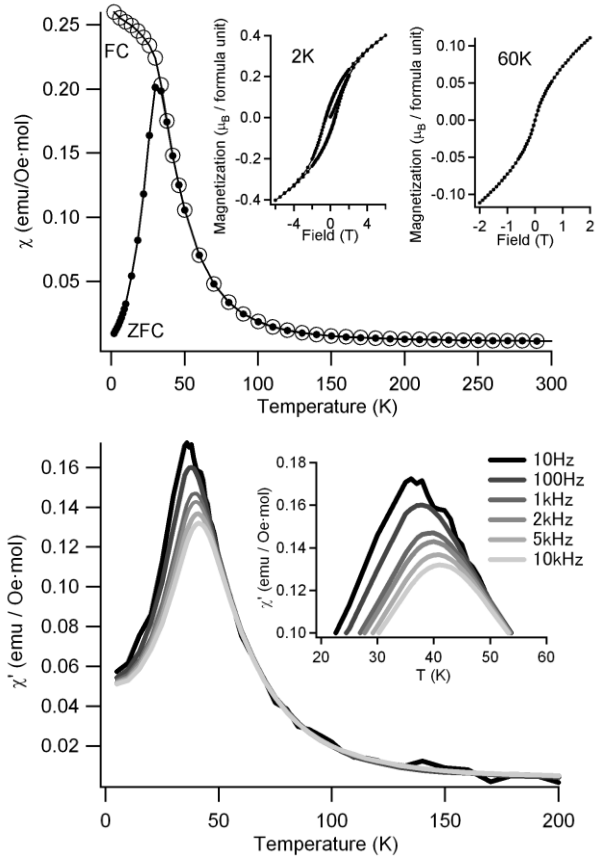


Figure 4.13: (a) DC magnetization data on $NiCoAlO_4$ platelets and (b) AC magnetic susceptibility data on the same sample.

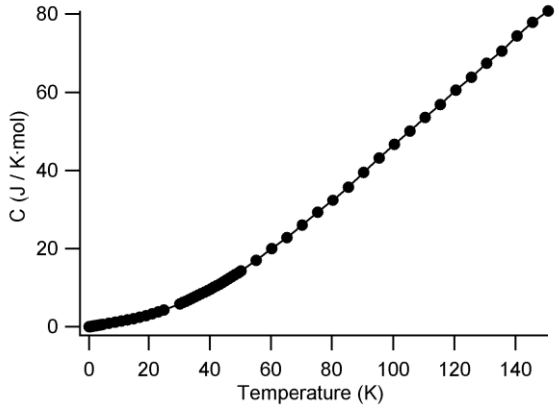


Figure 4.14: Low-temperature heat capacity of $NiCoAlO_4$ platelets.

The blocking temperatures of these two compositions of spinel platelets are quite different, and in general are very low considering the large volume of the platelets. Although originally derived for isolated, non-interacting particles, we turn to Stoner-Wohlfarth theory,[33, 34] the blocking temperature of a superparamagnet is related to the particle size and intrinsic anisotropy constant by the following expression (Equation 4.1):

$$E_A = KV \sin^2 \theta \qquad 4.1$$

where $K$ is the anisotropy constant, $V$ is the volume of the superparamagnetic domain, and $\theta$ is the angle between the magnetization axis and easy axis of magnetization. The blocking temperature $T_B$ is such that the product $k_b T_B$ ($k_b$ = Boltzmann constant) is equal to the right hand side of the expression when $\theta = 0$. Assuming that the $NiCo_2O_4$ platelet has a lateral area of 1 $\mu m^2$ and thickness of 50 nm, a $T_B$ of 250K implies an anisotropy constant $K$ of only 0.7 erg/$cm^3$, which is perhaps 2~5 orders of magnitude smaller than what might be expected for a cobalt-containing spinel[14, 35, 36] such as $NiCo_2O_4$. On the other hand, if the superparamagnetic domain size is a cube that is only 50 nm tall (as thick as the platelet), then the anisotropy constant would be 270 erg/$cm^3$, which is a more reasonable value. Similarly, for the $NiCoAlO_4$ platelets, the low blocking temperature (40K) implies that the superparamagnetic domain is even smaller, having a volume of 200~1000 $nm^3$ (anisotropy values of 700~45000 erg/$cm^3$). Thus,

within the framework of Stoner-Wohlfarth theory, it is more reasonable to describe each platelet as having many small superparamagnetic domains despite the apparent single crystalline nature. The porous or rough structure of the $NiCoAlO_4$ platelet shown in Figure 4.6 shows surface protrusions that are on the order of 5-10 nm, and this or the mosaic structure may be the origin of the multiple domains. An alternate explanation would be that the large anisotropy supplies an additional easy axis of magnetization contained within the (111) plane. The causes the $\sin^2\theta$ term in Equation 4.1 to become smaller than 1, since the angle between the magnetization axis and easy axis is now always less than 90˚; this results in a lower blocking temperature. Hou *et al* prepared single crystal $Co_3O_4$ platelets approximately 20nm thick and 200 nm in diameter, and reported a blocking temperature of approximately 35 K, however, they did not comment on whether this would be expected for the given dimensions and anisotropy constant.[37]

**Preparation of $CoFe_2O_4$ platelet precursors and control of platelet thickness**

While any ferrimagnetic materials can be prepared as superparamagnetic particles, much research to date has focused on $CoFe_2O_4$ nanoparticles, given its high magnetization. Hence, when preparing these spinel platelets it would be beneficial to be able to prepare the same $CoFe_2O_4$ composition. However, simply precipitating a $NiCl_2$-$FeCl_2$ solution via hexamethylenetetraamine (HMT) hydrolysis fails to produce platelets of desirable quality, as seen in Figure Figure 4.15a. Some of the platelets are in fibrous rather than solid, and EDS shows that their elemental ratios are not Co:Fe = 1:2. In fact, it was observed that the supernatant after precipitation changed to a brown color upon exposure to air, indicating that not all Fe species had precipitated. Despite the entire reaction being conducted under nitrogen, the color of this reaction mixture turned dark brown by the time refluxing temperatures were achieved, so it is possible that the some of the iron salts oxidize in the alkali environment at high temperature before they may co-precipitate (Ma *et al* report their $Co_2Fe(OH)_2$ sample to be a light pink,[38] so we expect our $CoFe_2(OH)_2$ sample to be a pale color also). Hence, to test this, another run was

conducted where a solution containing the cobalt and iron salts was first heated to reflux, and then a concentrated HMT solution was added via syringe. The solution remained clear and largely colorless until HMT was added; within seconds of HMT addition the color of the solution turned brown and opaque as the salts precipitated, but the color was not as dark as before. TEM (Figure 4.15b) shows more solid platelets have formed; however, among them some have thicknesses of approximately 100 nm (see inset). This inhomogeneity in thickness was remedied by the addition of a coordinating polymer, polyvinylpyrrolidone to the reaction mixture prior to heating; the platelets in Figure 4.15c generally tended to be thinner and more homogeneous in thickness. A relatively short reflux time (4 hrs) prevented the white suspension from turning to a coarse brown powder. The consistent solid platelet morphology may be an effect of the polymer selectively binding on the faces of the crystallites, and regulating the balance between lateral and axial growth, and smooth precipitation to a crystalline product also may be preventing the Fe species from oxidizing easily.

A similar influence on thickness by PVP was also observed in preparing $NiCo_2O_4$ platelets. As briefly mentioned earlier in this chapter, the $NiCo_2O_4$ platelets were typically approximately 50 nm thick (Figure 4.15d), somewhat thicker than the $NiCoAlO_4$ platelets. Addition of PVP to the reaction mixture before heating resulted in much thinner platelets (Figure 4.15e). In fact, images at higher magnifications showed that the platelets tended to look more like fragile sheets, with many cracks and tears. Raising the reaction temperature to hydrothermal conditions and increasing the reaction time (150 °C, 24 hrs) produced more solid platelets, which still appear to be thinner than the initial sample without PVP.

In summary, we find that by controlling the timing of HMT addition and the use of coordinating polymers such as PVP, we may control the growth of these layered precursors. The preparation of thin $CoFe_2O_4$ and $NiCo_2O_4$ platelets will make future studies on ferrofluids much easier as they should be easier to disperse in solution.

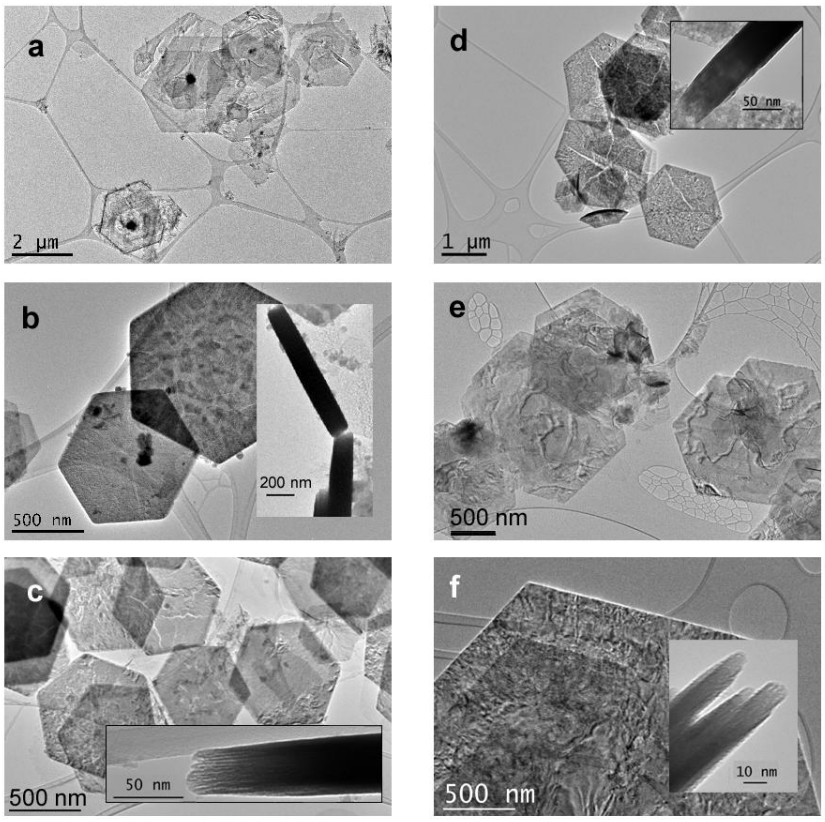


Figure 4.15: Morphology of various Ni-$Co_2$ and Co-$Fe_2$ hydroxide platelets influenced by the addition of polyvinylpyrrlidone. (a-c) show Co-$Fe_2$ platelets, (d-f) show Ni-$Co_2$ platelets.

a) HMT added before reflux, no PVP
b) HMT added during reflux, no PVP
c) HMT added during reflux, with PVP
d) HMT added before redlux, no PVP
e) HMt added during reflux, with PVP
f) HMT added with PVP at room temperature, reaction at 150 ℃

## Conclusions

Studying the transformation of well-defined single crystalline layered precursors to spinels enables us to examine in detail the topochemical nature of the transformation. The spinel platelets are highly crystalline in their lateral directions, and the layered precursor method has been demonstrated to be a valuable route in preparing large, highly anisotropic superparamagnetic particles of variable composition including the metastable $NiCoAlO_4$. Assuming that the Stoner-Wohlfarth equation still holds for highly anisotropic particles, the surprisingly low blocking temperature of the micron-sized $NiCoAlO_4$ platelets can be explained by the presence of multiple domains induced by roughness and a mosaic structure; otherwise, the considerable shape anisotropy of the particles may be a factor.

Future challenges are to disperse these relatively large particles as a stable, preferably concentrated ferrofluid. If individual platelets show a preference to stacking face-to-face or edge-to-edge under a magnetic field, the fluid may show interesting rheology. Light transmission studies on a magnetically responsive liquid crystal are also an attractive idea, but the high optical absorption of the spinel particles will have to be addressed.

In terms of preparing thin films of these spinels, using simple wet chemical methods, LDH particles have previously been tiled on solid substrates with fairly high packing density.[39, 40] By applying their technique, oriented films of these spinels should be easily prepared on a substrate, and this may serve as a useful platform for other applications or magnetic measurements such as investigating the easy axis of orientation or anisotropic susceptibilities.

## References


1. Sun, G.; Sun, L.; Wen, H.; Jia, Z.; Huang, K.; Hu, C. *J. Phys. Chem. B* **2006,** *110*, 13375-13380.

2. Zou, L.; Li, F.; Xiang, X.; Evans, D. G.; Duan, X. *Chem. Mater.* **2006,** *18*, 5852-5859.

3. Ruano-Casero, R. J.; Perez-Bernal, M. E.; Rives, V. *Z. Anorg. Allg. Chem.* **2005,** *631*, 2142-2150.

4. Kannan, S.; Venkov, T.; Hadjiivanov, K.; Knözinger, H. *Langmuir* **2004,** *20*, 730-736.

5. Meng, W.; Li, F.; Evans, D. G.; Duan, X. *Mater. Chem. Phys.* **2004,** *86*, 1-4.

6. Markov, L.; Petrov, K. *Reac. Solids* **1986,** *1*, 319-327.

7. Liu, J.; Li, F.; Evans, D. G.; Duan, X. *Chem. Commun.* **2003**, 542-543.

8. Li, F.; Liu, J.; Evans, D. G.; Duan, X. *Chem. Mater.* **2004,** *16*, 1597-1602.

9. Rojas, R. M.; Kovacheva, D.; Petrov, K. *Chem. Mater.* **1999,** *11*, 3263-3267.

10. Markov, L.; Petrov, K.; Lyubchova, A. *Solid State Ionics* **1990,** *39*, 187-193.

11. Liu, Z.; Renzhi, M.; Osada, M.; Takada, K.; Sasaki, T. *J. Am. Chem. Soc.* **2005,** *127*, 13869-13874.

12. Ma, R.; Liu, Z.; Takada, K.; Iyi, N.; Bando, Y.; Sasaki, T. *J. Am. Chem. Soc.* **2007,** *129*, 5257-5263.

13. Liu, Z.; Ma, R.; Ebina, Y.; Iyi, N.; Takada, K.; Sasaki, T. *Langmuir* **2007,** *23*, 861-867.

14. Song, Q.; Zhang, Z. J. *J. Am. Chem. Soc.* **2004,** *126*, 6164-6168.

15. Lüders, U.; Barthélémy, A.; Bibes, M.; Bouzehouane, K.; Fusil, S.; Jacquet, E.; Contour, J.-P.; Bobo, J.-F.; Fontcuberta, J.; Fert, A. *Adv. Mater. (Weinheim, Fed. Repub. Ger.)* **2006,** *18*, 1733-1736.

16. Bellotto, M.; Rebours, B.; Clause, O.; Lynch, J.; Bazin, D.; Elkaim, E. *J. Phys. Chem.* **1996,** *100*, 8527-8534.

17. Ma, R.; Liu, Z.; Takada, K.; Fukuda, K.; Ebina, Y.; Bando, Y.; Sasaki, T. *Inorg. Chem.* **2006,** *45*, 3964-3969.

18. Roussel, H.; Briois, V.; Elkaim, E.; de Roy, A.; Besse, J. P. *J. Phys. Chem. B* **2000,** *104*, 5915-5923.

19. Roussel, H.; Briois, V.; Elkaim, E.; de Roy, A.; Besse, J. P.; Jolivet, J. P. *Chem. Mater.* **2001,** *13*, 329-337.

20. Boclair, J. W.; Braterman, P. S.; Jiang, J.; Lou, S.; Yarberry, F. *Chem. Mater.* **1999,** *11*, 303-307.

21. Richardson, M. C.; Braterman, P. S. *J. Phys. Chem. C* **2007,** *111*, 4209-4215.

22. Radha, A. V.; Shivakumara, C.; Vishnu Kamath, P. *Clays and Clay Minerals* **2005,** *53*, 520-527.

23. Battle, P. D.; Cheetham, A. K.; Goodenough, J. B. *Mater. Res. Bull.* **1979,** *14*, 1013-1024.

24. Marco, J. F.; Gancedo, J. R.; Gracia, M.; Gautier, J. L.; Ríos, E. I.; Palmer, H.; Greaves, C.; Berry, F. J. *J. Mater. Chem.* **2001,** *11*, 3087-3093.

25. Holgersson, S.; Karlsson, A. *Z. Anorg. Allg. Chem.* **1929,** *183*, 383-394.

26. Blasse, G. *Philips Res. Rept.* **1963,** *18*, 383-392.

27. Lenglet, M.; Guillamet, R.; Durr, J.; Gryffroy, D.; Vandenberghe, R. E. *Solid State Commun.* **1990,** *74*, 1035-1039.

28. Knop, O.; Reid, K. I. G.; Sutarno, Y.; Nakamura, Y. *Can. J. Chem.* **1968,** *46*, 3463-3476.

29. Marco, J. F.; Gancedo, J. R.; Gracia, M.; Gautier, J. L.; Rios, E.; Berry, F. J. *J. Solid State Chem.* **2000,** *153*, 74-81.

30. Klissurski, D. G.; Uzunova, E. L. *Chem. Mater.* **1991,** *3*, 1060-1063.

31. Mørup, S.; Bødker, F.; Hendriksen, P. V.; Linderoth, S. *Phys. Rev. B: Condens. Matter* **1995,** *52*, 287-294.

32. Prené, P.; Tronc, E.; Jolivet, J.-P.; Livage, J. *IEEE Trans. Magn.* **1993,** *29*, 2658-2660.

33. Stoner, E. C.; Wohlfarth, E. P. *IEEE Trans. Magn.* **1991,** *27*, 3475-3518.

34. Stoner, E. C.; Wohlfarth, E. P. *Trans. R. Soc.* **1948,** *A240*, 599-644.

35. Calero-DdelC, V. L.; Rinaldi, C. *J. Magn. Magn. Mater.* **2007,** *314*, 60-67.

36. Zhang, H. Y.; Gu, B. X.; Zhai, H. R.; Lu, M.; Miao, Y. Z.; Zhang, S. Y.; Huang, H. B. *J. Appl. Phys.* **1994,** *75*, 7099-101.

37. Hou, Y.; Kondoh, H.; Shimojo, M.; Kogure, T.; Ohta, T. *J. Phys. Chem. B* **2005,** *109*, 19094-19098.

38. Ma, R.; Liu, Z.; Takada, K.; Iyi, N.; Bando, Y.; Sasaki, T. *J. Am. Chem. Soc.* **2007,** *129*, 5257-5263.

39. Lee, J. H.; Rhee, S. W.; Jung, D.-Y. *Chem. Mater.* **2006,** *18*, 4740-4746.

40. Lee, J. H.; Rhee, S. W.; Jung, D.-Y. *J. Am. Chem. Soc.* **2007,** *129*, 3522-3523.

# Chapter 5

## Synthesis of $RbLaNb_2O_6F$, a Mixed Valence Layered Perovskite

## Introduction

Layered perovskites have many interesting physical properties, such as superconductivity[1, 2] or colossal magnetic resistance.[3, 4] However, these layered perovskites are not ion-exchangeable, and it is the ion-exchangeable layered perovskites which are useful building blocks for inorganic materials since they possess a wide range of intercalation and exfoliation chemistry. One common aspect of them, though, is that they usually consist of $d^0$ early transition metal B-site cations (such as $Ti^{4+}$, $Nb^{5+}$, $Ta^{5+}$). Thus, the compounds are typically white insulators and typically have wide band gaps (3-4 eV), and do not possess interesting electronic or magnetic properties themselves. Some exceptions are perovskites doped with rare earths to induce photoluminescence,[5, 6] transition metal ions such as Mn to impart magnetism,[7] or treatment with ammonia to yield narrow band gap oxynitrides.[8] Here, we explore the reductive fluorination of ion-exchangeable Dion-Jacobson and Ruddlesden-Popper layered perovskites to obtain mixed-valence layered perovskites which, potentially could be exfoliated into single layer sheets. Electronic structure calculations in this study and the literature show that these materials can be made 2D metals if an extra electron is injected into the conduction band via reduction.[9, 10] If the mixed valences are reasonably stable in air, such a finding would provide an interesting parallel to graphene sheets, and provide a whole new class of oxide conducting nanosheets.

Reduced perovskites with mixed valence and ion-exchange capability exist; however, these have been typically obtained by reduction and insertion of an alkali metal into the interlayer, as in $(Li_xVO)La_2Ti_3O_{10}$,[11] $Na_{2-x+y}Ca_{x/2}La_2Ti_3O_{10}$,[12] $Na_{1-x+y}Ca_{x/2}LaTiO_4$,[13] $(Li_xCl)LaNb_2O_7$,[14] $Rb_2LaNb_2O_7$,[15] and other layered tantalates.[16] These materials are at least moderately air sensitive. Furthermore, as the mixed valencies

are induced by changes in the interlayer species, ion exchange or exfoliation may permit the sheets to easily reoxidize and lose their interesting electronic properties.

Instead of modifying the interlayer, reduction by chemically doping the octahedral lattice of the layer slabs themselves provides a more promising route to obtaining stable, reduced oxide nanosheets. The dopant we choose is fluorine, which may exchange with a lattice oxygen in the presence of a separate reducing agent. In this chapter, the preparation and characterization of the air-stable mixed valence oxyfluoride $RbLaNb_2O_6F$ is reported together with encouraging results concerning its ion exchange capability and the synthesis of the analogues $KCa_2Nb_3O_9F$ and $NaYTiO_3F$.

In preparing these layered oxyfluoride perovskites, the precursors chosen were known layered perovskites which are known to already easily exfoliate into nanosheets, such as the n = 2 Dion-Jacobson phase $RbLaNb_2O_7$ and n = 3 phase $KCa_2Nb_3O_{10}$. The structures of these compounds are shown in Figure 5.1. The main difference is the number of $MO_6$ octahedra (hence n = 2, n = 3) forming each layer slab. It is typical of the $MO_6$ octahedra to be slightly distorted, especially for $NbO_6$ with shorter Nb-O bond lengths towards the interlayer, as shown in the Figure 5.1c. The interlayer alkali cations are exchangeable, and may be used to exfoliate the compounds via intercalation of alkyl amines or protons/tetrabutylammonium cations. The n = 1 Ruddlesden-Popper $NaYTiO_4$ was also prepared as a precursor, although it is not known to exfoliate.

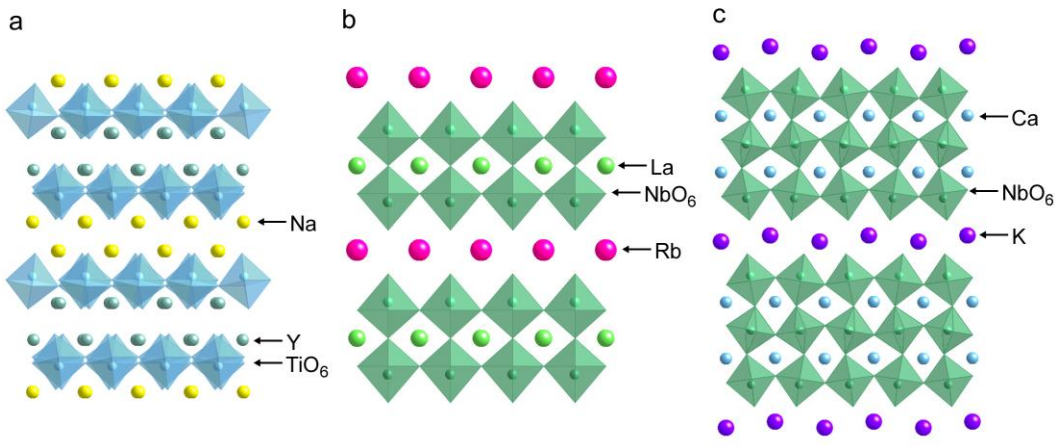


Figure 5.1: Structures of the (a) $NaYTiO_4$, (b) $RbLaNb_2O_7$, and (c) $KCa_2Nb_3O_{10}$

The strategy to obtain mixed valence was to reductively exchange fluorine with one of the oxygen atoms in the lattice. For example, one of the oxygen atoms in $RbLaNb_2O_7$ could be replaced to obtain $RbLaNb_2O_6F$, and in doing so the formal oxidation state of $Nb^{+5}$ is reduced to $Nb^{+4.5}$. The same mixed valence can also be obtained by the formula $KCa_2Nb_3O_9F$. When the fluorine exchanges with oxygen, it has a choice between a number of crystallographic sites—in $RbLaNb_2O_7$, there are the O1, O2, and O3 sites, which are the central, equatorial, and apical oxygens respectively (see Figure 5.3, pg. 10). The multiplicity of these sites are 1, 4, and 2; so other than energetics, statistical factors may also come into play.

Choosing a fluorinating agent compatible with reducing conditions led us to adopt the use of fluoropolymers such as poly(vinylidene fluoride) (PVDF, $(CH_2CF_2)_n$), and poly(tetrafluoroethylene) (PTFE, $((CF_2)_n$). Here, the carbon in the fluoropolymer acts as a reducing agent, ideally leaving the system as $CO_2$. A possible reaction of $RbLaNb_2O_7$ and PTFE under an inert atmosphere is shown below (Equation 5.1) :

$$2\ RbLaNb_2O_7 + CF_2 \rightarrow 2\ RbLaNb_2O_6F + CO_2 \qquad 5.1$$

The recent use of PVDF in the synthesis of the oxyfluorides $Sr_2TiO_3F_2$,[17] $Ca_2CuO_2F_2$,[17] and $SrFeO_2F$ [18] mainly by Slater and co-workers originally introduced us to the use of fluoropolymers. The stoichiometry of PVDF, however, makes a wider range of reactions and products possible, including a carbon residue (Equation 5.2) :

$$2\ RbLaNb_2O_7 + CH_2CF_2 \rightarrow 2\ RbLaNb_2O_6F + C + H_2O + CO \qquad 5.2$$

Depolymerization may also occur at competing rates, so the true pathway is not known—however, based on the higher fluorine content and potential to leave no carbonaceous residue, PTFE would be the preferred fluorine precursor.

## Experimental

$RbLaNb_2O_7$ was prepared by heating $Rb_2CO_3$ (25% excess), $La_2O_3$ (pre-treated at 900 °C for 24 hr), and $Nb_2O_5$ at 850 °C for 30 minutes, then at 1100 °C for 2 days. $NaYTiO_4$ was prepared by heating $Na_2CO_3$ (20% excess), $Y_2O_3$, and $TiO_2$ for 900 °C for 1 day, while $KCa_2Nb_3O_{10}$ was prepared by mixing $K_2CO_3$ (10% excess), $CaCO_3$, and $Nb_2O_5$ and heating at 1200 °C for 10 hours. After cooling, all parent materials were washed with water 2-3 times to ensure no excess alkali species remained.

Fluorination reactions were typically carried out by intimately mixing 0.5 g of the parent oxide with 1.2 eq or 0.6 eq of either poly(vinylidene fluoride) (PVDF, Alfa Aesar) or poly(tetrafluoroethylene) (PTFE, Sigma-Aldrich, 1 micron powder) under ethanol (1 eq. is the stoichiometrically necessary amount to yield $RbLaNb_2O_6F$). The mixtures were pressed into 13 mm pellets, loaded on a passivated copper boat, and heated to 400 °C for 12 hours at 10 °C/min under flowing nitrogen. In some cases, a second fluorination was conducted by grinding the pellets with additional fluoropolymer, pelletizing, and heating at the same conditions. The samples have no detectable color change over a period of a few weeks.

Proton exchange of $RbLaNb_2O_6F$ was accomplished by shaking 0.44g of $RbLaNb_2O_{7-x}F_x$ (prepared by two 1.2 eq fluorinations using PVDF) in 50 mL of 1 M nitric acid. The acid was replaced daily for five days before final centrifugation, washing with water (three times) and ethanol (twice) followed by drying at 60 °C in air for 15min.

X-ray diffraction patterns were obtained using Cu-$K_{\alpha 1}$ radiation on a Scintag Pad V diffractometer operating in Bragg-Brentano geometry. For lattice parameter refinement and Rietveld analysis, silicon powder was added as an internal standard. Data for Rietveld refinement were acquired by scanning from 5-90° with a step scan of 0.015° and a count time of 2.5 seconds. Rietveld analysis was conducted using the GSAS package[19] with the EXPGUI interface.[20]

Elemental analyses were conducted by Atlantic Microlab (Norcross, Georgia).

TEM studies were conducted on either a JEOL-2010 $LaB_6$ (200 kV) or JEOL-2010F (200 kV) electron microscope. Electron energy-loss spectra were recorded on the JEOL 2010F instrument using convergent beam diffraction mode.

Electronic structure calculations were carried out using the generalized gradient approximation (GGA) exchange correlation and the full-potential linearized augmented plane wave (FLAPW) method as implemented in the WIEN2k package.[21] 300 k-points gave reasonable convergence for the insulating parent and metallic products; non-spin-polarized calculations were performed using the total energy as the convergence criterion. Structural data were entered as obtained from Rietveld refinement results, without further optimization. For the fluorinated products, supercell calculations were costly and hence a virtual crystal approximation (VCA) was adopted. This entails using a pseudoatom which has averaged properties between fluorine and oxygen (for example, it may have an atomic number of 8.5) and placing it at the various oxygen sites.

## Results and Discussion

### Reactivity and Chemical Analysis

All three starting parent perovskites are white compounds, but upon reaction of the fluoropolymer, they turn into a dark grey-black with an occasional blue or brown tint. This change in color is somewhat expected, as the lanthanum niobate perovskites $RbLaNb_2O_7$ and $HLaNb_2O_7$ also change to a blue-black color upon reduction under hydrogen at elevated temperatures.[22] The reduced compounds would be $d^1$ compounds with a slightly populated $t_{2g}$ conduction band, and delocalization would cause a black color as in graphite. In the hydrogen-reduced sample, the bluish tint is from the intervalence charge transfer absorption at 1100nm.

While the fluorinated products of $NaYTiO_4$, $RbLaNb_2O_7$, and $KCa_2Nb_3O_{10}$ do have the characteristic grey-black color, it is important to determine how much of this reduction is due to fluorine exchange, or whether it might simply be due to a

carbothermal reduction (i.e. the formation of $RbLaNb_2O_{6.5}$ rather than $RbLaNb_2O_6F$, for example). The possibility of a carbothermal reduction was investigated by heating $RbLaNb_2O_7$ with polyethylene or activated carbon such that the added amount of carbon was the same as in the PVDF or PTFE samples. The XRD diffraction patterns in Figure 5.2a show a structural change only when a fluoropolymer is used, that is, the 001 peak at 8° has shifted to a lower angle (see Figure 5.2b) , and the previously overlapping peaks near 32.5 ° have also shifted to reveal three peaks (110, 004, and 111 reflections; see Figures 5.2a,c). After reaction, the products treated with polyethylene and activated carbon were only a light to medium grey, as opposed to the almost black PTFE/PVDF-derived samples. Based on these observations, we may assume that the presence of fluorine is necessary for a reduced product, and F anion exchange is the likely reaction at hand. It was also observed that the activated carbon sample before reaction was a medium grey before reaction, so the black color of the fluorinated products is not solely due to residual carbon.

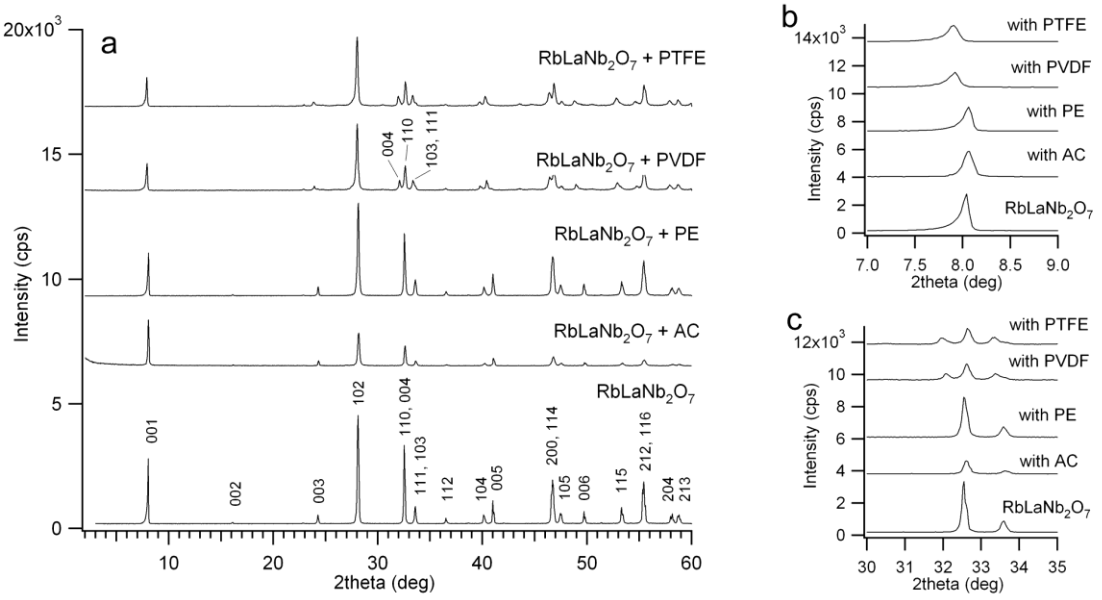


Figure 5.2: XRD patterns of $RbLaNb_2O_7$ and reaction products. PTFE = poly(tetrafluoroethylene), PVDF = poly(vinylidene fluoride), PE = polyethylene, AC = activated carbon. $RbLaNb_2O_7$ was ground and pelletized with 1.2 eq of PTFE or PVDF while activated carbon and polyethylene were added so that an amount of carbon equal to that of the PVDF sample was obtained.

Elemental analysis obtained by flame combustion analysis on the fluorinated compounds are summarized below in Table 5.1. The C/F ratios of the PVDF-treated products are above 1.00. Since the C/F ratio in PVDF is 1.00, this means that after reaction the samples are enriched in carbon and deficient in fluorine, which is the opposite of what we would expect. However, based on the structural changes and color changes observed earlier, we may still deduce that although much fluorine is volatilized and lost, the remaining fluorine does become incorporated into the oxide lattice. XRD shows that the remaining carbonaceous residue transforms into graphite fluoride upon heating the pellet at 600°C.

The middle rows of Table 5.1 show that oxyfluoride samples prepared from PTFE also showed significant amounts of carbonaceous residue. However, the C/F ratios remained close to the initial 0.5 ratio of the precursor fluoropolymer. Adding PTFE in smaller amounts (0.6 eq) but with multiple grindings yielded samples with lower carbon contaminant. Based on the total amount of fluorine and carbon present in the samples, we may deduce what the fluorine content in the oxide is. At one extreme, all of the fluorine detected may be located in oxyfluoride compound; the opposite, more pessimistic assumption is that fluorine is first bound to the carbon as graphite fluoride (terminal composition CF) and only the remaining fluorine is present as an oxyfluoride. The smaller the carbon contaminant is, the smaller this uncertainty of $x$ in the formula $RbLaNb_2O_{7-x}F_x$ is. As shown in the bottom two lines of Table 5.1, the samples treated with 0.6 eq of PTFE twice have a fluorine content such that $x$ is approximately 0.5-0.7 and while after three grindings $x$ is 0.86-1.3. Hence, we tentatively refer to these products with the formulae $RbLaNb_2O_{6.4}F_{0.6}$ and $RbLaNb_2O_6F$. Attempts were made to remove the excess carbon by treatment at 400°C in air for 12 hours, however; a white product was obtained, indicating the oxidation of Nb and loss of mixed valency.

The use of electron microprobe-based techniques such as X-ray energy-dispersive spectroscopy (EDS) or electron energy loss spectroscopy (EELS) in conjunction with TEM would be more helpful in determining the true O/F ratio of the oxide particles. However, the use of EDS does not give a definitive answer since the F $K_{\alpha 1}$ peak and La $M_{\alpha 1}$ peak overlap. The use of EELS is more suitable given its higher energy resolution

and sensitivity to light elements; however, preliminary studies showed that fluorine amount in most particles to be extremely low. Although further studies are necessary, during acquisition, an intense electron beam is focused to a fine point, so this may cause fluorine to volatilize.

Efforts were also made to reduce the carbon impurity and increase the crystallinity of the products by heating at higher temperatures. However, prolonged heating at 500 °C or heating at 600 °C resulted in a pellet with a white coating on the outside, and XRD shows that the unit cell has changed back to dimensions very close to that of the parent material.

Table 5.1: Elemental analysis (C,F) results for various fluorinated product mixtures. $F_x$ is the fluorine content in the chemical formula $RbLaNb_2O_{7-x}F_x$.

| Sample | C wt% | F wt% | C/F ratio | $F_x$ |
|---|---|---|---|---|
| $RbLaNb_2O_7$ + 1.2 eq PVDF, pre-rxn | 2.78 | 4.40 | 1.00 | |
| $RbLaNb_2O_7$ + 1.2 eq PVDF, post-rxn | 2.75 | 3.18 | 1.37 | |
| product above + 1.2 eq PVDF, post-rxn | 5.02 | 5.12 | 1.55 | |
| | | | | |
| $RbLaNb_2O_7$ + 1.2 eq PTFE, pre-rxn | 1.36 | 4.30 | 0.50 | |
| $RbLaNb_2O_7$ + 1.2 eq PTFE, post-rxn | 1.01 | 3.31 | 0.48 | 0.0-0.9 |
| product above + 1.2 eq PTFE, post-rxn | 1.53 | 4.74 | 0.51 | 0.0-1.3 |
| | | | | |
| $RbLaNb_2O_7$ + 0.6 eq PTFE, x2 | 0.44 | 2.44 | 0.29 | 0.5-0.7 |
| $RbLaNb_2O_7$ + 0.6 eq PTFE, x3 | 0.93 | 4.44 | 0.33 | 0.86-1.3 |

**Structural Change**

Table 5.2. compares the unit cell parameters of various oxyfluoride products. Fluorination of $RbLaNb_2O_7$ resulted in a unit cell with a longer *c* axis but a *smaller a* parameter, with more distortion resulting at higher degrees of fluorination. Fluorination of $NaYTiO_4$ led to an increased *c* parameter (from 12.21 Å to 12.95 Å), and the *a*, *b* parameters also increased somewhat. The n = 3 compound $KCa_2Nb_3O_{10}$ showed a much smaller structural change at the same reaction conditions despite the almost identical

colored product. In general, it seems that the more octahedral layers are contained in each layer slab, the less the change in the unit cell parameters is. $RbLaTiNbO_6F$ and $RbSrNb_2O_6F$ are layered perovskites very similar to the $RbLaNb_2O_6F$ prepared in this study. The lattice parameters match well with that of $RbSrNb_2O6_6F$, notably the reduced *a* and elongated *c* parameters.

Table 5.2: Lattice parameters of various layered perovskites

| | Space group | *a* (Å) | *b* (Å) | *c* (Å) | Vol. (Å$^3$) |
|---|---|---|---|---|---|
| $RbLaNb_2O_7$ (lit.)[a] | *P4/mmm* | 3.885(2) | 3.885(2) | 10.989(3) | 165.86 |
| $RbLaNb_2O_7$ (lit.)[b] | *P4/mmm* | 3.896(9) | 3.896(9) | 11.027(2) | 167.38 |
| $RbLaNb_2O_7$ (this work) | *P4/mmm* | 3.89170(9) | 3.89170(9) | 11.0072(4) | 166.71 |
| $RbLaNb_2O_{6.4}F_{0.6}$ | *P4/mmm* | 3.87650(14) | 3.87650(14) | 11.1916(7) | 168.18 |
| $RbLaNb_2O_6F$ | *P4/mmm* | 3.86575(16) | 3.86575(16) | 11.2135(7) | 167.58 |
| $RbSrNb_2O_6F$ [c] | *P4/mmm* | 3.850 | 3.850 | 11.284 | 167.26 |
| $RbLaTiNbO_6F$ [d] | *P4/mmm* | 3.860(1) | 3.860(1) | 10.980(3) | 163.60 |
| $NaYTiO_4$ [e] | *Pbcm* | 12.2134(3) | 5.3517(3) | 5.3509(3) | 349.75 |
| $NaYTiO_{3-x}F_x$ | *Pbcm* | 12.9439(21) | 5.3858(9) | 5.3658(7) | 374.07 |
| $KCa_2Nb_3O_{10}$ [f] | *Cmcm* | 3.8802(9) | 29.508(6) | 7.714(1) | 883.42 |
| $KCa_2Nb_3O_{10-x}F_x$ | *Cmcm* | 3.8709(4) | 29.5676(32) | 7.7064(9) | 882.02 |

[a] Ref.23, [b] Ref.24, [c] Ref. 25, [d] Ref. 26, [e] Ref.27, [f] Ref. 28

It is difficult to determine what sites the F atoms occupy, since the X-ray and neutron scattering factors for oxygen and fluorine are very close to each other. As mentioned earlier, for the n = 2 $RbLaNb_2O_{7-x}F_x$ compound, there are three possibilities, namely the central O1 position, the equatorial O2 position, and the apical O3 position (see Figure 5.3). In general, fluorine does not seem to occupy the apical O3 site, since the shorter Nb-O3 bond length implies covalent character, and oxygen, rather than fluorine, would have a stronger tendency to participate in such a bond. For example, concerning $KSrNb_2O_6F$ (*Immm*), Yoo *et al* conclude based on bond sum valence calculations that F orders in the equatorial O2 position.[29] In their $RbLaTiNbO_6F$ compound, Caruntu *et al* refined the structure with F placed at the O1 and O2 sites,[26] and Choy *et al* find that for

$RbSrNb_2O_6F$, $^{19}F$-NMR and lattice energy calculations suggest that the F is distributed over the central and equatorial sites (O1, O2). For the newly synthesized $RbLaNb_2O_6F$, electronic structure calculations were conducted to compare the total electronic energies of the sructures with the fluorine distributed over the various oxygen sites (Table 5.3) We find that the oxyfluorides have a lower total electronic energy than the parent $RbLaNb_2O_7$, however, the magnitude of this difference is disturbingly large (61 MJ/mol!) The different fluorine distributions also have very large energy differences – each site distribution differs in energies of 2000 – 3000 kJ/mol. In contrast, Choy *et al* found their different fluorine distributions in $RbSrNb_2O_6F$ to differ by only 60 – 1000 kJ/mol. The reason for this discrepancy is unknown. Total energy calculations were indeed conducted on Rietveld parameters rather than unoptimized structures, but calculations on $RbLaNb_2O_7$ with the fluorinated product's unit cell (i.e. different structure) still yielded a similar result. In comparing the relative stabilities of the $RbLaNb_2O_6F$ structures, we find fluorine at O1 to be the most stable case (same as in $RbSrNb_2O_6F$); the next stable site however is O3 and then O2. Total electronic energy calculations on Choy's $RbSrNb_2O_6F$ also result in the same stability order (with the same magnitudes of energy separating the distributions), so the disagreement is systematic.

Table 5.3: Comparison of total electronic energies and lattice energies for compounds with various fluorine distributions. The multiplicities of sites O1, O2, and O3 are 1, 4, and 2 respectively, resulting in the partial filling of the O2, O3 sites by fluorine.

| | F site | Total energy | Relative energy | Lattice energy |
|---|---|---|---|---|
| $RbLaNb_2O_7$ | n/a | -39295.0736 Ry/cell | + 61761 kJ/mol | |
| $RbLaNb_2O_7$ (with unit cell same as below) | | -39295.0250 Ry/cell | | |
| $RbLaNb_2O_6F$ | O1 (100%) | -39344.3354 Ry/cell | - 2899.67 kJ/mol | |
| | O2 (25%) | -39341.1174 Ry/cell | + 1324.3 kJ/mol | |
| | O3 (50%) | -39342.1263 Ry/cell | 0 kJ/mol | |
| $RbSrNb_2O_6F$ | O1 (100%) | -28708.740354 Ry/cell | | 4211.904 kJ/mol |
| | O2 (25%) | -28705.453859 Ry/cell | | 4148.496 kJ/mol |
| | O3 (50%) | -28706.466701 Ry/cell | | 2864.88 kJ/mol |

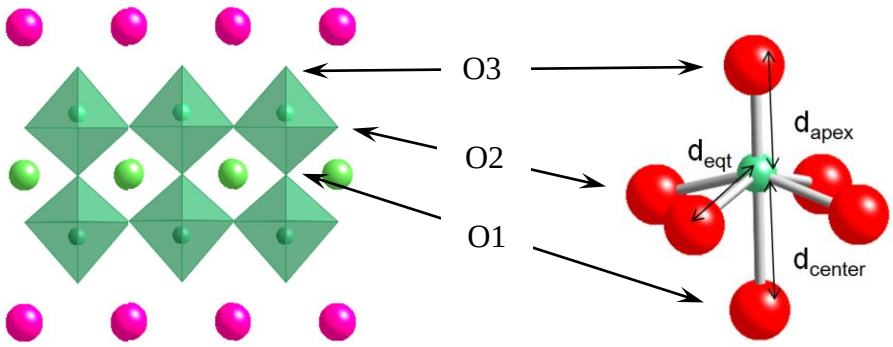


Figure 5.3: Oxygen sites of $RbLaNb_2O_{7-x}F_x$ and a $NbO_{6-a}F_a$ octahedron

Rietveld refinement (Figure 5.4) was performed on the $RbLaNb_2O_7$ parent material, $RbLaNb_2O_{6.4}F_{0.6}$, and $RbLaNb_2O_6F$. All samples were refined using a tetragonal *P4/mmm* space group. For the oxyfluorides, in all three samples the $NbO_6$ octahedra are distorted such that the Nb-O1 bond is longer than the other bonds and the octahedron is "puckered" so that the Nb atom and the equatorial O2 atoms are not coplanar (see Table 5.4 for select bond lengths and angles). Fluorination seems to decrease the distortion angle (defined by O2-Nb-O2), a trend followed by $RbSrNb_2O_6$. Refinements were also conducted with vacancies at the various oxygen sites, but these failed to give any meaningful results as the occupancy factor for some of the oxygen sites was usually forced to converge at values above 1. Thermal parameters for the atoms was fixed at 0.025 regardless of site or atom, since fitting yielded slightly negative factors on the oxygen atoms. The atomic positions for $RbLaNb_2O_7$ and $RbLaNb_2O_6F$, as found by Rietveld analysis, have been listed in Table 5.5.

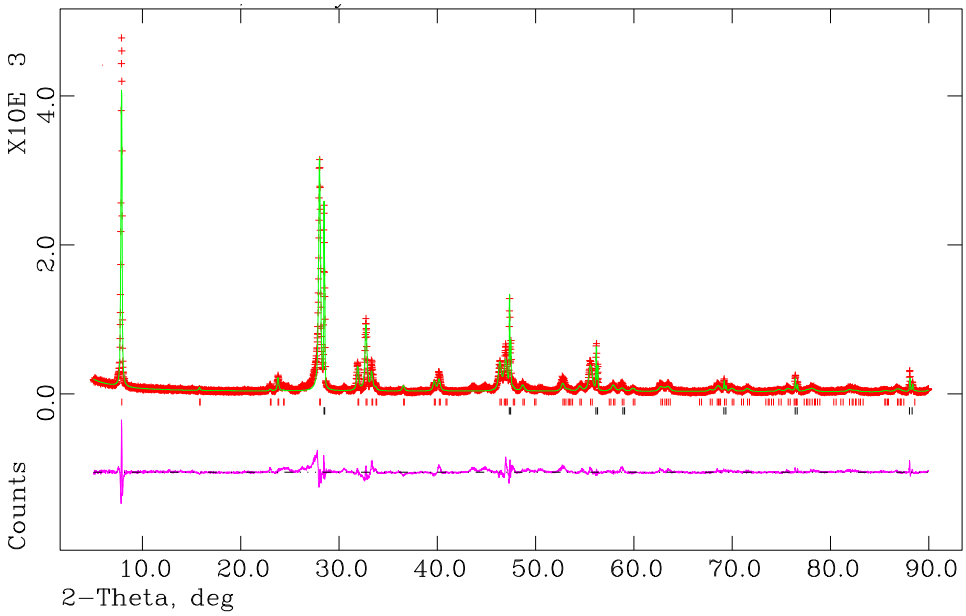


Figure 5.4: Rietveld refinement of $RbLaNb_2O_6F$; top red ticks indicate Bragg reflections of the product phase, and black ticks indicate Bragg reflections of silicon powder (internal standard)

Table 5.4: Select bond lengths of $RbLaNb_2O_7$ and related oxyfluorides

| | $RbLaNb_2O_7$ | $RbLaNb_2O_{6.4}F_{0.6}$ | $RbLaNb_2O_6F$ | $RbSrNb_2O_6F$ |
|---|---|---|---|---|
| $d_{apex}$ | 1.770 Å | 1.821 Å | 1.693 Å | 1.726 Å |
| $d_{center}$ | 2.274 Å | 2.319 Å | 2.334 Å | 2.361 Å |
| $d_{eqt}$ | 2.016 Å | 1.983 Å | 1.996 Å | 1.988 Å |
| distortion | 149.6° | 155.7° | 151.2° | 154.1° |

Table 5.5: Table of atomic positions for $RbLaNb_2O_7$ and $RbLaNb_2O_6F$

| | Atom | Pos. | *x* | *y* | *z* |
|---|---|---|---|---|---|
| $RbLaNb_2O_7$ | Rb | 1d | 0.5 | 0.5 | 0.5 |
| *P4/mmm* (123) | La | 1c | 0.5 | 0.5 | 0.0 |
| *a* = 3.89170(9) | Nb | 2g | 0.0 | 0.0 | 0.20657 |
| *c* = 11.072(4) | O1 | 1a | 0.0 | 0.0 | 0.0 |
| | O2 | 4i | 0.0 | 0.5 | 0.15856 |
| | O3 | 2g | 0.0 | 0.0 | 0.36378 |
| | | | $\chi^2$ =2.2%, $R_{wp}$ = 21%, $R_p$ = 15 % | | |
| $RbLaNb_2O_{6.4}F_{0.6}$ | Rb | 1d | 0.5 | 0.5 | 0.5 |
| *P4/mmm* (123) | La | 1c | 0.5 | 0.5 | 0.0 |
| *a* = 3.87650(14) | Nb | 2g | 0.0 | 0.0 | 0.79281 |
| *c* = 11.1916(7) | O/F 1 | 1a | 0.0 | 0.0 | 0.0 |
| | O/F 2 | 4i | 0.0 | 0.5 | 0.83006 |
| | O/F 3 | 2g | 0.0 | 0.0 | 0.64011 |
| | | | $\chi^2$ = 4.3%, $R_{wp}$ = 22%, $R_p$ = 16 % | | |
| $RbLaNb_2O_6F$ | Rb | 1d | 0.5 | 0.5 | 0.5 |
| *P4/mmm* (123) | La | 1c | 0.5 | 0.5 | 0.0 |
| *a* = 3.86575(16) | Nb | 2g | 0.0 | 0.0 | 0.79183 |
| *c* = 11.2135(7) | O/F 1 | 1a | 0.0 | 0.0 | 0.0 |
| | O/F 2 | 4i | 0.0 | 0.5 | 0.83613 |
| | O/F 3 | 2g | 0.0 | 0.0 | 0.64082 |
| | | | $\chi^2$ = 5.5%, $R_{wp}$ = 24%, $R_p$ = 17 % | | |

Although the *P4/mmm* space group accounts for all reflections observed in the X-ray diffraction pattern, electron diffraction has a larger apparent dynamic response, and can frequently show supercell reflections not visible by XRD. In Figure 5.5, an electron diffraction pattern looking down the 001 zone axis shows faint spots (slightly streaked) at *d*-spacings larger than $d_{001}$. The faint spots suggest a 4*a* x 4*a* superstructure, with certain symmetry elements extinguishing some of the spots. This may be due to some cooperative tilting of the octahedra,[30] although it is difficult to assign a new space group. Since we do not see these superstructure reflections in the parent $RbLaNb_2O_7$ phase, they are due to structural distortions caused by introducing fluorine.

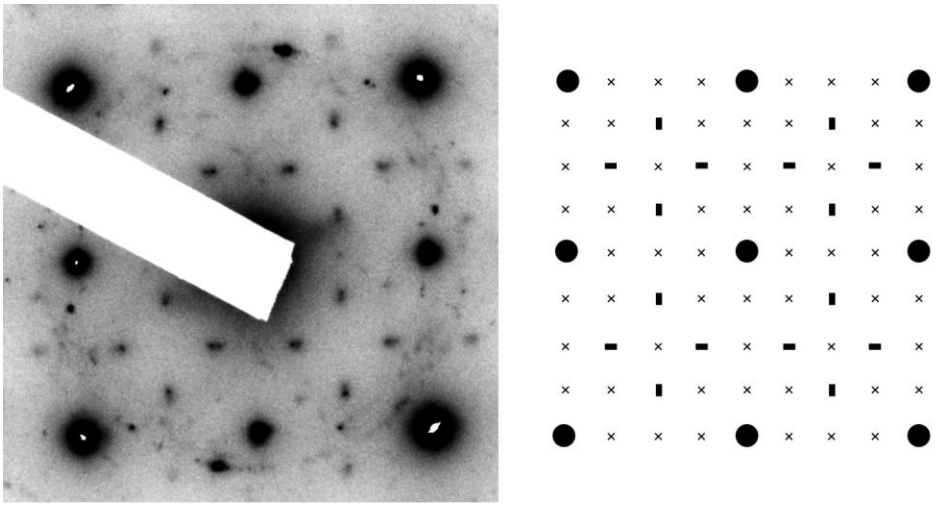

Figure 5.5: Selected area diffraction pattern of $RbLaNb_2O_{7-x}F_x$, 001 zone axis.

**Electronic Structure**

Most of the cation-exchangeable layered perovskites are insulating $d^0$ systems. The total and partial density of states (t-DOS, p-DOS) for $RbLaNb_2O_7$ is shown in Figure 5.6; the total DOS shows a band gap of only approximately 1.2 eV. This is a large underestimation, as most such white niobium oxide compounds should have a band gap of 3-4 eV. Regular DFT calculations using LDA (local density approximation) or GGA (generalized gradient approximation) for the exchange correlation potential are known to routinely underestimate the bandgaps of insulators or semiconductors; however, relative band gap changes and other features of the density of states are known to be reasonably accurate.[31-34] Throughout the plots of the partial density of states, it should be noted that the figures plot the partial density of states per atom without accounting for crystallographic site multiplicity. For example, the site multiplicities for O1, O2 , and O3 are 1, 4, and 2 respectively, so when comparing the O1, O2, and O3 p-DOS (Figure 5.6c), one must keep in mind that the height of the trace for O2 should be multiplied by 4, etc. Examining the plots shows that Nb 4d – O 2p hybridization occurs mainly between Nb

and O2, O3 rather than with the central O1. This is somewhat similar to the hybridization found in $RbCa_2Ta_3O_{10}$, where Machida *et al* also find the equatorial oxygens hybridizing the most with Nb.[35] However, the same authors also find in their compound that the apical oxygens mainly contribute to the maximum of the valence band, where as the O1 p-DOS (red trace, third plot of Figure 5.6) is the largest contributor for $RbLaNb_2O_7$.

The conduction bands are essentially a superposition of the empty La (4f) states at 4.5 eV superimposed on to $t_{2g}$ (at 1-5 eV) and $e_g$ (at 6-10 eV) type bands. The original Nb 4d components of the $t_{2g}$ and $e_g$ bands are what one would expect; namely, the $dz^2$ and $dx^2$-$y^2$ orbitals (red, green traces, Figure 5.6d) contribute to the upper $e_g$ band, while the $d_{xy}$, $d_{xz}$, $d_{yz}$ orbitals form the $t_{2g}$ band. The two dimensional crystal structure causes the in-plane $d_{xy}$-derived band (blue trace) to form its own band at the minimum of the conduction band.

Reductive fluorination results in injecting an extra electron which occupies this $d_{xy}$ type band, resulting in a 2-D metallic compound. Figure 5.7, Figure 5.8 and Figure 5.9 show the density of states for the fluorinated product $RbLaNb_2O_6F$, with F at the various O1, O2, and O3 sites. The Fermi level indicated by the dotted line shows that In general, such 2-D metallicity would be the expected case for any fluorinated layered $d^x$ system where d = 0 – 1; hence, fluorination yields a convenient pathway for possibly transforming the insulating layered perovskites into 2-D metallic conductors. Tobias *et al* also mention this as the general case, and most *n*=2 Ruddlesden-Popper and Dion-Jacobson phases are expecteded to have 2D metallic behavior. It is possible, however, that disorder of oxygen and fluorine may cause electron localization, resulting in a thermally activated semiconductor—the virtual crystal approximation (calculations conducted here) would not account for this. The fact that the multiplicity of the O1 site is one is somewhat encouraging, since there is no chance O-F disorder if the fluorine occupies only the O1 site.

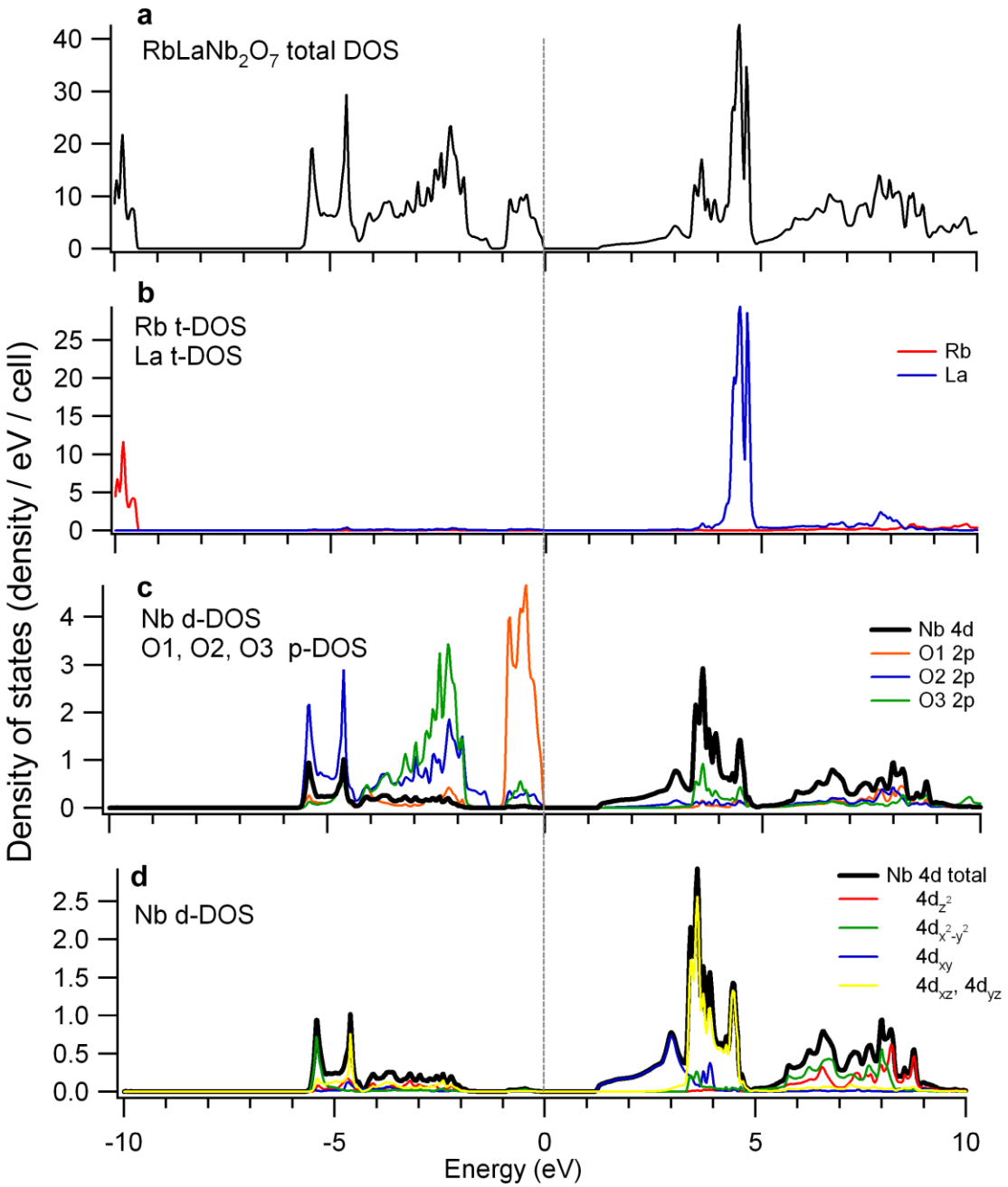


Figure 5.6: Partial and total density of states for $RbLaNb_2O_7$. The dotted line indicates the Fermi energy.

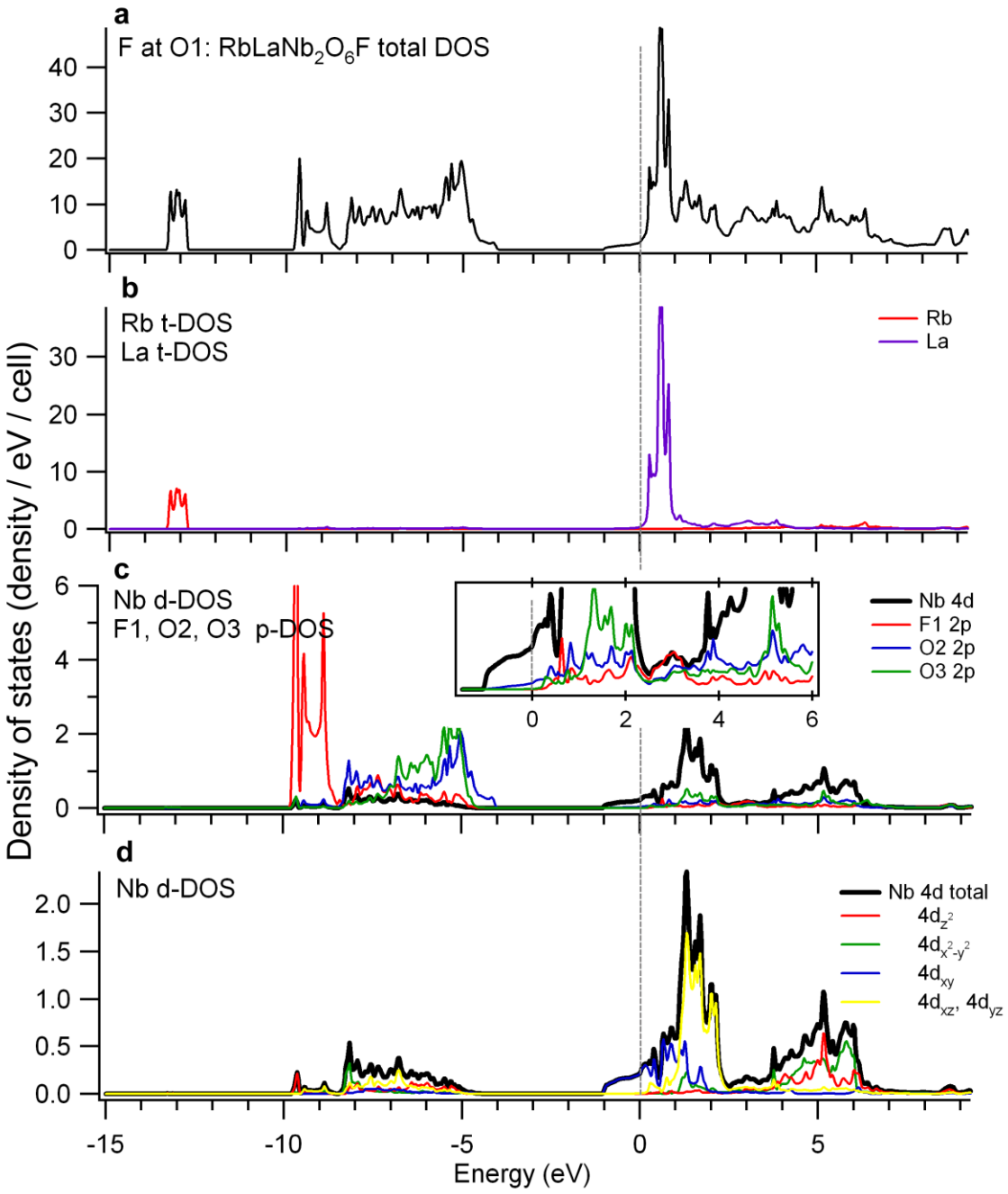


Figure 5.7: Partial and total density of states for $RbLaNb_2O_6F$, with fluorine at the O1 site

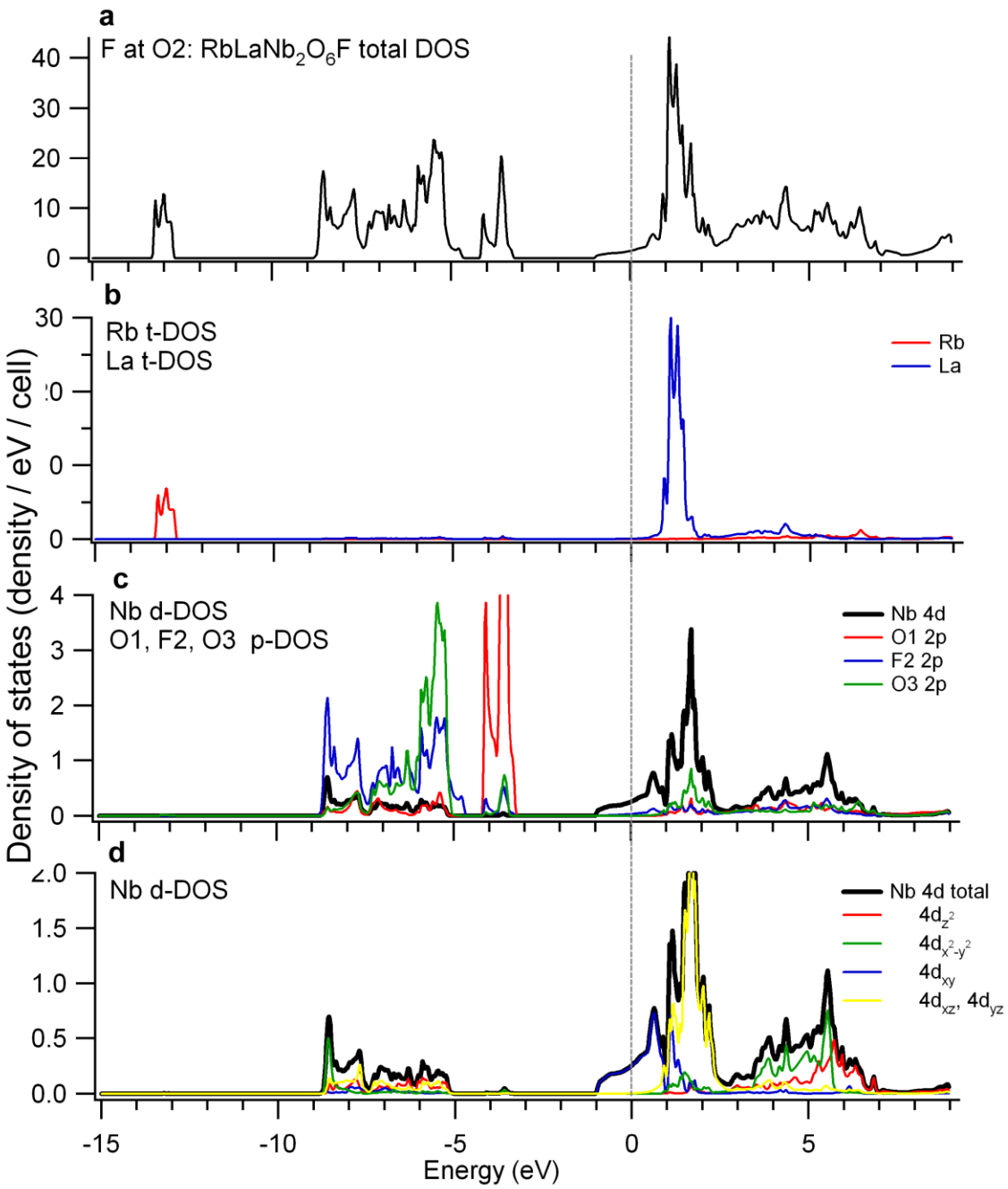


Figure 5.8: Partial and total density of states for $RbLaNb_2O_6F$, with fluorine at the O2 site

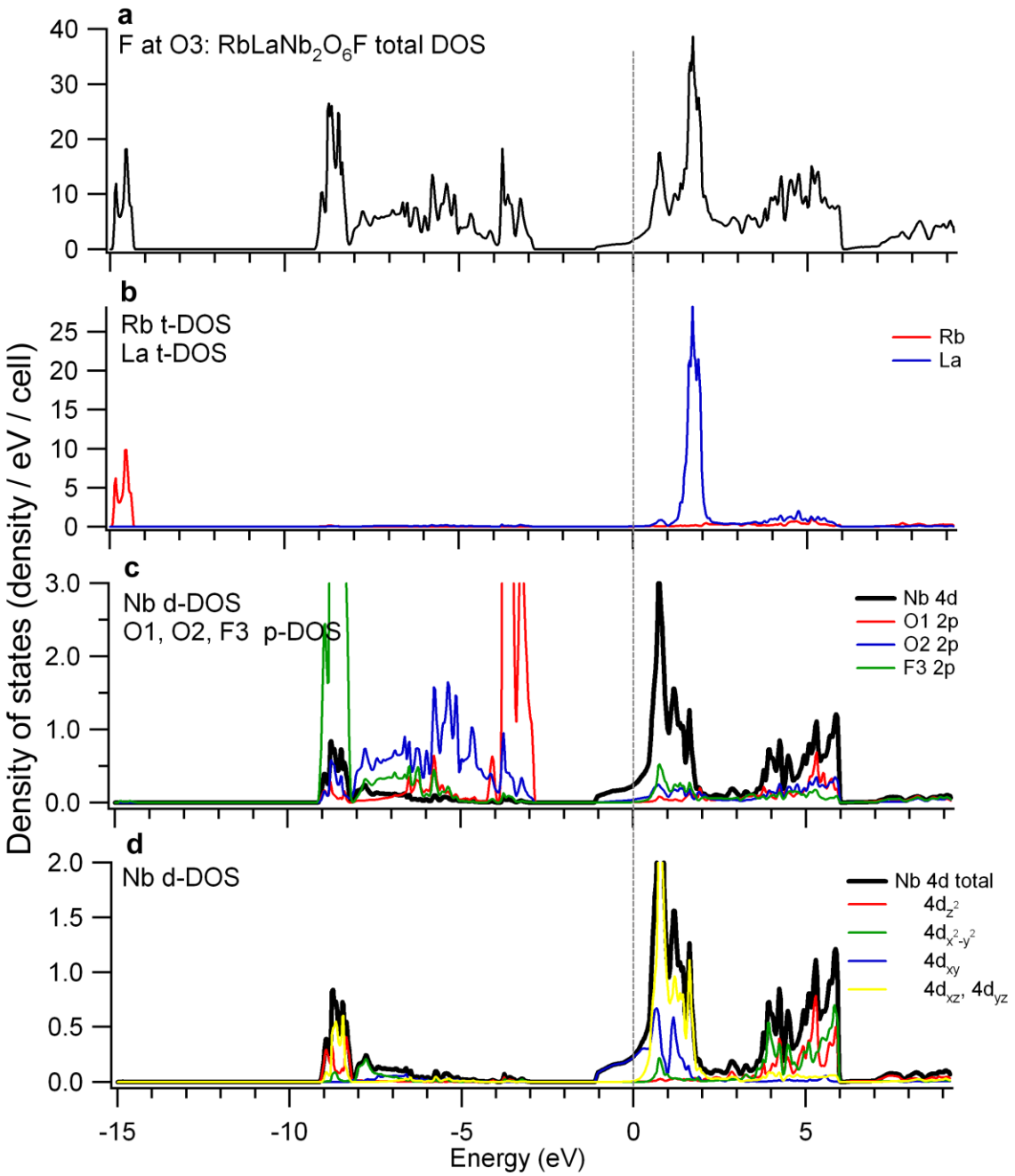


Figure 5.9: Partial and total density of states for $RbLaNb_2O_6F$, with fluorine at the O3 site

**Ion Exchange/Exfoliation**

The layered perovskites $RbLaNb_2O_7$ and $KCa_2Nb_3O_{10}$ may be treated in aqueous acid to yield the proton-exchanged products $HLaNb_2O_7$ and $KCa_2Nb_3O_{10}$. These products may then be treated with aqueous tetra-*n*-butylammonium hydroxide; the acid-base reaction eliminates the interlayer proton, and the layered material exfoliates as soon as the bulky tetra-*n*-butylammonium cation intercalates.

The oxyfluoride $RbLaNb_2O_7F$ also seems into be ion-exchangeable. Figure 5.10 shows that after acid treatment, the 00l peak at 8° has shifted to two split peaks at 7.1° ($d_{001}$ = 12.4 Å)and 7.5° ($d_{001}$ = 11.8 Å). The increase in interlayer spacing with the exchange of a smaller cation $H^+$ is probably due to hydrated protons in the interlayer. The product in suspension and after isolation as a dry powder appears to have the same black color of the Rb precursor, so visually there appears to be no drastic oxidation upon proton exchange. Elemental analysis indicated that the sample still contained 3.04% of fluorine. Further treatment with aqueous tetra-*n*-butylammonium hydroxide solution resulted in a fine colloidal suspension presumably containing exfoliated nanosheets; however, after centrifugation and removal of the carbon impurity, the remaining suspension is a light grey color, indicating the oxidation of the sheets. Assuming $RbLaNb_2O_6F$ survives the acid treatment intact, the exfoliation step has potential to reoxidize the sample as the niobium atoms are more exposed in exfoliated form, and $F^-$ ions may exchange with $OH^-$ ions. Alternate ion-exchange/exfoliation steps in anerobic conditions without the use of hydroxides present may be successful.

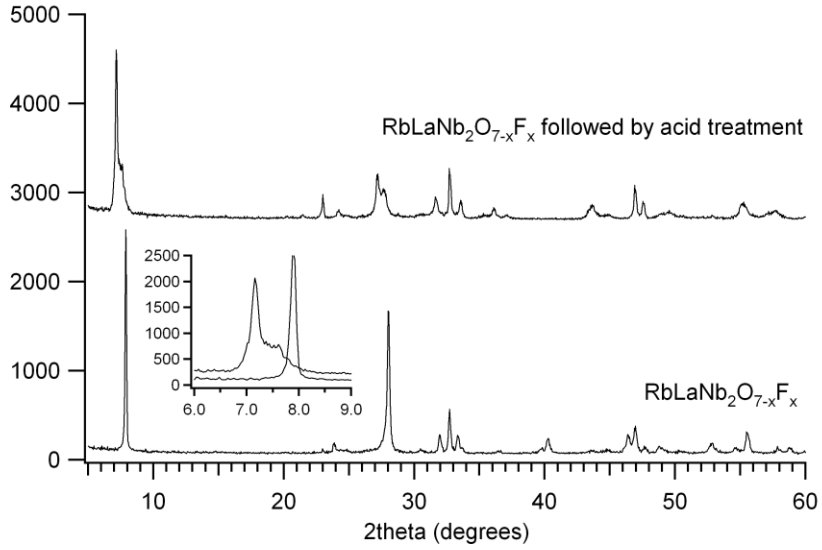


Figure 5.10: XRD patterns of $RbLaNb_2O_6F$ before and after treatment with 1M nitric acid

## Conclusions

Based on color and structural changes, it appears that the layered perovskites $RbLaNb_2O_7$, $KCa_2Nb_3O_{10}$ and $NaYTiO_4$ all react with fluoropolymers to obtain reduced products. The products do not change color over time in ambient atmosphere, and seem receptive to ion exchange. Preparing them in pure form without carbon impurity will make electric and magnetic characterizations possible; the high temperature syntheses of $RbLaTiNb_2O_6F$ and $RbSrNb_2O_7$ imply that $RbLaNb_2O_6F$ could be prepared from anaerobic solid state reaction of precursors such as RbF, $La_2O_3$, $NbO_2$, $Nb_2O_5$, etc. An alternate synthesis could entail the fluorination of $RbLaNb_2O_7$ in an alternate medium such as RbF/LiF/NaF flux under anerobic or vacuum conditions. Once a pure product is obtained, exfoliation could be conducted with a propylamine-intercalated product, possibly in a deoxygenated or organic solvent to prevent oxidation of the nanosheets. In general, it seems that reductive fluorine exchange is a valid way to obtain many metallic or conducting layered perovskites and nanosheets.

## References


1. Bednorz, J. G.; Müller, K. A. *Z. Phys. B: Condens. Matter* **1986,** *64*, 189-193.

2. Enz, C. P. *Lect. Notes Phys.* **1996,** *477*, 143-160.

3. Argyriou, D. N.; Mitchell, J. F.; Potter, C. D.; Bader, S. D.; Kleb, R.; Jorgensen, J. D. *Phys. Rev. B* **1997,** *55*, 11965-11968.

4. Mitchell, J. F.; Millburn, J. F.; Medarde, M.; Short, S.; Jorgensen, J. D.; Fernandez-Diaz, M. T. *J. Solid State Chem.* **1998,** *141*, 599-603.

5. Kudo, A.; Sakata, T. *J. Phys. Chem.* **1995,** *99*, 15963-15967.

6. Ida, S.; Ogata, C.; Unal, U.; Izawa, K.; Inoue, T.; Altuntasoglu, O.; Matsumoto, Y. *J. Am. Chem. Soc.* **2007,** *129*, 8956-8957.

7. Schaak, R. E.; Afzal, D.; Schottenfeld, J. A.; Mallouk, T. E. *Chem. Mater.* **2002,** *14*, 442-448.

8. Schottenfeld, J. A.; Benesi, A. J.; Stephens, P. W.; Chen, G.; Eklund, P. C.; Mallouk, T. E. *J. Solid State Chem.* **2005,** *178*, 2313-2321.

9. Tobias, G.; Canadell, E. *J. Am. Chem. Soc.* **2006,** *128*, 4318-4329.

10. Hase, I.; Nishihara, Y. *Phys. Rev. B* **1998,** *58*, 1707-1709.

11. Neiner, D.; Sweany, R. L.; Golub, V.; Wiley, J. B. *J. Mater. Chem.* **2006,** *16*, 186-191.

12. Lalena, J. N.; Cushing, B. L.; Falster, A. U.; Simmons, W. B.; Seip, C. T.; Carpenter, E. E.; O'Connor, C. J.; Wiley, J. B. *Inorg. Chem.* **1998,** *37*, 4484-4485.

13. Mcintyre, R. A.; Falster, A. U.; Li, S.; Simmons, W. B. J.; O'Connnor, C. J.; Wiley, J. B. *J. Am. Chem. Soc.* **1998,** *120*, 217-218.

14. Viciu, L.; Kodenkandath, T. A.; Wiley, J. B. *J. Solid State Chem.* **2007,** *180*, 583-588.

15. Armstrong, A. R.; Anderson, P. A. *Inorg. Chem.* **1994,** *33*, 4366-4369.

16. Toda, K.; Masaki, T.; Teranishi, T.; Ye, Z.-G.; Sato, M.; Hinatsu, Y. *J. Mater. Chem.* **1999,** *9*, 799-803.

17. Slater, P. R. *J. Fluorine Chem.* **2002,** *117*, 43-45.

18. Berry, F. J.; Ren, X.; Heap, R.; Slater, P. R.; Thomas, M. F. *Solid State Commun.* **2005,** *134*, 621-624.

19. Larson, A. C.; Von Dreele, R. B. "General Structure Analysis System (GSAS)" Los Alamos National Laboratory Report LAUR 86-748, 2000.

20. Toby, B. H. *J. Appl. Crystallogr.* **2001,** *34*, 210-213.

21. Blaha, P.; Schwarz, K.; Madsen, G. K. H.; Kvasnicka, D.; Luitz, J. **WIEN2k**, An Augmented Plane Wave + Local Orbitals Program for Calculating Crystal Properties (Karlheinz Schwarz, Techn. Universität Wien, Austria), 2001. ISBN 3-950131-1-2.

22. Gomez-Romero, P.; Palacin, M. R.; Casan, N.; Fuertes, A. *Solid State Ionics* **1993,** *63-65*, 424-428.

23. Gopalakrishnan, J.; Bhat, V. *Mater. Res. Bull.* **1987,** *22*, 413-417.

24. Kodenkandath, T. A.; Lalena, J. N.; Zhou, W. L.; Carpenter, E. E.; Sangregorio, C.; Falster, A. U.; Simmons, W. B.; O'Connor, C. J.; Wiley, J. B. *J. Am. Chem. Soc.* **1999,** *121*, 10743-10746.

25. Choy, J. H.; Kim, J. Y.; Kim, S. J.; Sohn, J. S.; Han, O. H. *Chem. Mater.* **2001,** *13*, 906-912.

26. Caruntu, G.; Spinu, L.; Wiley, J. B. *Mater. Res. Bull.* **2002,** *37*, 133-140.

27. Toda, K.; Kameo, Y.; Kurita, S.; Sato, M. *J. Alloys Compd.* **1996,** *234*, 19-25.

28. Fukuoka, H.; Isami, T.; Yamanaka, S. *J. Solid State Chem.* **2000,** *151*, 40-45.

29. Yoo, C.-Y.; Kun-Pyo, H.; Kim, S.-J. *Acta Crystallographica, C* **2007,** *63*, 63-65.

30. Aleksandrov, K. S.; Bartolome, J. *J. Phys.: Condens. Matter* **1994,** *6*, 8219-8235.

31. Chen, S.; Gong, X. G.; Wei, S.-H. *Phys. Rev.* **2007,** *75*, 205209.

32. Robertson, J.; Xiong, K.; Clark, S. J. *Phys. Status Solidi B* **2006,** *243*, 2054-2070.

33. Jones, R. O.; Gunnarsson, O. *Reviews of Modern Physics* **1989,** *61*, 689-746.

34. Machida, M.; Yabunaka, J.-i.; Kijima, T.; Matsushima, S.; Arai, M. *International Journal of Inorganic Materials* **2001,** *3*, 545-550.

35. Machida, M.; Mitsuyama, T.; Ikeue, K. *J. Phys. Chem. B* **2005,** *109*, 7801-7806.

# Appendix

## Details of Impedance Measurements

### Theory and Analysis of Electrochemical Impedance Measurements

An excellent starting point is the paper by Thangadurai *et al* in *Electrochemical Proceedings*, **2001**, *2001-28*, 109-128. Other papers by the principal authors are extremely relevant and helpful. Free modeling software ZView can be downloaded from www.scribner.com. A user may enter a model circuit with certain R and C values, and the software will simulate impedance spectra based on this; hence it is a very useful tool in learning. The help files of the software explain the various circuit elements succinctly. ZPlot and ZView are also used to acquire and fit impedance data from the Solartron instruments. Kramers-Krönig transformations can be conducted by using custom-written code provided by Prof. Digby D. Macdonald. To run this code, Microsoft Visual Studio .NET must be installed.

### Sample Preparation

Powder samples were prepared as pressed pellets. Typically, 0.5 g of material such as $HLaNb_2O_7$ pressed in a 13mm die produces a pellet 1 mm thick, which is a convenient thickness. Some materials, especially fine powders or those with high surface area tend to clog the die assembly, resulting in cracked pellets. This may be remedied by applying a very small amount of lubricant or releasing agent such as a zinc stearate spray onto the die assembly using a Kimwipe. Typically, pellets were pressed at 3 metric tons. XRD on ground pellets shows that crystallinity of $HLaNb_2O_7$ pellets pressed at 3, 6, 9 tons was noticeably different (i.e., broader peaks and an extra layer line appeared at higher pressures), so the pressing pressure should definitely be controlled.

After pressing, metal contacts may be evaporated or sputtered (sputtering is much cheaper and faster) onto both sides of the pellets. 100-150 nm of metal was sputtered for the samples in this work. It should be noted that Pt is semi-permeable to $H_2$, and Ag is semi-permeable to $O_2$, so these may act as non-blocking electrodes for measuring proton or oxide anion conductivity at elevated temperatures. A paper comparing the various metals can be found at *Solid State Ionics*, **2005**, *176*, 1429-1437, although it concerns pellets which can be sintered and measurements at relatively high temperatures.

Sputtering also covers the edges of the pellets with metal, so it is necessary to scrape the metal off the edges with a razor blade to avoid a short circuit.

## Conductivity/Impedance Measurements

A simple setup for conductivity is shown below Figure A.1, and should be convenient for measuring the electronic conductivity using the BAS electrochemical workstation in the lab. The setup could also be used for impedance measurements, if the measurement cell (described later) cannot be used:

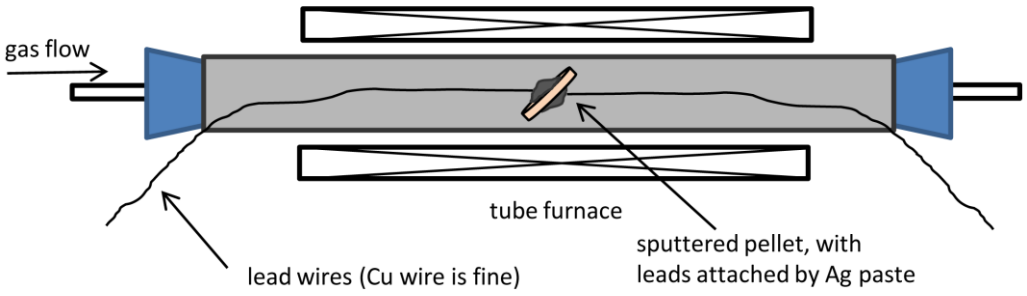


Figure A.1: Simple setup for conductivity using silver paste

Here, copper leads are pasted on to the pellets using a silver-filled adhesive. A good conducting adhesive is PYRO-DUCT 597-C by Aremco Products, but it has a limited shelf life of a few months; afterwards it is unusable. Compared to most silver-filled epoxies, it is rated to a high temperature (900°C), and has the same consistency as toothpaste, making it easy to put a dab on the pellet and apply the lead wire.

Equipment for acquiring impedance data is available at present only in the Macdonald lab (Hosler Rm 23 at time of writing). Impedance instrumentation could also be purchased as an add-on to the BAS electrochemical workstation, or as a PC card-based system from Gamry. These options are much cheaper than acquiring instrumentation from Solartron or HP, but are limited by their maximum frequencies (perhaps tens or hundreds of kHz instead of 1 MHz). This may not be a problem for some systems; however, materials with low conductivities (as these layered perovskites) typically require higher frequencies.

## Apparatus at the Macdonald Lab

### Electrochemical Equipment

Currently, the impedance equipment convenient for use is the Solartron 1287 (electrochemical interface) and 1255B (frequency response analyzer), which are connected to each other. 4 leads (BNC cable) extend from the interface; there are two reference electrodes (RE1, RE2), a counter electrode (CE1), and working electrode (WE2). For a typical two-point measurement, RE1 and CE1 are connected to form one electrode, and RE2 and WE2 are joined to form the other electrode. It has been recommended that RE1 and RE2 be closer along the wires to the sample, if possible. When joining the cables, the shielding should not be joined.

The software to acquire impedance data is Zplot, and the data is viewed using ZView. The impedance data is typically acquired by opening Zplot and choosing the "Constant E" tab, entering a bias of 0V, choosing an amplitude, frequency range, and clicking "acquire". For an aqueous or fairly conductive sample, an amplitude of only few tens of milivolts is necessary, but more resistive samples may require a few hundred milivolts. If warnings are shown on the computer monitor or 1287 panel, then the run should be quickly aborted. Noisy spectra can be smoothed by increasing the amplitude. However, the general features of the spectra should not be dependent on the amplitude;

otherwise it is an indication that the amplitude is probably too large and not in the linear range. Certain ‘kinks’ may be present in the spectra too. This may be due to operational amplifiers in the potentiostat switching, and if this is the case changing the amplitude may result in more visually pleasing spectra. A jump at 60 Hz is always observed, due to ambient line frequencies.

**Apparatus-Overview**

The existing set up is a flow-through system capable of delivering three gases, humidified or dry, to the sample contained in a an electric furnace. A room temperature bubbler provides humidity; if higher humidities are required, a syringe pump will need to be acquired and connected, and the tubing downstream must be heated with heating tape and insulation. A photograph (Figure A.2) and block diagram (Figure A.3) of the apparatus is shown below :

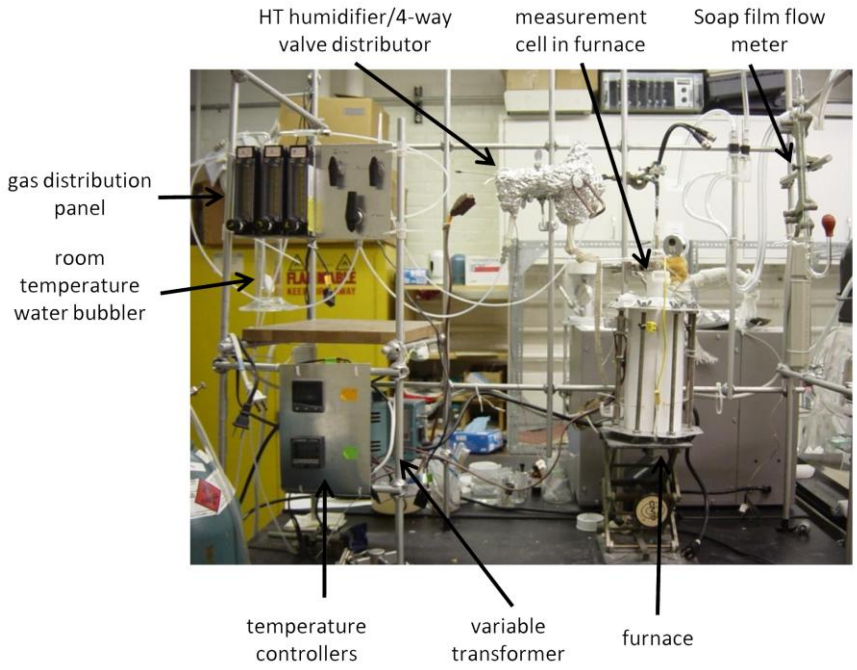


Figure A.2: Photograph of overall apparatus

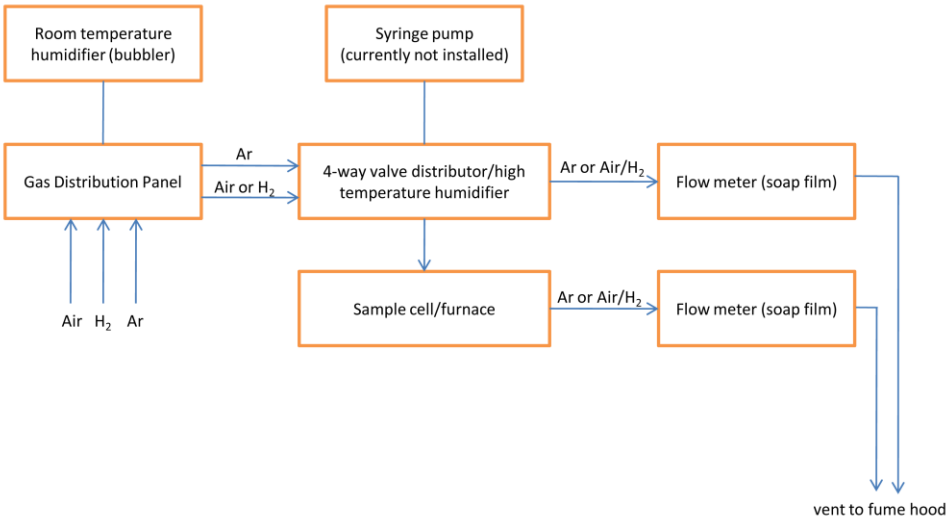


Figure A.3: Overall block diagram of apparatus

**Apparatus-Gas Distribution Panel**

The gas distribution panel (see Figure A.4 and Figure A.5) can supply either air or hydrogen (chosen by valve 1) to the furnace. This stream can also be humidified by a room temperature water bubbler (on/off selected by valve 3), or a high temperature humidifier further downstream between the gas distribution panel and sample.

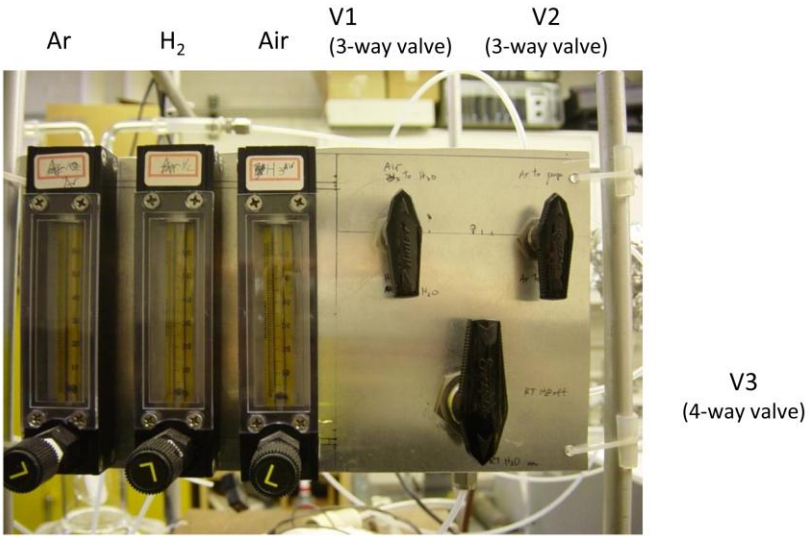


Figure A.4: Front view of the gas distribution panel

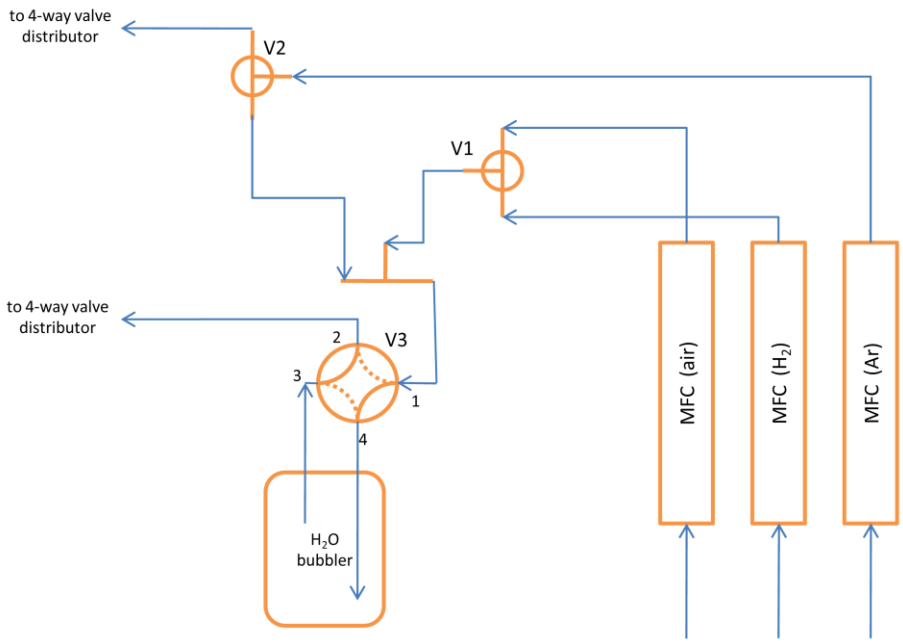


Figure A.5: Schematic of the gas distribution panel

If desired, argon may be used to dilute the air or hydrogen to a desired concentration before flowing to the furnace (valve 2). The ratios between argon and the

other gas would be determined by the mass flow controllers on the panel. When argon is not mixed with air or hydrogen, it simply flows directly to the 4-way valve distributor, and may be used to purge the furnace before/after introducing air/hyrdogen.

If absolute gas flow rates must be known, then the mass flow controllers must be calibrated with the gas to be used—the soap film flow meters further downstream may be used for this (assuming there are no leaks in the system!)

The room temperature humidifier (bubbler) provides 100% RH, which implies $P_{H2O}$ = 0.03 atm. Higher humidities will require the use of the high temperature humidifier further downstream, a syringe pump, and some of the tubing to be heated to prevent condensation.

Two streams exist, one from V2 and the other from V3. One stream, typically the V2 stream is used to purge the furnace before/after runs, while the V3 stream would supply the atmosphere during measurement. The 4-way valve selects which stream flows to the furnace.

If the tubing needs to be heated, the heating tape extending from the 4-way valve may be used to heat the tubing and top of the measurement cell. Another piece of tape and a condensation trap will be necessary on the exit port of the measurement cell, with a thermocouple and possibly a temperature controller to monitor. The silicone tubing used is reasonably heat-resistant. It is recommended to further wind inch-wide strips of fiber glass insulation on top of the heating tape, and aluminum foil can be wrapped on the outside to keep everything in place.

**Apparatus-High Temperature Humidifier/4-way Valve Distributor**

This piece (shown in Figure A.6 and Figure A.7) is constructed out of pyrex glass with a Teflon 4-way valve (stopcock), wrapped in heating tape and insulation; a thermocouple is also present for temperature control. The stream of measurement gas ("air or $H_2$") from V3 flows into the 4-way valve from the bottom left, and the purge gas ("argon") from V2 enters through the back on the right hand side. If the valve feels loose, it may be necessary to unwrap the insulation and tighten the stopcock.

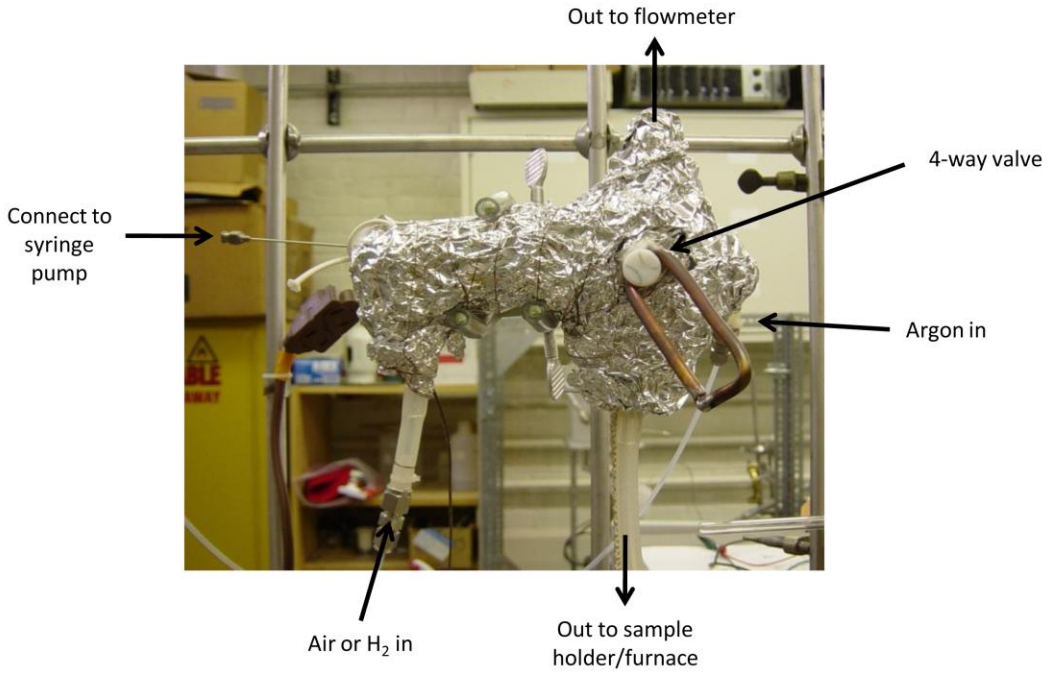


Figure A.6: Outer view of the high temperature humidifier/4-way valve distributor

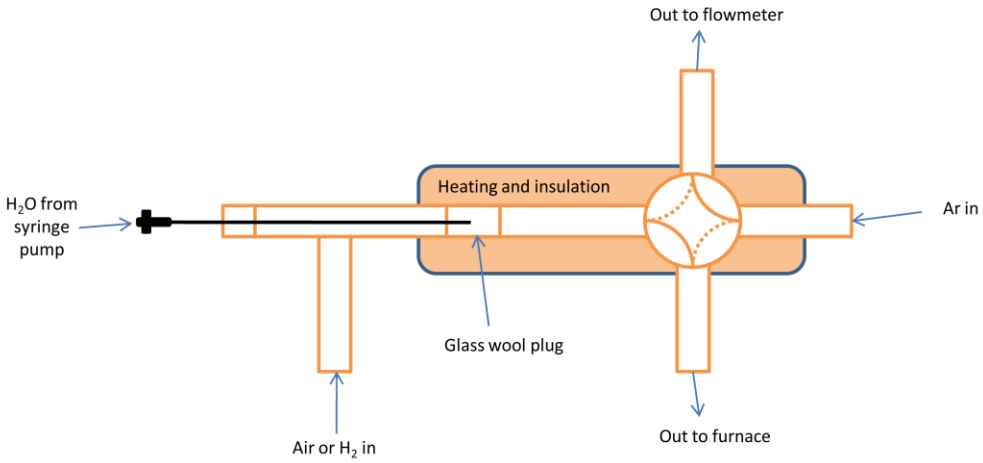


Figure A.7: Schematic of the high temperature humidifier/4-way valve distributor

If the water bubbler does not provide enough humidity, a syringe pump may be connected to the protruding needle. The humidity will depend on the flow rate of the air or $H_2$ gas, and the pumping rate of the syringe pump, so both will have to be calibrated—the syringe pump can be calibrated by disconnecting it, and running the syringe pump for an hour or so and weighing how much water is ejected. The dew point should be checked, since all areas downstream will have to be heated above this temperature.

**Apparatus-Sample Holder**

The arrangement shown in Figure A.1 on page 3 may be adequate for most measurements. A spring-loaded measurement cell for measuring pellet samples has also been provided Figure e A.8. Using this cell provides leads which are shielded for most of the lengths. Since pyrex glass parts are used, the maximum temperature for this cell is approx. 500°C.

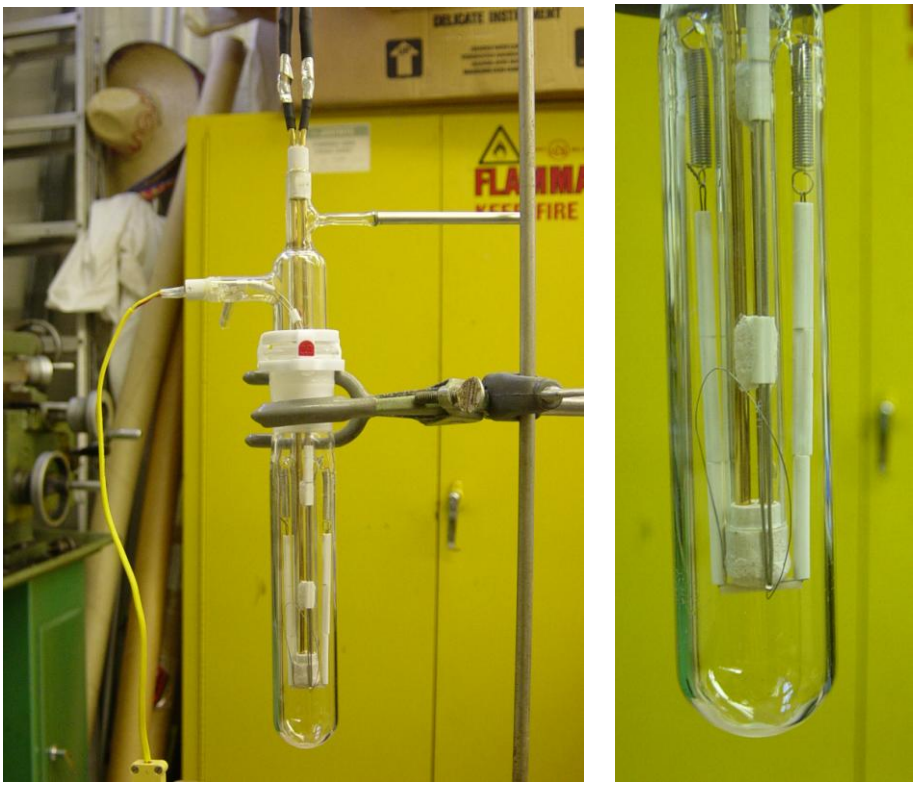

Figure A.8: Low-noise measurement cell

In this cell, the pellet is held in place by an alumina bar pulled two springs (see the schematic in Figure A.9). One contact is a piece of Pd foil, while the other contact is made by Pd wire which must be sandwiched between the pellet and the aluminar bar. The type K-thermocouple can be used to monitor the temperature of the pellet. Note the Au-covered glass at the top of the cell is fragile! Other simple spring-loaded pellet holders may be constructed from pieces of sintered alumina (such as boats or tubing, available from AlfaAesar and Omega), and high temperature cement (OmegaBond 700 will adhere to glass and ceramics). Porous sintered alumina can be machined very easily on a diamond bandsaw, and springs can be wound from Nichrome wire.

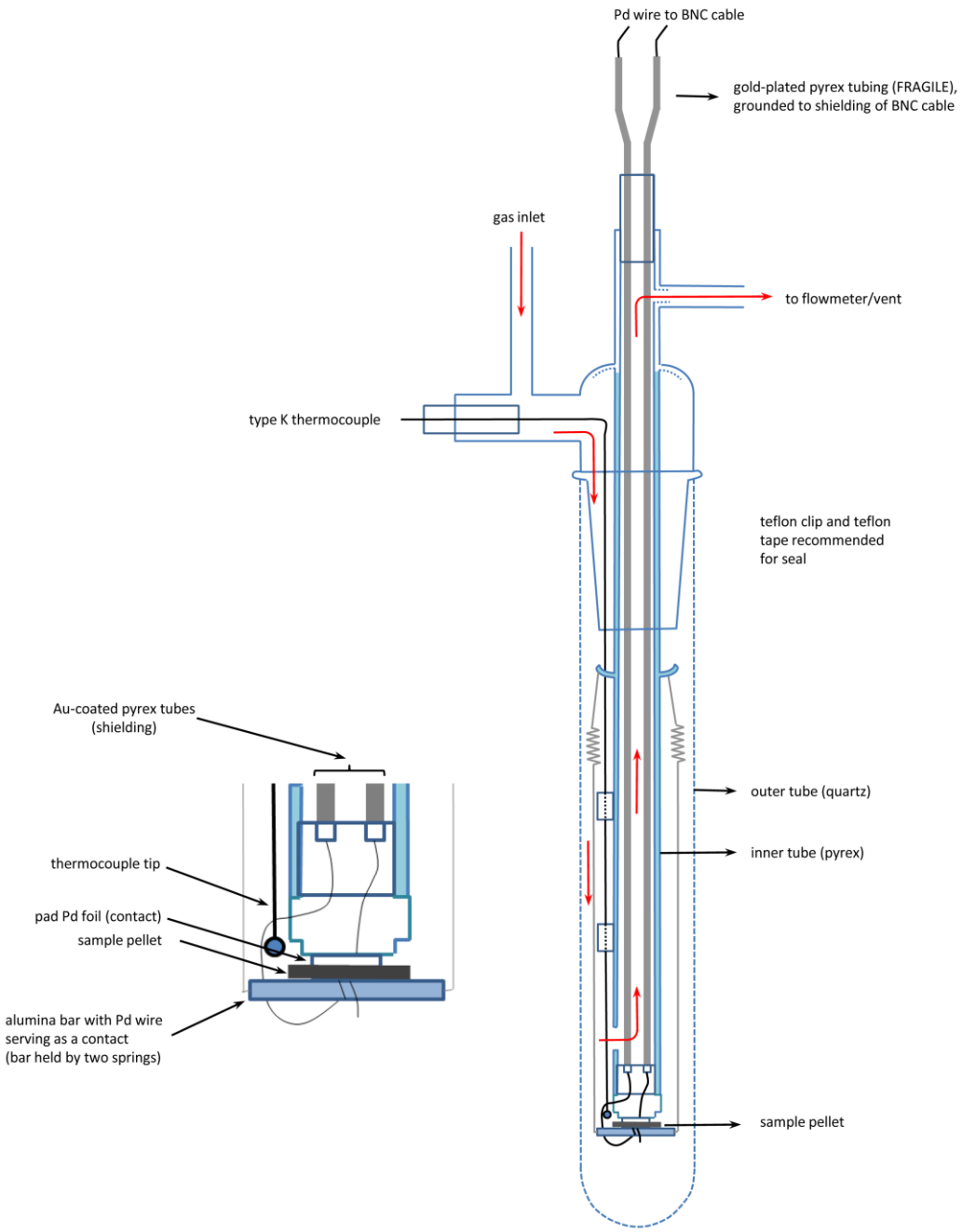


Figure A.9: Schematic of the low-noise measurement cell

**Apparatus-Furnace**

**Important:** The electric furnace (Figure A.10) runs on 60V, rather than 110V—therefore, it must connected to the variable transformer supplied on the bench. If 110V is applied, the heating elements on the furnace may burn out! This can be checked by a simple conductivity test using a multimeter.

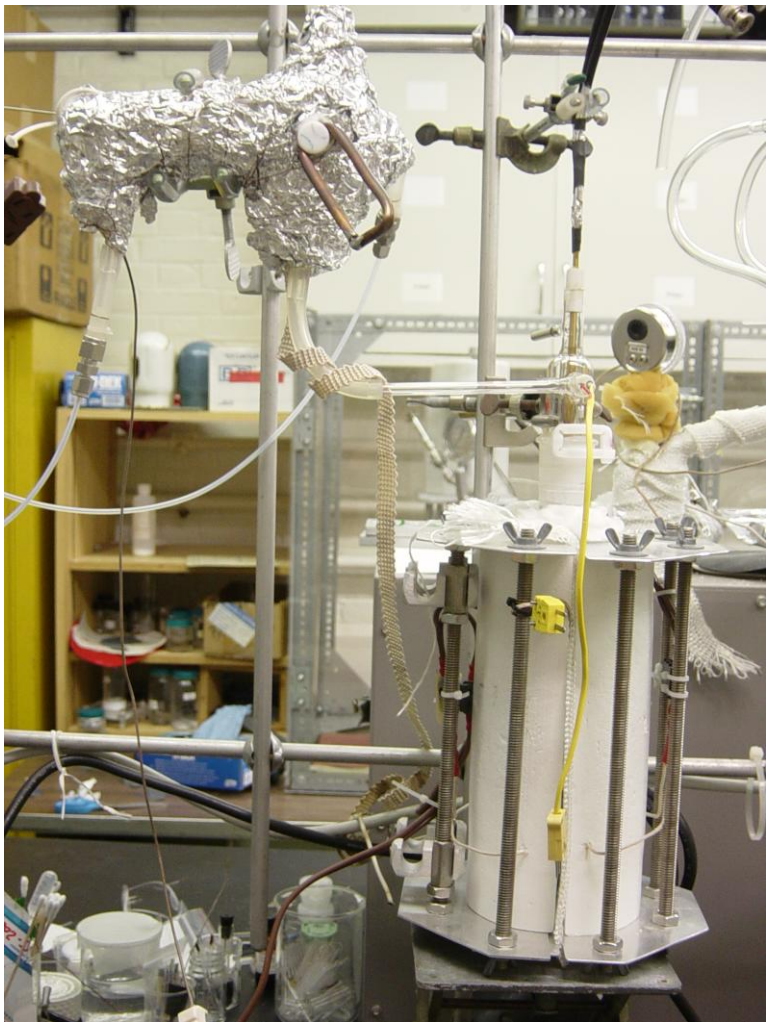

Figure A.10: Furnace with the measurement cell in place

This power to this variable transformer is controlled by the temperature controllers mounted on the left of the apparatus. The thermocouple on the furnace should be used to control the temperature, while the thermocouple on the cell can be used to

monitor the actual sample temperature. It will be necessary to plug bottom of the furnace and any gaps at the top using fiber glass insulation.

## Sample Procedure for a Run

### Using room temperature bubbler: $P_{H2O}$: 0.03 atm

1. After loading pellet, fill bubbler with water. Plug the needle on the 4-way distributor.
2. Set V2 to purge, V3 to on, 4-way distributor to send V2 to the sample (i.e. flush furnace with Ar—good idea if you're going to use hydrogen next)
3. Open gas cylinders, check flowrates on the mass flow controllers and soap film flowmeters. Low exit flow rates indicate large leaks or broken glass parts.
4. Switch the 4-distributor so that the argon from gas from V3 enters the furnace.
5. Set the furnace to the desired temperature. Wait for equilibration and the sample to fully hydrate (or dehydrate!)
6. Acquire impedance spectra. Repeat steps 5, 6 as desired.
7. Lower furnace temperature
8. Switch 4-way distributor to purge furnace with flow from Ar.
9. When furnace is cool, can take out sample, close all gas cylinders.

### Using the high temperature bubbler: $P_{H2O}$: >0.03 atm

1. Fill syringe with water.
2. Start gas flows to achieve necessary flow rates. The measurement stream from V3 should go straight to the flowmeters rather than the furnace.

3. Heat the humidifier to approx. 120°C, and the gas tubing to above dewpoint, and the furnace to a moderate temperature say, 200 °C (or anything above dewpoint)
4. Best to wait a while (30-60min)
5. Turn on the syringe pump. You should see condensation in one of the traps. Wait for awhile.
6. Switch the 4-way distributor to send the humidified stream to the measurement cell. You should see condensation in the other trap, now.
7. Adjust furnace temperature, acquire spectra
8. When done, purge the furnace with dry argon, turn off the syringe pump. After a few minutes, the gas flows will have removed all moisture and the humidifier/tubing can let to cool.

# VITA

## Yoji Kobayashi

Yoji Kobayashi was born in 1978 in Frankfurt am Main, Germany. After living in the UK and Japan, he attended Dartmouth College, majoring in Chemistry (organometallic synthesis, Prof. David S. Glueck) but learning Chinese instead. After spending one year at the Tokyo Institute of Technology (heterogeneous catalysis, Prof. Kiyoshi Otsuka), he finally settled on coming to the US again for attending graduate school (and sometimes playing in the orchestra), where he met his wife Leiliang Zheng.